4. RESULTS AND DISCUSSION

4.1 Analysis of Inlet and Exit Flow Characteristics

The second and third experiments as described in Section 3.2 resulted in a series of plots for rotor inlet and exit flow characteristics with respect to the distortion screen at three different spans and up to three different blade loadings. Rotor speed was maintained constant at 2100 rpm. Rotor flow data were obtained for a 270° circumferential profile, which far exceeded the portion of the inlet which would directly experience the effects of the various 110° distortion screens. The three-dimensional rotor inlet flow survey was performed with 30° resolution about the circumference of the annulus 0.2 C upstream of the blades, while the one-dimensional rotor exit flow survey was performed with 10° resolution 0.2 C downstream of the blades.

Figure 4.1 shows the characteristic of distortion screen Level 2 as compared with the undistorted rotor characteristic. Based on the error analysis of Appendix B, the flow coefficient C_x/U_{tip} has an uncertainty of $\pm 2.13 \times 10^{-3}$ while the pressure rise coefficient Psi has an uncertainty of $\pm 6.55 \times 10^{-4}$. Points A, B, and C moving upward on the Level 2 and undistorted speed lines correspond to increased loading on the blades, with points A being at pre-stall conditions. All data were curve fitted using cubic splines as described in Appendix D.

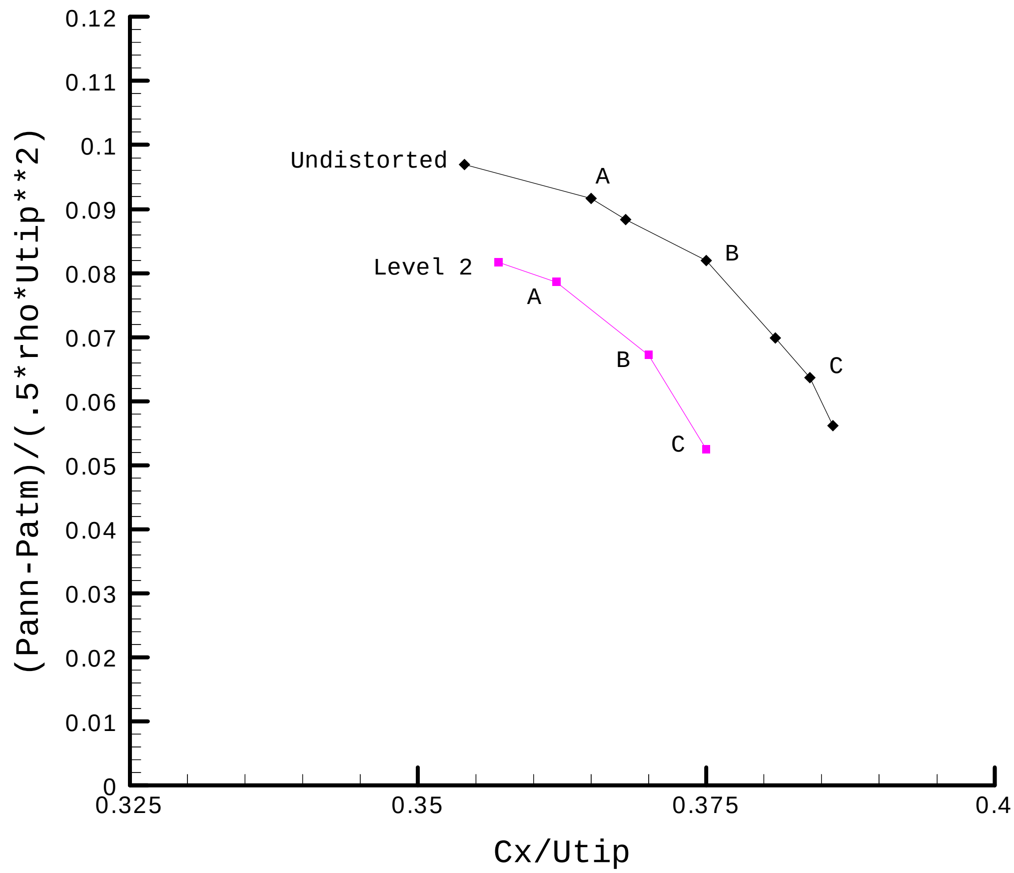

Figure 4.1 Characteristics of Undistorted and Level 2 Distorted Rotor Performance.

In order to compare the response of the flow characteristics to distortion as functions of span, loading, and distortion intensity, it is necessary to overlay the resulting data plots. Figure 4.2 depicts an overlay of the inlet flow characteristics for distortion screen Level 2, operating point A, at 50 % and 33 % spans in order to compare the inlet flow parameter responses as functions of measurement span. Based on the error analysis of Appendix B, measurements for flow pitch angle and angle of attack have uncertainties of ± 3.0º while measurements for the non-dimensional inlet and exit pressure parameters have uncertainties of 2.75×10^{-3}. For 50 % span, the inlet relative total and static pressure profiles remain relatively constant until just prior to the distortion screen where they rapidly decrease to 5.4 times and 1.3 times their undistorted magnitudes, respectively. The flow pitch angle and angle of attack are relatively constant until entering the distorted region, where they increase steadily and peak at the trailing edge of the distortion where the total pressure is lowest.

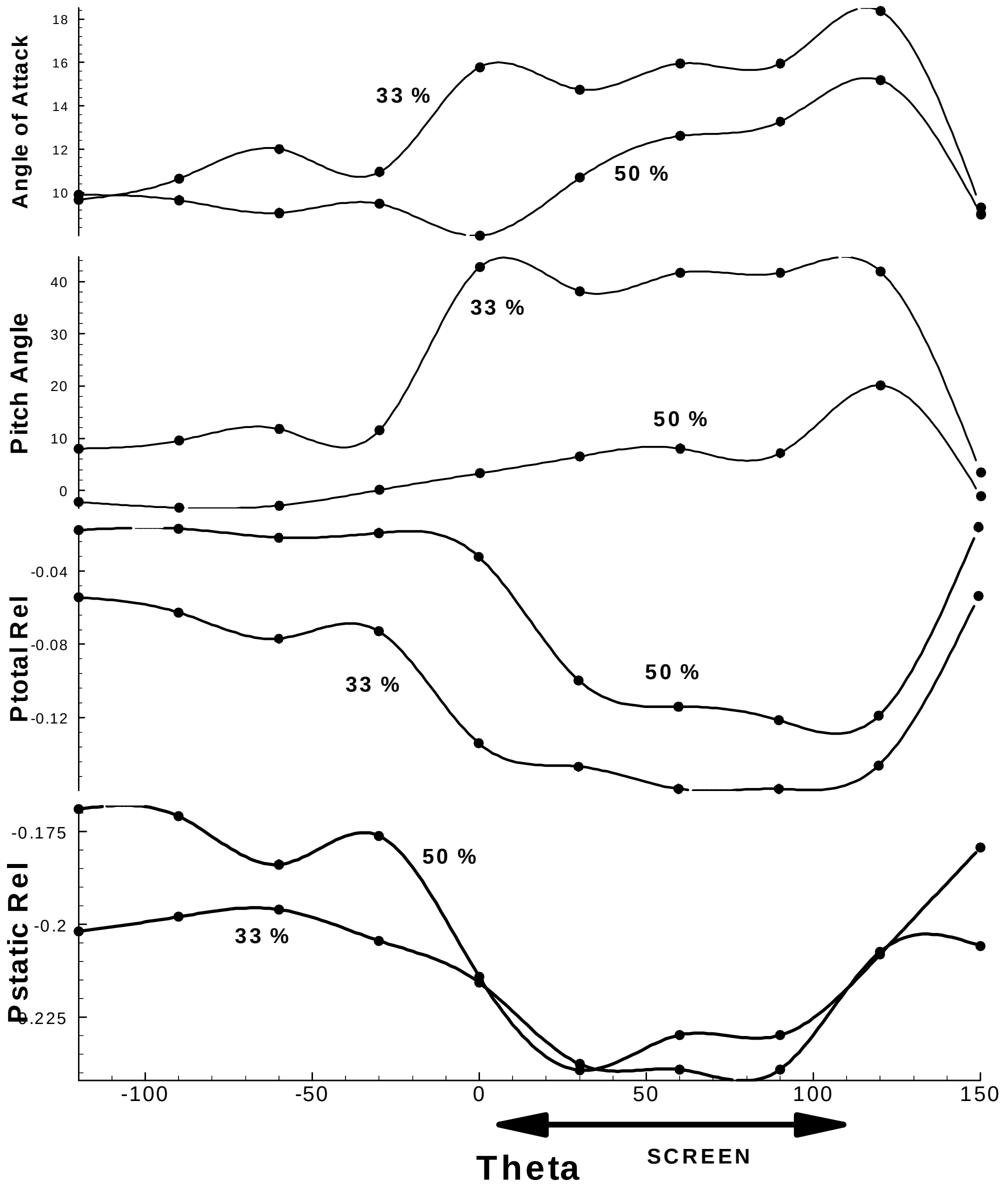

Figure 4.2: Inlet Flow Characteristics for Distortion Screen Level 2, Operating Point A, at 50 % and 33 % Spans.

For 33 % span data shown in Figure 4.2, the pitch angle and the angle of attack are higher throughout the distorted region, as opposed to solely at the trailing edge as was the case for the same screen and operating conditions at 50 % span. It appears as though the inlet flowfield response to distortion is in phase for both 50 % and 33 % spans, with the exception of the inlet total pressure profile where the 33 % span measurement response is 30º in advance of the 50 % span response. Apart from this observation, thus far it appears as though the inlet flow parameter responses to distortion are not functions of measurement span.

The distortion screen causes a total pressure drop across the screen, thereby reducing the absolute velocity of the incoming flow. This reduction in absolute velocity causes an increase in the computed angle of attack to the blades by reducing the axial velocity and increasing the relative flow angle to the blades as they pass behind the distortion screen. Note that the relative total pressure in Figure 4.2 varies as much as 22 % behind the distortion screen. Neal (13) proposed the variation of inlet parameters behind the screen to be due to the non-uniform porosity of the distortion screen and support mesh.

In addition, note that the angle of attack at the trailing edge of the distortion screen for 50 % span as shown in Figure 4.2 exceeds that of the steady-state stalling angle of 12.6º. As this may be a case of dynamic stalling of the blades, it is interesting to investigate the changes in the wake parameters corresponding to this inlet data. These wake parameters are presented in the 50 % span, operating point A, screen Level 2 data as shown in Figure 4.3. Figure 4.3 also depicts exit flow data for the same operating conditions at 33 % span.

For 50 % span, the peak in the inlet flow angle of attack is preceded 10º circumferentially by a 60 % increase in the suction side jet semi-width. No trend is observable in the suction side jet maximum relative pressure. However, it appears as though the rotor may be maintaining a constant mass rate of flow despite the increases of 20 % in the wake semi-width and 25 % in the wake maximum relative defect as compared to their undistorted values. This would agree with the results of Colpin and Kool (31). All rotor exit flow trends return to their original undistorted values after the trailing edge of the screen, indicating reattachment of the flow if it were indeed separated during the distortion cycle. Using a one-dimensional exit total pressure survey, it is not possible to determine if the blades were actually undergoing a dynamic stalling event.

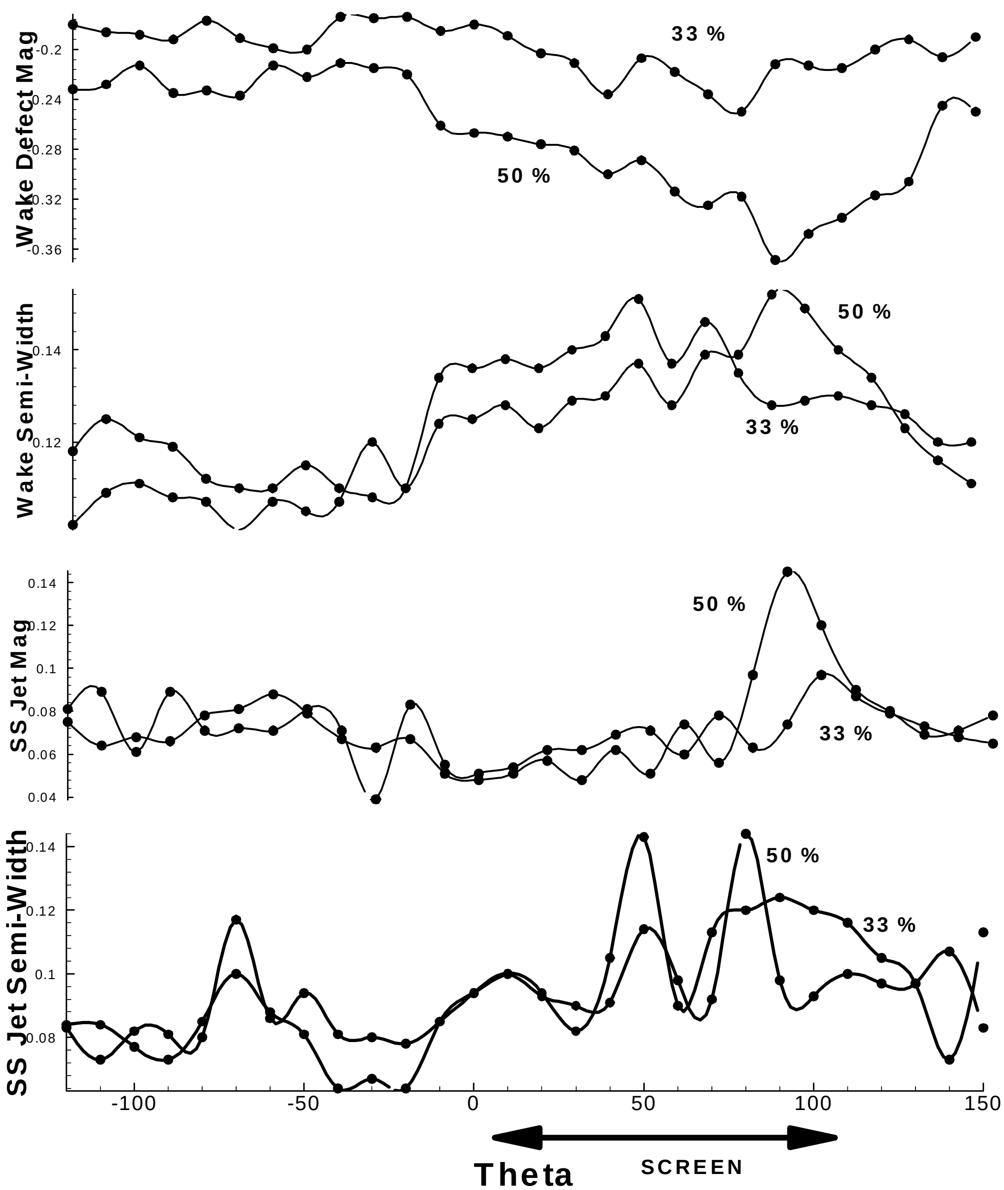

Figure 4.3: Exit Flow Characteristics for Distortion Screen Level 2, Operating Point A, at 50 % and 33 % Spans.

For the 33 % span data shown in Figure 4.3, the peak angle of attack at the trailing edge of the distortion corresponds to much prior thickening of the suction side jet semi-width and a 75 % increase in the suction side jet relative pressure at the rotor exit. There is a 17 % increase in the wake semi-width behind the distortion as compared to the undistorted region, which spans almost 15 % of the blade passage. The wake maximum relative defect had greater magnitude behind the distortion screen but varied a great deal.

Performing a spanwise comparison of the data in Figure 4.3, the suction side jet parameters are quite random although they both peak at the trailing edge of the distortion. Wake semi-width and depth are strongly in phase with one another, and both peak in magnitude at the trailing edge of the distortion screen. None of the response parameters shown in Figure 4.3 indicate that response is a function of span.

Figure 4.4 presents inlet flow characteristics for distortion screen Level 2, operating point A at 50 % and 67 % spans in an effort to further quantify response to distortion as a function of span. For 67 % span, the angle of attack gradually increases and peaks at the trailing edge of the distorted region, which agrees with the trending of the 50 % span data but is contrary to the 33 % span inlet data, both of which are shown in Figure 4.2. The static pressure profile of 67 % span is in phase with that for 50 % span, although the 67 % span total pressure recovery at the trailing edge of the screen is 30º in advance of the recovery for 50 % span. Again, with the exception of the inlet total pressure profile, the data presented in Figures 4.2 and 4.4 indicate that inlet flow response to distortion is not a function of span.

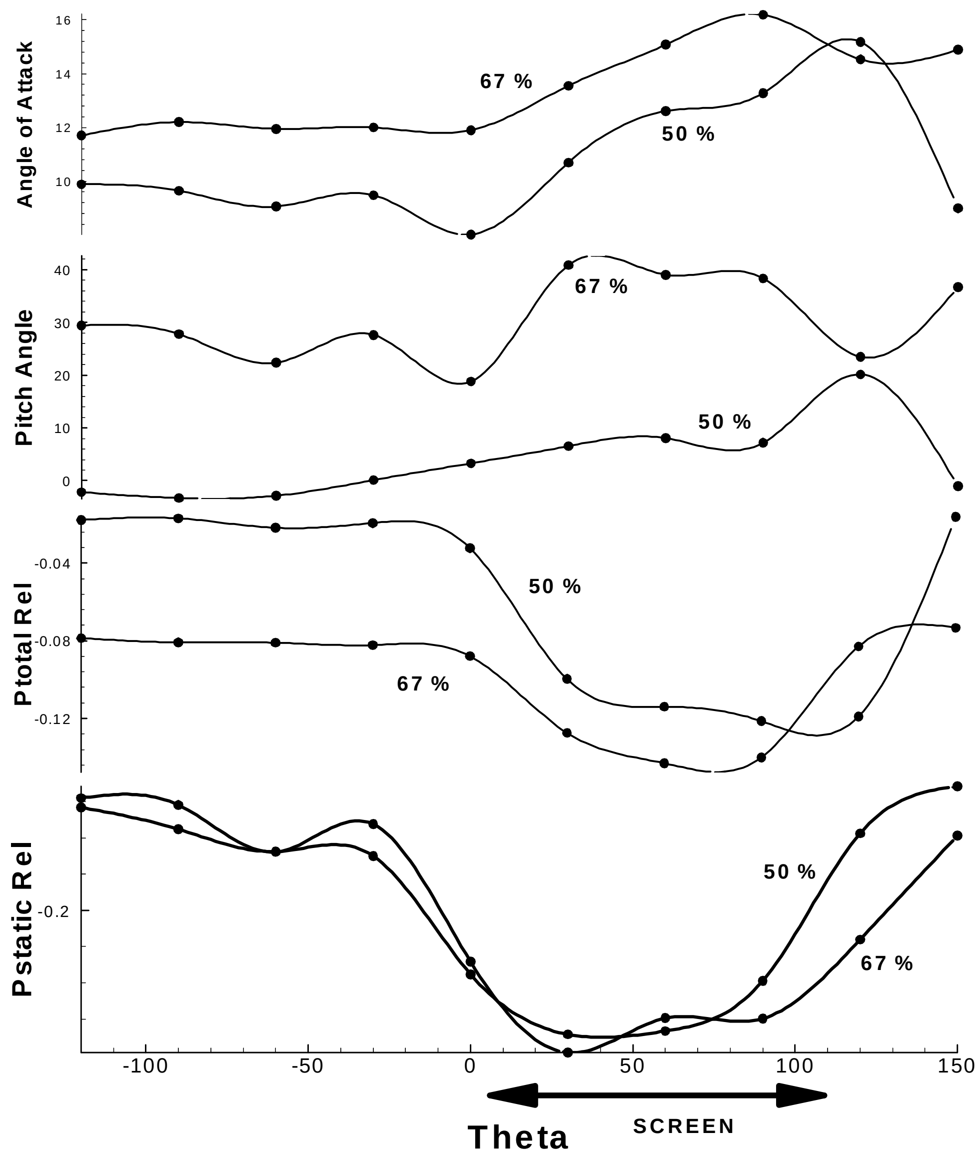

Figure 4.4: Inlet Flow Characteristics for Distortion Screen Level 2, Operating Point A, at 50 % and 67 % Spans.

Figure 4.5 presents the exit flow characteristics for distortion screen Level 2, operating point A for 50 % and 67 % measurement spans. The peak angle of attack at 67 % span corresponds to much prior thickening of the suction side jet semi-width on the order of 17 % throughout the distorted region. The suction side jet relative maximum data is inconclusive. None the less, similar to the case of 33 % span data as shown in

Figure 4.3, the wake semi-width and defect relative maximum amplitudes increased by 22 % and 28 %, respectively.

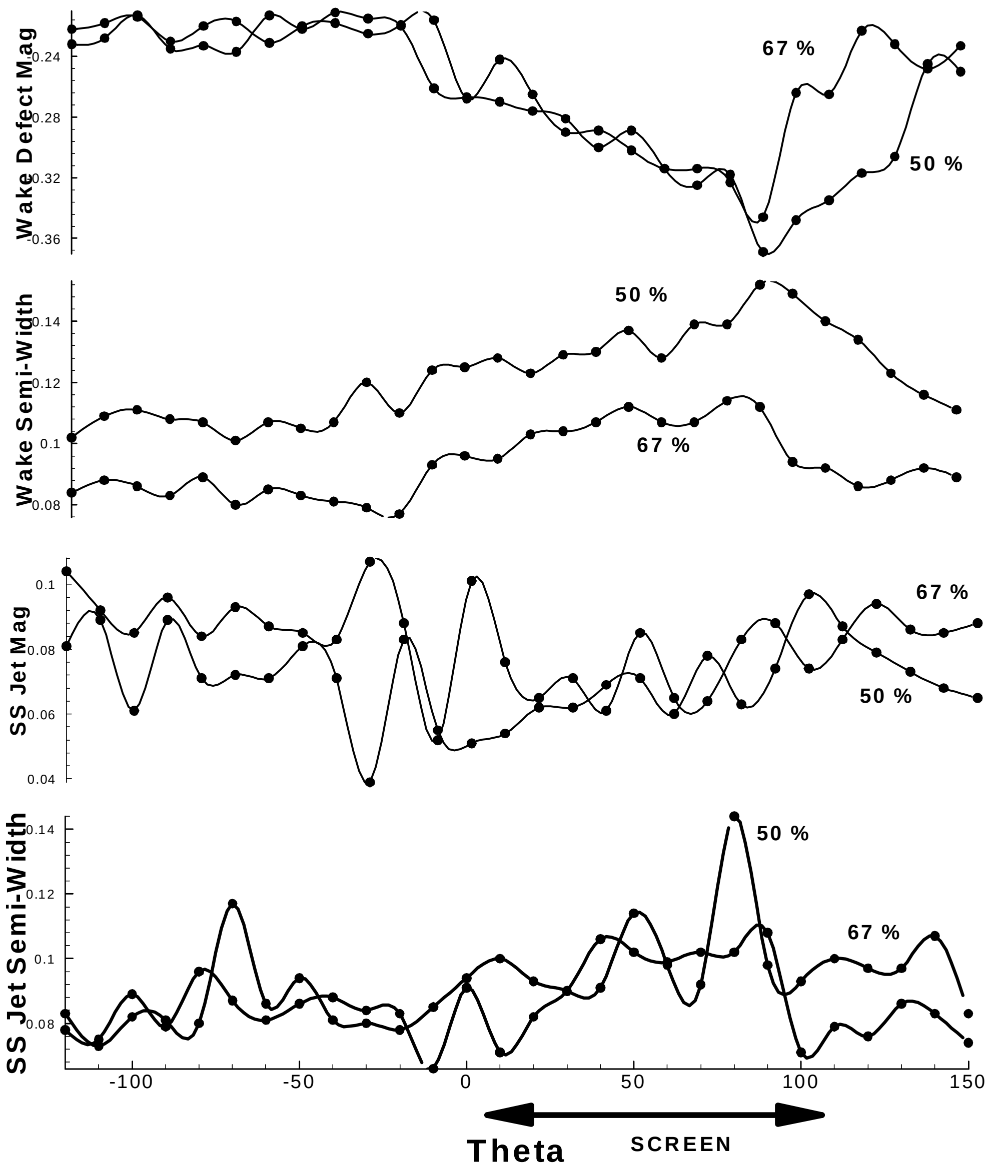

Figure 4.5: Exit Flow Characteristics for Distortion Screen Level 2, Operating Point A, at 50 % and 67 % Spans.

Comparing wake response values between 50 % and 67 % spans in Figure 4.5, the suction side jet parameters at either span have no discernible trending. The wake semi-width and magnitude are strongly in phase with one another. Based on this analysis as well as the comparison between 33 % and 50 % spans one concludes that neither the inlet nor exit flow parameter responses to distortion are functions of span.

Based on the wake semi-width data in Figures 4.3 and 4.5, it is most likely that stall for this RAF-6 rotor blade originates at the hub, a result in agreement with Verdesoto (35) and Dancy (11). The suction side semi-width is consistent for all blade spans although it has a lower peak at 67 % span, while the suction side jet magnitude is consistent for all spans. The wake semi-width is lowest at 67 % span, while the wake defect magnitude is lowest at 50 % span and highest at the 33 % and 67 % spans. Inlet data shown in Figures 4.2 and 4.4 at 33 %, 50 %, and 67 % spans for operating point A indicate the highest angles of attack and flow pitch angles to occur at the hub and tip of the blades, remaining lowest at 50 % span. This result was true for regions within and without the distorted sector.

In order to evaluate the effects of loading on parameter response to distortion, Figure 4.6 presents inlet and exit flow characteristics for screen Level 2, 50 % span, at operating points A and C. For operating point C, the inlet relative total and static pressure profiles remain flat until just prior to the distortion screen where they rapidly decrease to 6.0 and 1.3 times their undistorted magnitude, respectively. This total pressure loss is an increase from 5.4 times the undistorted value for operating point A to 6.0 times the undistorted value as shown for operating point C. The increase in magnitude of the total pressure loss behind the screen makes physical sense, as the total pressure loss across an arbitrary screen will increase as flow velocity across it is increased. This applies to the case where operating point C has a higher axial flow velocity than operating point A. Flow pitch and yaw angles for operating point C are flat until the leading edge of the distortion screen. They then increase steadily until dipping slightly at the 30º angle into the screen and peak at the trailing edge of the screen, where the flow angle of attack exceeds the steady-state stalling angle by only 0.7º and it is unlikely that dynamic stalling of the airfoils has occurred.

The changes in the inlet total pressure profile for operating point C precede those for operating point A by 30º in both the drop and recovery stages. Changes in pitch angle and angle of attack are in phase, although their peaks for point C once again precede those for point A by 30º.

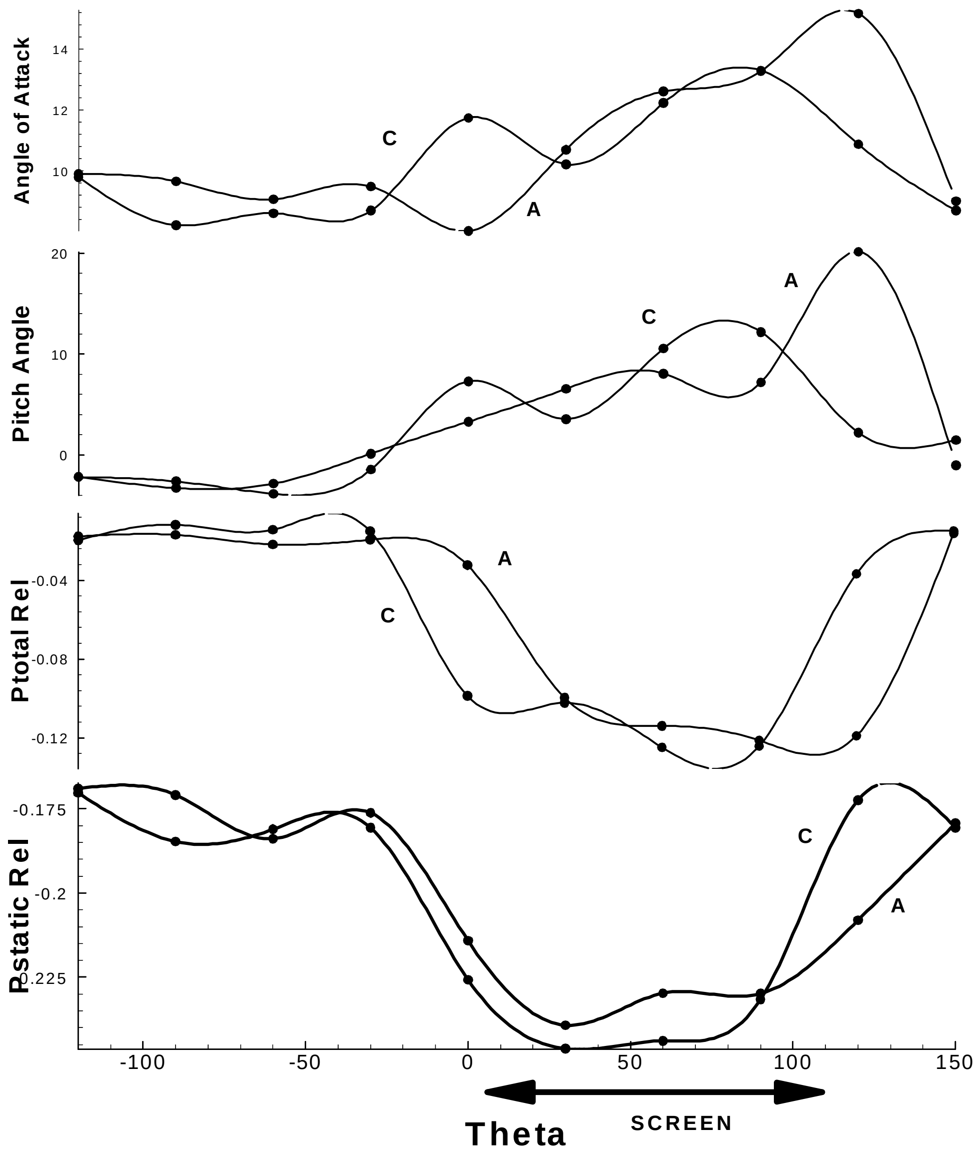

Figure 4.6: Inlet Flow Characteristics for Distortion Screen Level 2, 50 % Span, Operating Points A and C.

Figure 4.7 presents the exit flow characteristics for the Level 2 screen at 50 % span for operating points A and C. For point C, the suction side jet semi-width and magnitude increase 55 % and 100 % to compensate for the reduced mass flow due to increases of 20 % ad 22 % of the wake semi-width and wake defect magnitude, respectively, as compared to their undistorted values. There is also an unexplained peak in the suction side jet semi-width 60º in advance of the distorted region. The wake defect average for operating point A behind the distortion is 4 % higher than that for operating point C, indicating a slightly greater wake defect for increased loading. The average wake semi-width behind the distortion is only 0.5 % higher for operating point A than C, indicating only a very slight thickening of the boundary layer on the blades with increased loading as the plenum exit throttle plate is closed.

As usual, the suction side parameters presented in Figure 4.7 are quite random. However, the wake parameters between points A and C for constant span and distortion intensity are almost identical. This leads one to conclude that wake response to a distortion is not a function of loading.

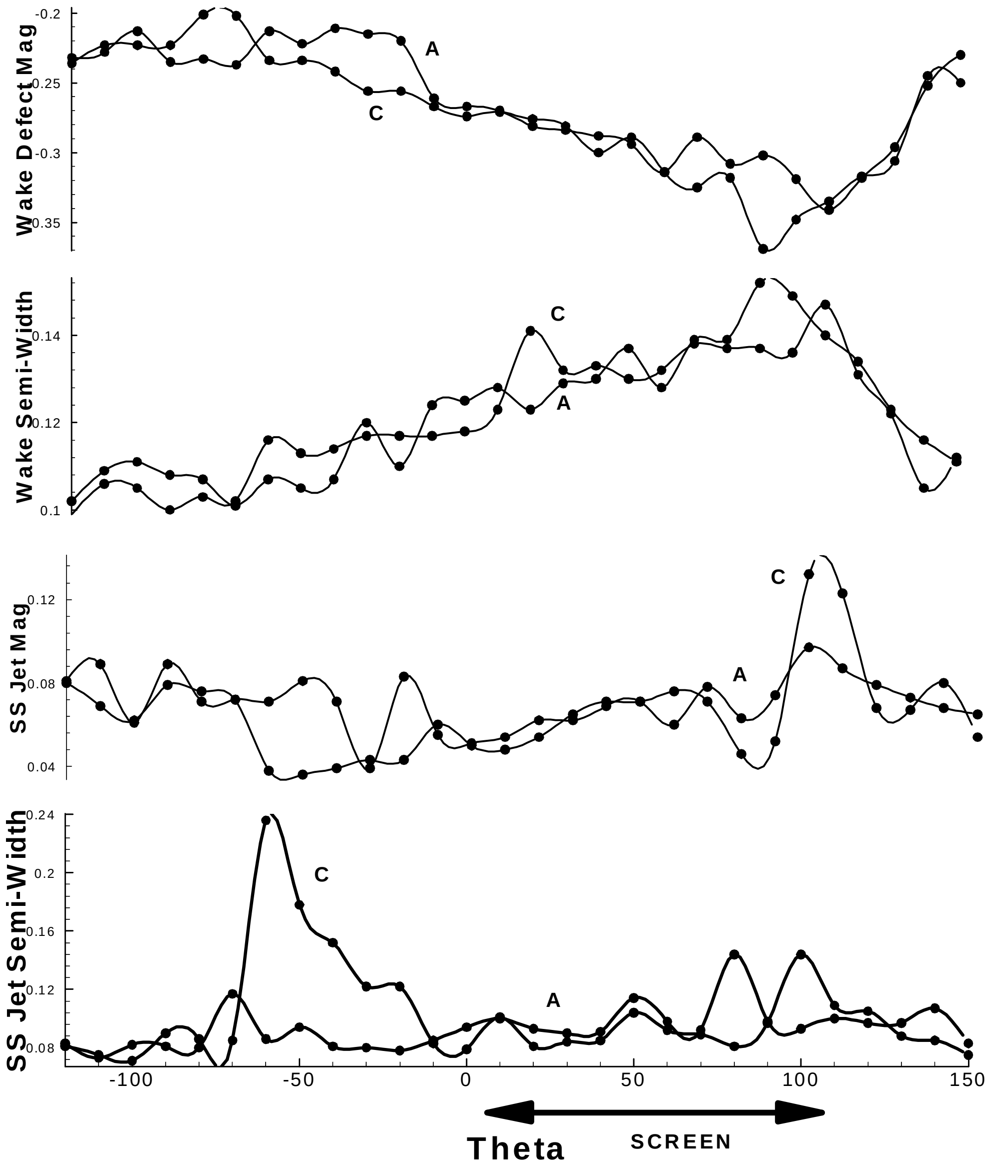

Figure 4.7: Exit Flow Characteristics for Distortion Screen Level 2, 50 % Span, Operating Points A and C.

The final variable in the second and third set of experiments is the effect of distortion screen intensity on flow response. Figure 4.8 depicts the characteristics of the undistorted, Level 1, and Level 2 distorted rotor performance at the aforementioned 2100 rpm.

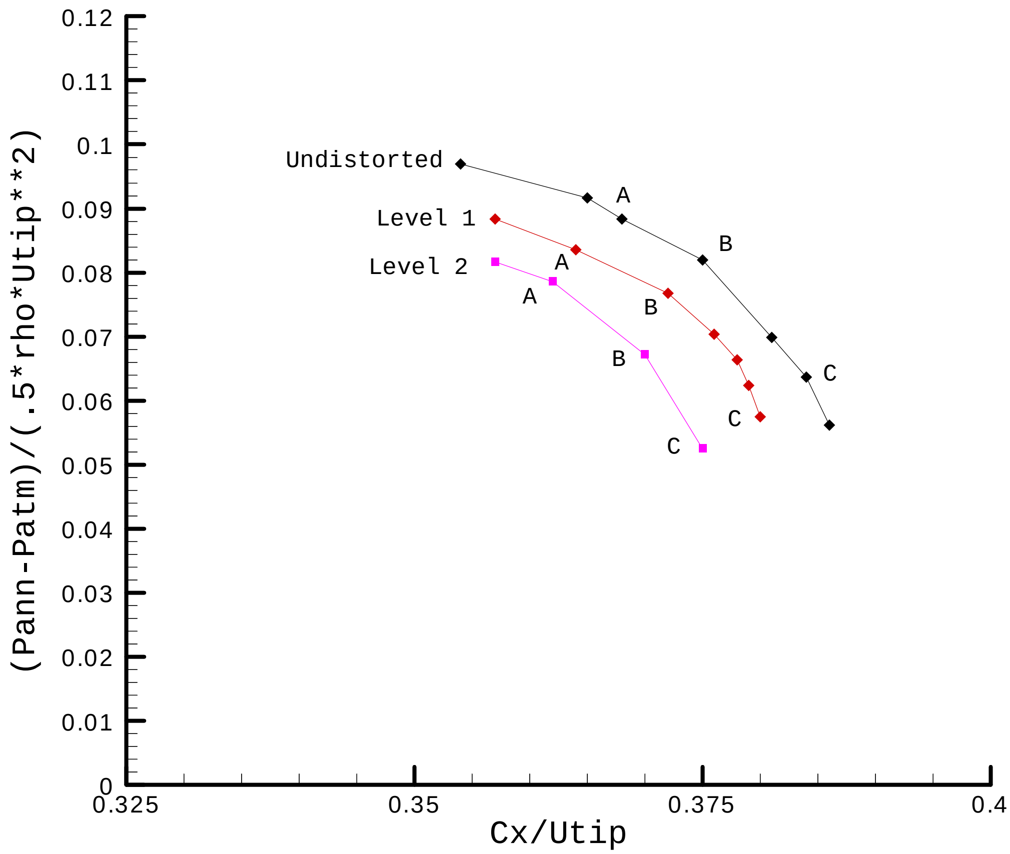

Figure 4.8: Characteristics of Undistorted, Level 1, and Level 2 Distorted Rotor Performance.

Inlet flow data corresponding to the Level 1 and Level 2 distorted rotor performances for 50 % span, operating point A are shown in Figure 4.9. The total and static pressure profiles for the Level 1 and Level 2 screens are exactly in phase, while peaks in the pitch angle and angle of attack are 30º in advance for the Level 1 screen.

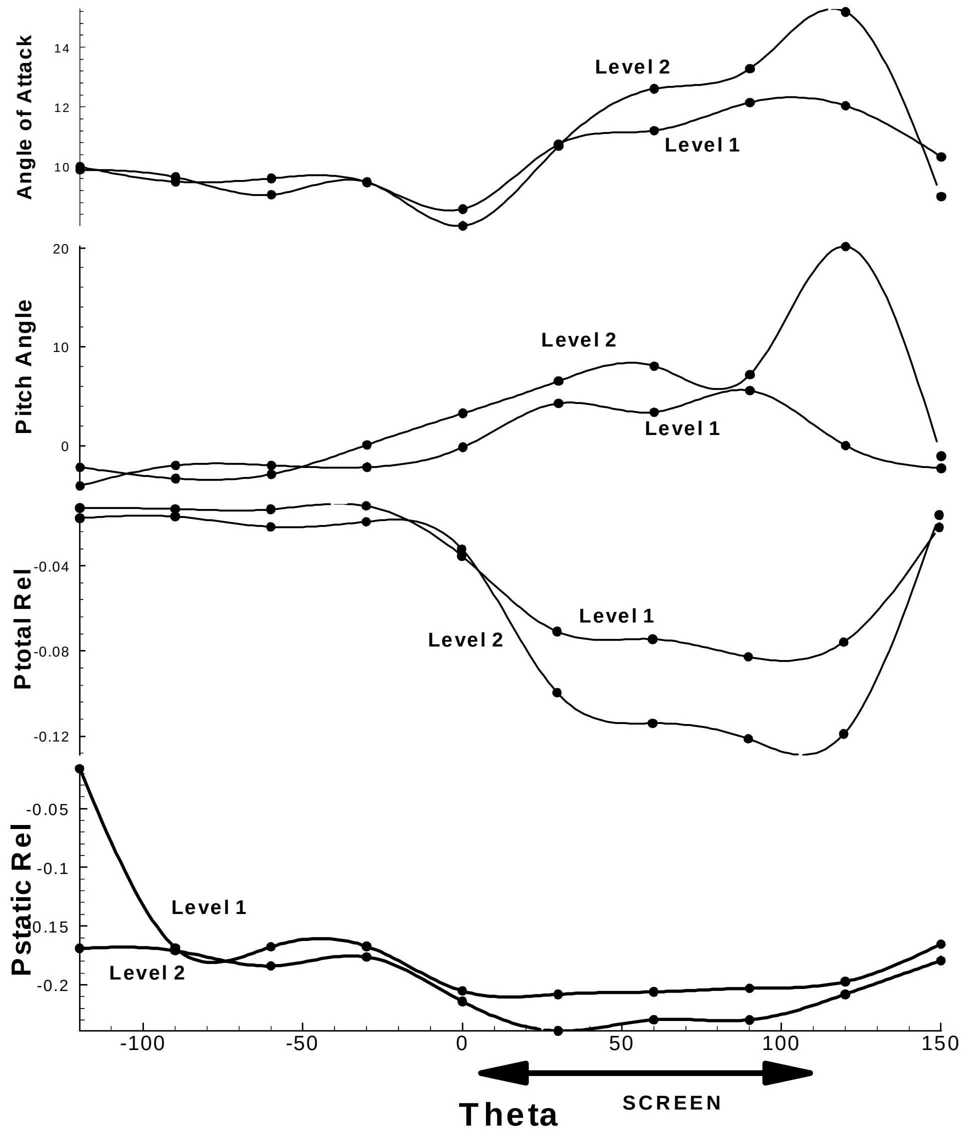

Figure 4.9: Inlet Flow Characteristics for Distortion Screens Level 1 and Level 2, 50 % Span, Operating Point A.

Figure 4.10 depicts the exit flow characteristics for distortion screens Level 1 and Level 2 for operating point A at 50 % span. As usual, the suction side parameters are quite random. Changes in the wake semi-width are exactly in phase for both screens, with the exception that the peak for the Level 1 screen occurs 50º after that for the Level screen. Changes in wake magnitude for the different screen levels are quite different, with the Level 2 wake responding to the distortion 40º in advance of the response for the Level 1 wake. The Level 2 wake magnitude response has a far greater peak value than does that for the Level 1 wake, as would be expected for a screen with lower porosity.

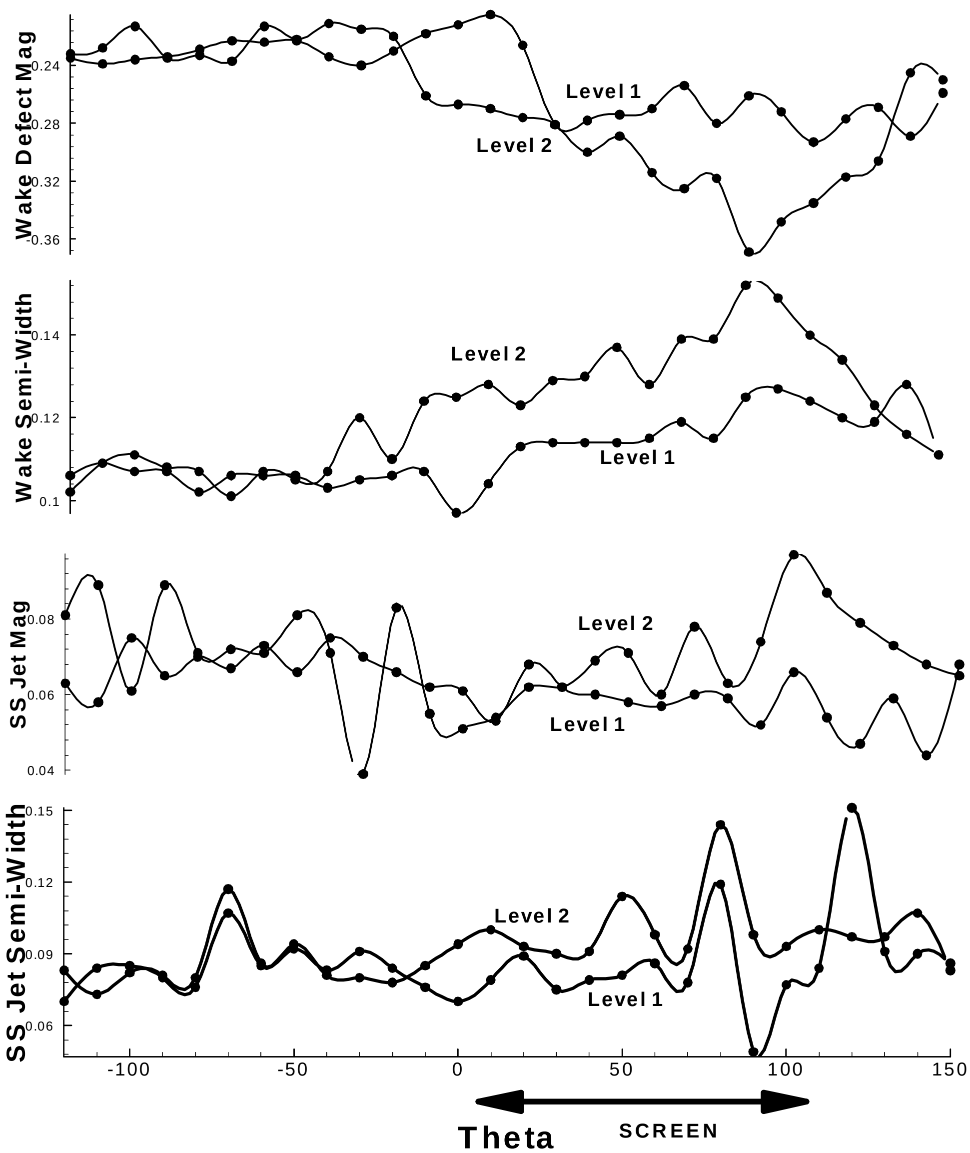

Figure 4.10: Exit Flow Characteristics for Distortion Screens Level 1 and Level 2, 50 % Span, Operating Point A.

Based on the analysis performed in this section, the time a blade responds to an inlet distortion does not appear to be a function of measurement span, blade loading, or distortion screen intensity. The remaining data for screens Level 1, Level 2, and Level 3 at 33 %, 50 %, and 67 % span for all operating points are available in Appendix A and exhibit similar trends of flow response to distortion.

4.2 Analysis of Rotor Exit Flow Time Response

Based on the conclusions from a one-dimensional exit total pressure survey, one must observe that the time a blade senses the rotor inlet flow effects relative to the distortion screen is not a function of span, loading, or distortion screen intensity.

In addition, it is worthwhile to investigate the time displacement of all five of the wake parameters with respect to the input driving functions of total pressure relative to atmospheric ($Pt_{\text{total rel}}$) and the flow angle of attack (α) to the rotor blades. The following is an analysis of the screen Level 2, operating point A time response of the wake parameters for 50 %, 33 %, and 67 % spans. The two inlet drivers are printed in black, while the wake width parameters are blue and wake magnitude parameters are red.

Figure 4.11 presents plots of the suction side jet semi-width as compared to the rotor inlet drivers for operating point A at 50 % span. The lower plot of suction side jet semi-width as compared with inlet relative total pressure shows a flat total pressure profile in the undistorted region but an unexplained spike in the jet semi-width. Approaching the distortion screen leading edge, the total pressure slowly decreases, in phase with a corresponding increase in the jet semi-width. The relative total pressure drop increases roughly 300 % and remains fairly constant until peaking in magnitude 90° into the distortion screen, while the peak in the jet semi-width occurs 80° into the distortion screen. This jet semi-width peak is 50 % greater than the average of its other values behind the screen.

The upper plot of Figure 4.11 compares inlet angle of attack with suction side jet semi-width. Again, both parameters are relatively flat until reaching the leading edge of the distorted region, where they slowly increase in phase with one another. The angle of attack peaks 10° after the trailing edge of the distortion screen, which is 40° out of phase with the suction side jet semi-width peak 80° into the distorted region. One observes that there is weak correlation between the suction side jet semi-width and the inlet drivers. It is important to note that peaks in the inlet parameters are not necessarily true data points but may have been determined from cubic spline interpolation as described in Appendix D. However, the peaks in the lines are near true data points, which are indicated by circular symbols.

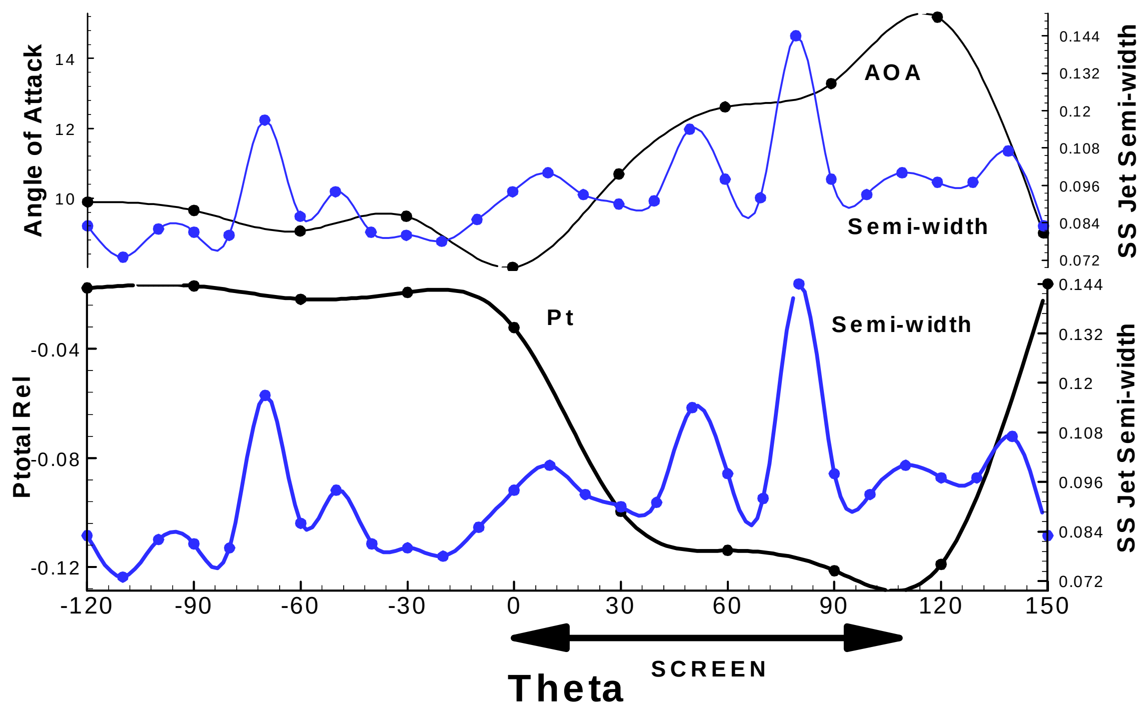

Figure 4.11: Suction Side Jet Semi-Width vs. Input Drivers for Operating Point A at 50 % Span.

Figure 4.12 presents plots of the suction side jet relative magnitude as compared with the inlet flow drivers for operating point A at 50 % span. While the inlet total pressure profile is relatively flat prior to the distorted region, the jet magnitude varies wildly. Once into the distorted region, the jet magnitude increases in phase with the total pressure drop, although at a much slower pace. Contrary to the case with the jet semi-width, the jet magnitude peak behind the screen corresponds to the maximum value of the magnitude of the relative total pressure at the inlet. Once behind the distortion screen, the jet magnitude also increases in phase with the inlet flow angle of attack but peaks 20° prior to the angle of attack peak 10° after the trailing edge of the distortion. Much stronger correlation is apparent for the suction side jet magnitude with respect to the inlet drivers than it was for suction side jet semi-width.

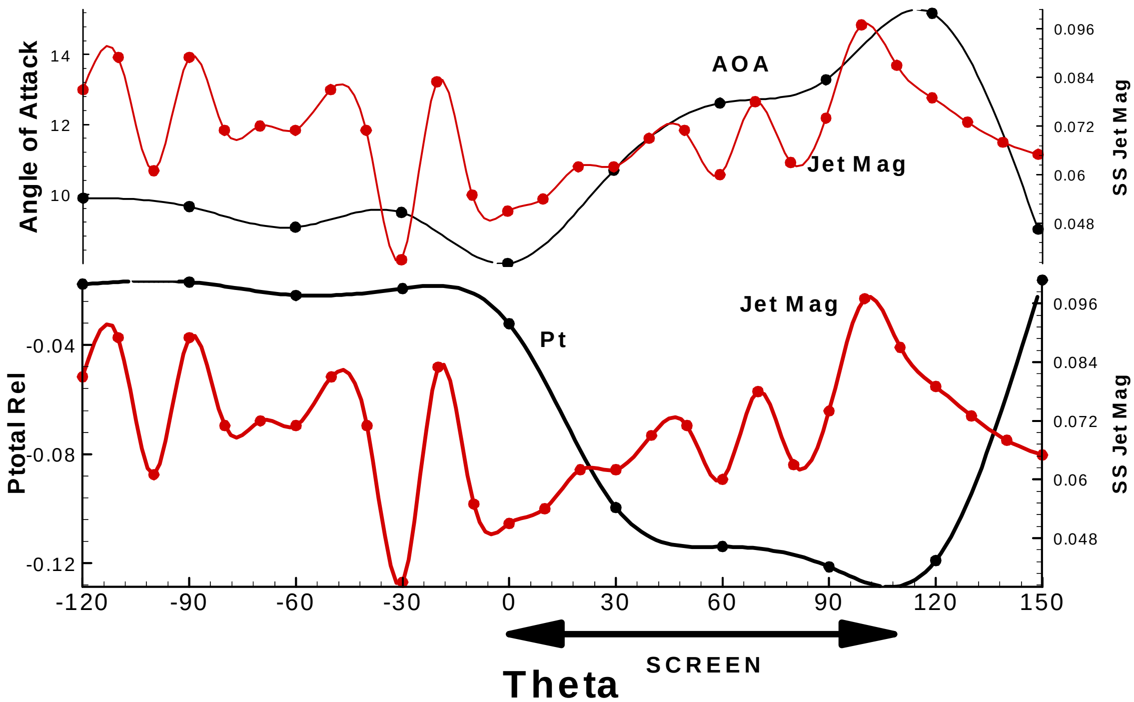

Figure 4.12: Suction Side Jet Relative Magnitude vs. Input Drivers for Operating Point A at 50 % Span.

Figure 4.13 compares changes in wake semi-width with the inlet drivers for operating point A at 50 % span. Interestingly, the wake semi-width begins to increase 40° prior to the drop in inlet total pressure. Wake semi-width then continues to increase until peaking 80° into the distortion screen, which is exactly where the suction side jet semi-width peaks. This parameter is 30° in advance of the peak angle of attack.

Figure 4.14 compares wake defect relative magnitude with the inlet drivers for operating point A at 50 % span. The defect magnitude is flat until the leading edge of the distortion screen and is in phase with changes in the inlet relative total pressure profile. It then steadily increases in magnitude until peaking 80° into the distorted region, once again 10° out of phase with the peak in the relative inlet total pressure 90° into the screen and 30° in advance of the peak angle of attack. One observes from Figures 4.13 and 4.14 that there are strong relationships between the wake semi-width and magnitude with respect to the inlet drivers.

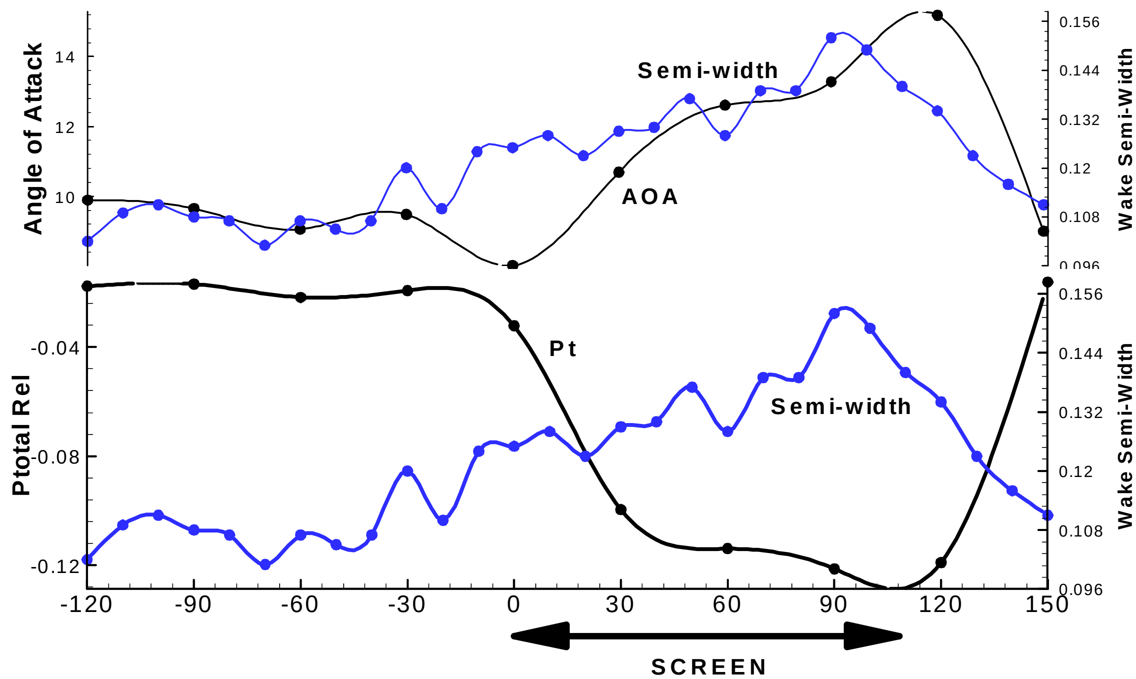

Figure 4.13: Wake Semi-Width vs. Input Drivers for Operating Point A at 50 % Span.

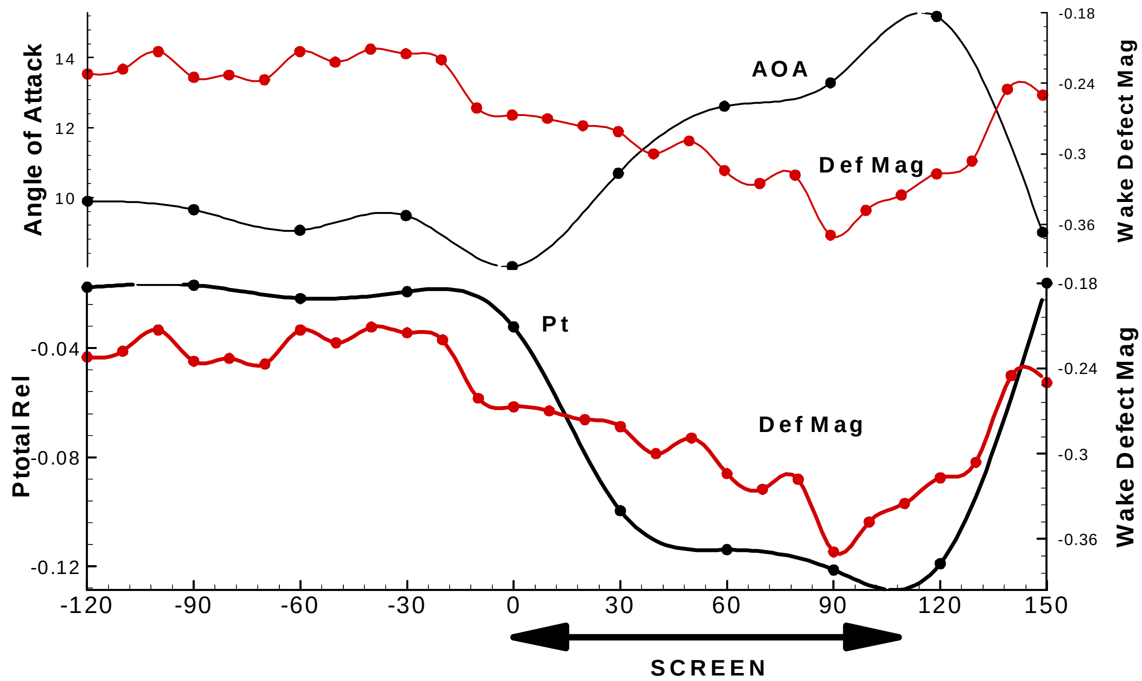

Figure 4.14: Wake Defect Relative Magnitude vs. Input Drivers for Operating Point A at 50 % Span.

Figure 4.15 compares rotor exit flow median total pressure with corresponding changes in the input drivers for operating point A at 50 % span. The median exit total pressure has an unexplained dip 60° prior to the leading edge of the distorted region. It then begins to decrease 20° in advance of the decrease in the inlet total pressure as the screen leading edge is approached. Interestingly, exit median total pressure recovers 20° in advance of the inlet total pressure recovery after the trailing edge of the distortion screen. The decrease and recovery of the exit median total pressure are also 20° in advance of the increase and subsequent decrease in angle of attack as the blade enters and leaves the distortion screen. Strong correlation is obvious between the exit total pressure profile and the inlet drivers.

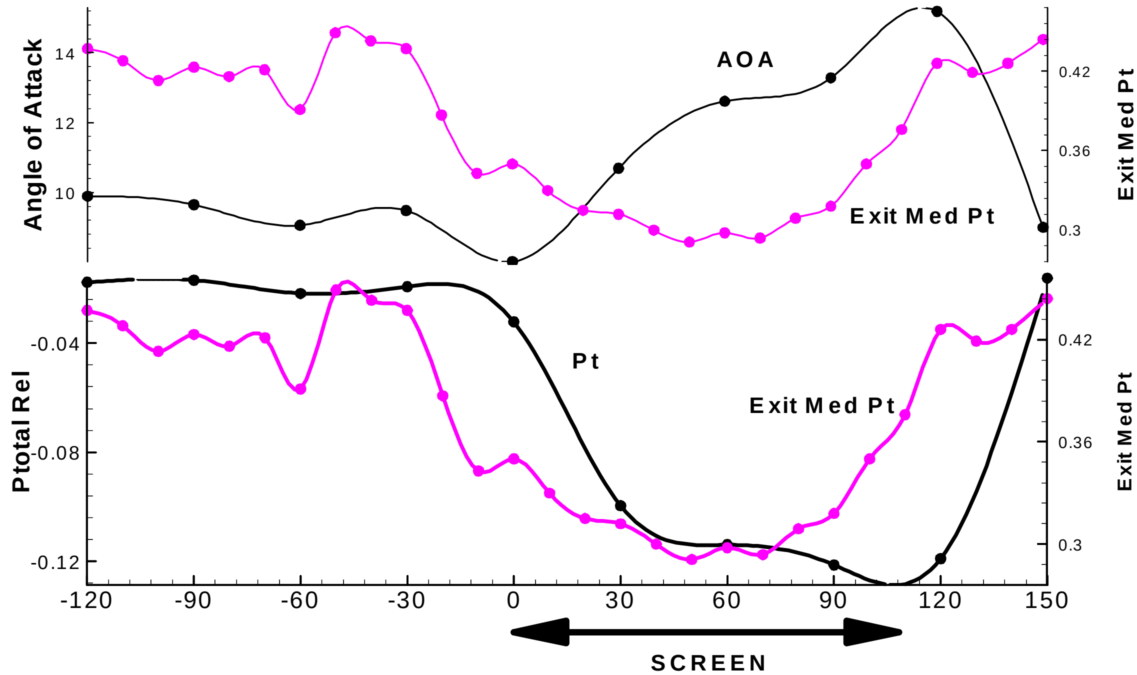

Figure 4.15: Rotor Exit Median Total Pressure vs. Input Drivers for Operating Point A at 50 % Span.

Figure 4.16 presents the suction side jet semi-width as compared with the input drivers for operating point A at 33 % span. The inlet total pressure profile is relatively flat although it begins to decrease slightly 90° prior to the screen. There is no obvious peak in the magnitude of the inlet total pressure profile although it has its greatest values 60° to 90° into the screen. Meanwhile, the suction side jet semi-width varies a great deal outside the distorted region and has a slight increase which is in phase with the slight drop in total pressure 60° prior to the screen. The jet semi-width is lowest 40° to 20° in advance of the distorted region, then increases in phase with decreases in the inlet total pressure profile. It then varies a great deal within the distorted region. However, it does have a peak 50° into the screen before returning back to its undistorted values in phase with the total pressure recovery after the trailing edge of the screen. The exists stronger correlation between the suction side jet semi-width and the inlet drivers for 33 % span than there were for 50 % span measurements at the same operating point.

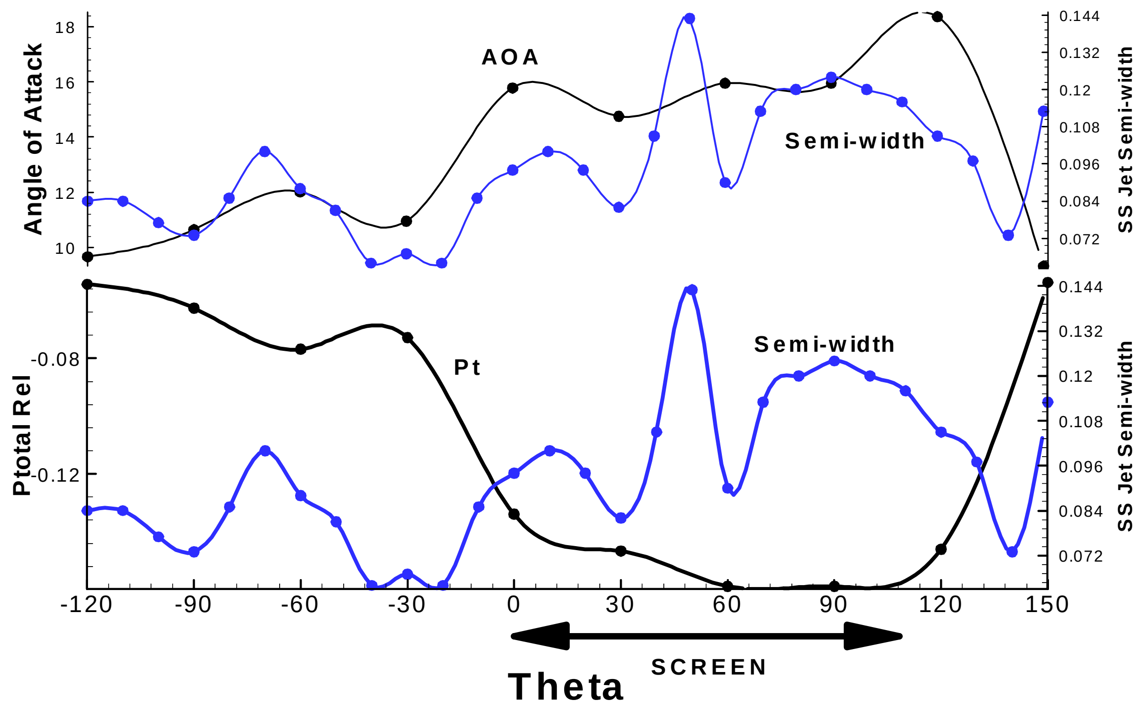

Figure 4.16: Suction Side Jet Semi-Width vs. Input Drivers for Operating Point A at 33 % Span.

In addition, the suction side jet semi-width undergoes trends which are almost exactly in phase with changes in the inlet angle of attack. Both have a slight peak 60° in advance of the distortion screen and begin to steadily increase 10° in advance of the screen leading edge. Both parameters then dip slightly 20° to 30° into the screen before peaking 60° out of phase, with the latter peak in the angle of attack 10° after the trailing edge of the screen. Once again, the suction side jet semi-width is fairly well correlated to the inlet drivers.

Figure 4.17 presents suction side jet relative magnitude as compared with the input drivers for operating point A at 33 % span. The suction side jet magnitude experiences a slight increase 60° in advance of the screen. It then remains relatively flat until going quite high 80° into the screen to 10° after the trailing edge of the screen, with a peak 90° into the screen. This peak corresponds to the minimum total pressure at the rotor inlet, although it is 20° in advance of the peak angle of attack. Again, poor correlation exists between the suction side jet magnitude and the inlet drivers.

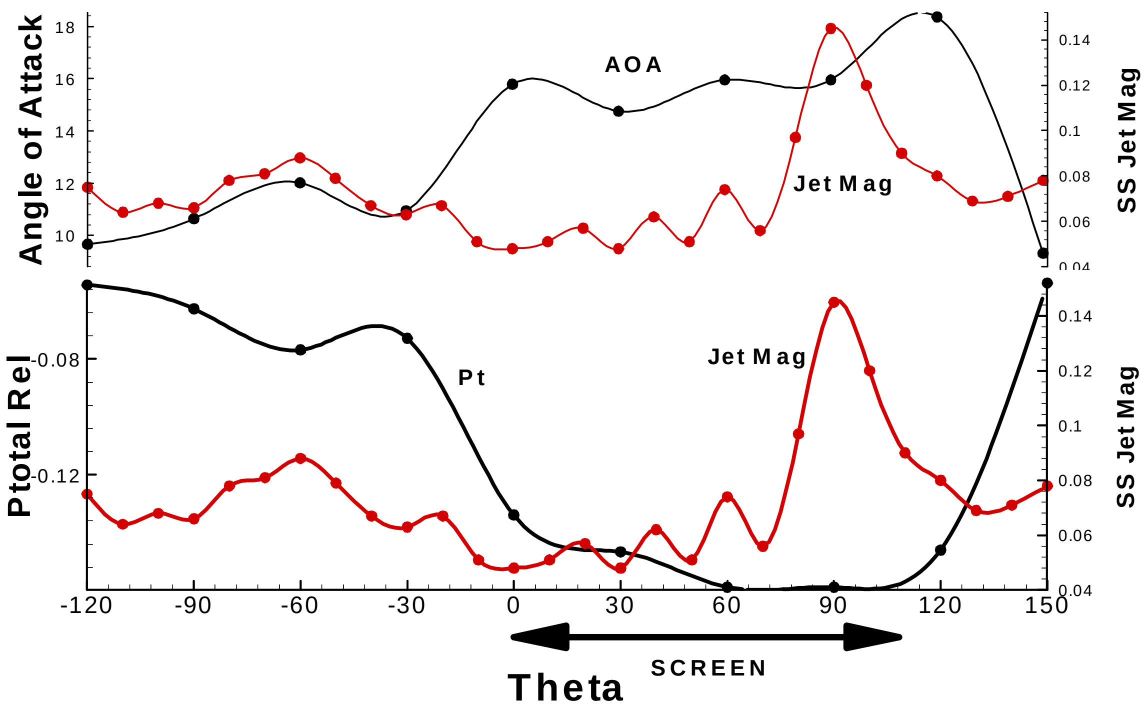

Figure 4.17: Suction Side Jet Relative Magnitude vs. Input Drivers for Operating Point A at 33 % Span.

Figure 4.18 presents the wake semi-width as compared with the input drivers for operating point A at 33 % span. Changes in wake semi-width and inlet total pressure are exactly in phase approaching the screen, although peaks in their respective magnitudes are 50° out of phase, with the wake semi-width in advance. Changes in wake semi-width and angle of attack are also exactly in phase, although in this case the peak in wake semi-width occurs 60° in advance. Strong correlation exists between the wake semi-width and the inlet drivers.

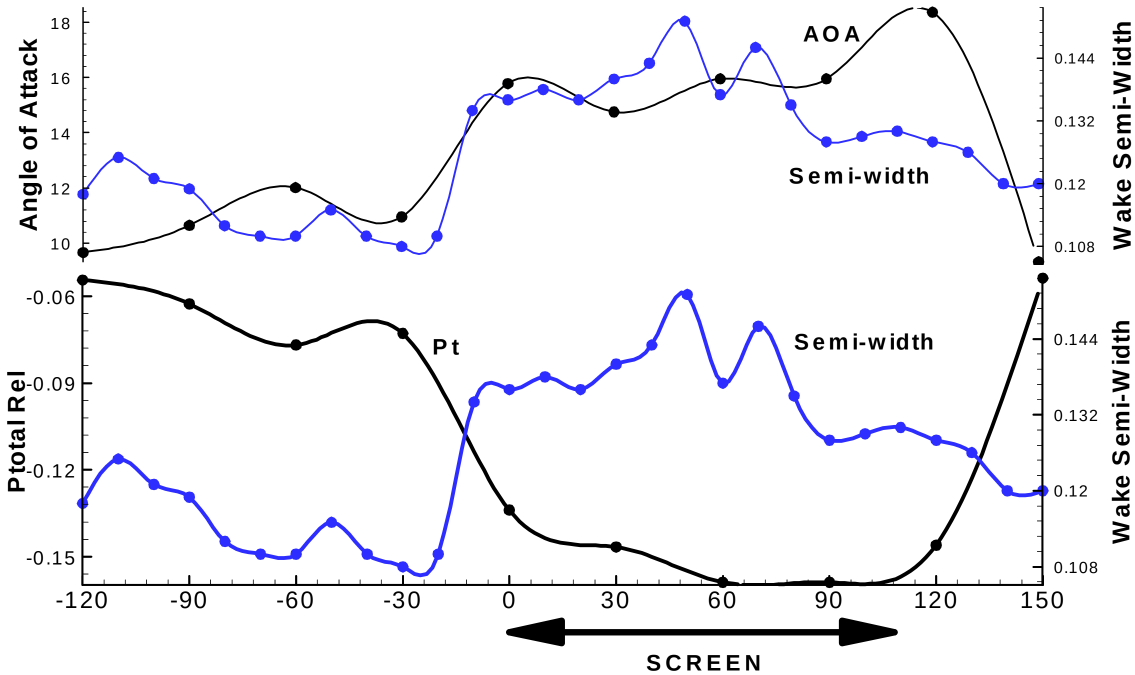

Figure 4.18: Wake Semi-Width vs. Input Drivers for
Operating Point A at 33 % Span.

Figure 4.19 presents wake defect relative magnitude as compared with input drivers for operating point A at 33 % span. The slight decrease in inlet total pressure 60° in advance of the screen is in phase with the slight decrease in wake defect magnitude. Both values then increase slightly before decreasing as the screen is approached, with the inlet total pressure decrease 30° in advance of the increase in the wake defect magnitude. The wake defect magnitude also lagged 30° behind the increase in angle of attack as the blade passed into the screen. This may indicate that blade exit flow response to an unsteady relative inlet condition is more evident at the hub than at other regions of the blade, as evidenced by the time lag that one-dimensional downstream total pressure parameters adjust to varying inlet conditions. The wake defect relative magnitude appears to have poor correlation with the inlet drivers.

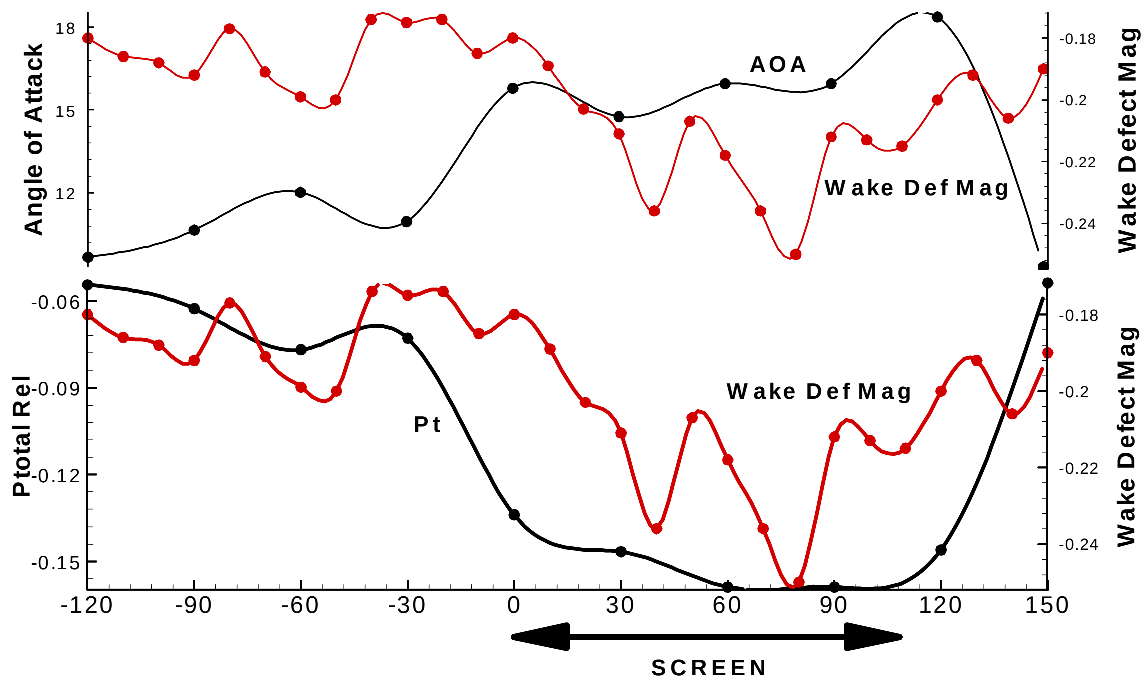

Figure 4.19: Wake Defect Relative Magnitude vs. Input Drivers for Operating Point A at 33 % Span.

Figure 4.20 depicts rotor exit median total pressure versus input drivers for operating point A at 33 % span. The changes in exit total pressure with respect to inlet total pressure are exactly in phase as the blade approaches the screen, although the inlet total pressure recovery after the trailing edge of the screen lags 30° behind the exit total pressure recovery. These results indicate poor attenuation of the distortion through the rotor. Changes in exit median total pressure are exactly in phase with the inlet angle of attack as well, although once again the exit median total pressure recovery leads the angle of attack return to its undistorted value by 30°. As before, strong correlation exists between the exit total pressure profile and the inlet drivers.

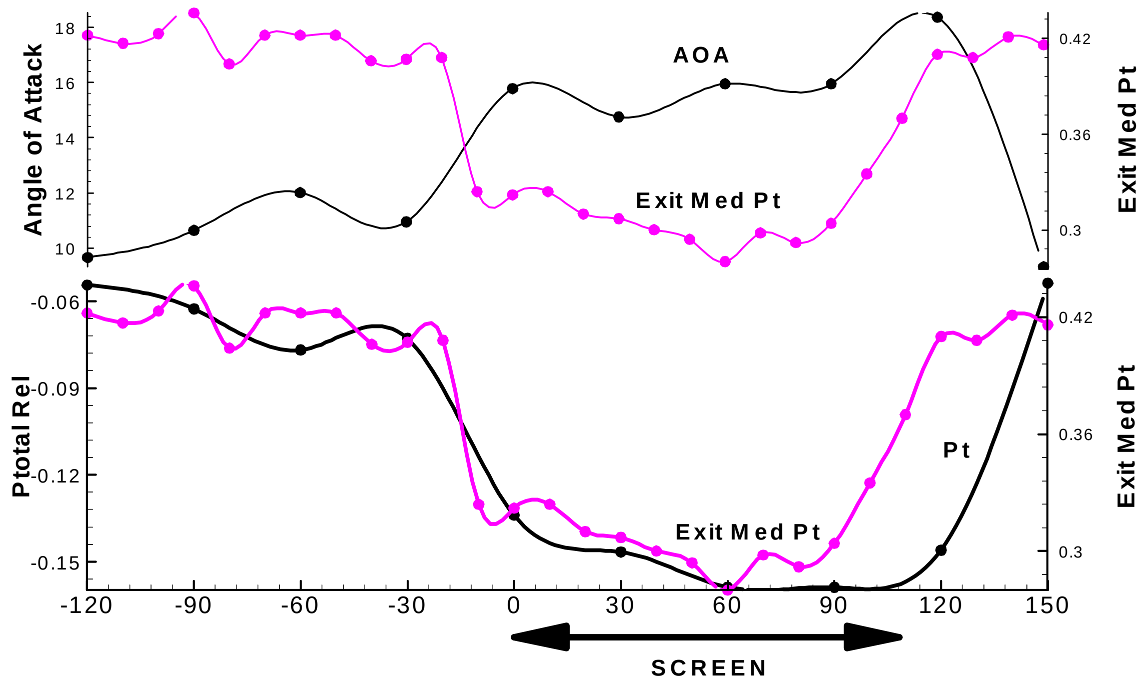

Figure 4.20: Rotor Exit Median Total Pressure vs. Input Drivers for Operating Point A at 33 % Span.

Figure 4.21 depicts the suction side jet semi-width as compared with input drivers for operating point A at 67 % span. Although the jet semi-width measurement is quite random outside of the distorted region, it is exactly in phase with the inlet total pressure profile after the leading edge of the screen is reached. It also has exactly the same phase as the angle of attack to the blades, although it has a high-magnitude region 40° to 90° into the screen, whereas the angle of attack simply peaks 90° into the screen. As with the other measurement spans, the suction side jet semi-width has only moderate correlation with the inlet drivers.

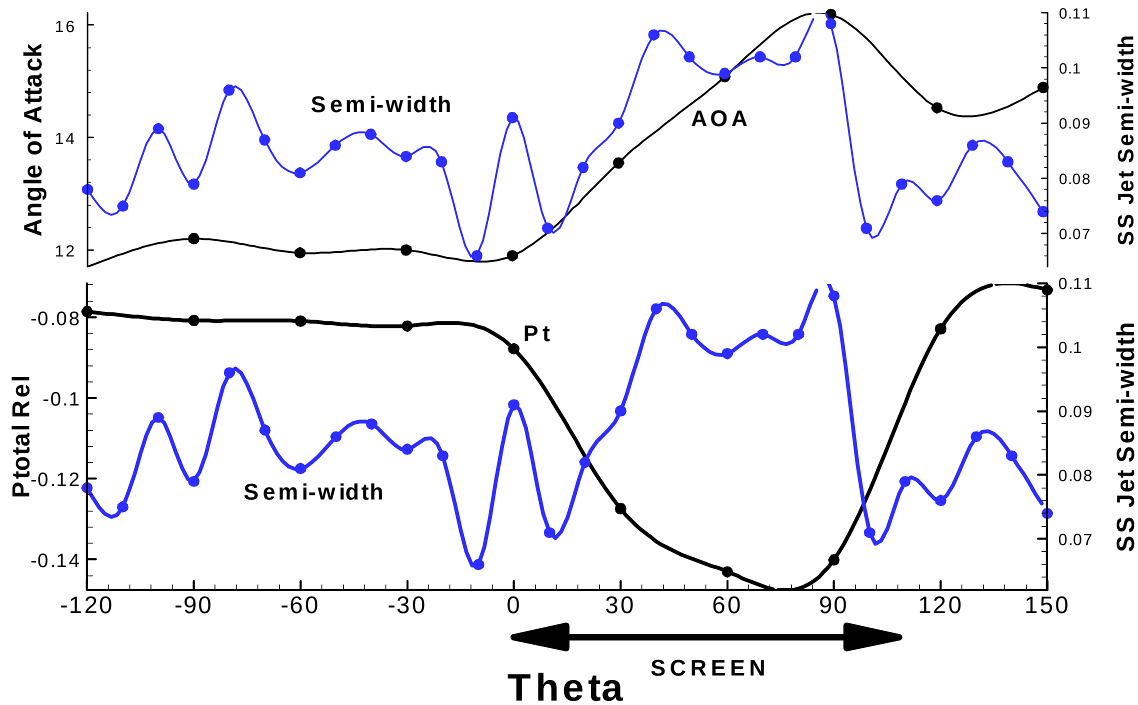

Figure 4.21: Suction Side Jet Semi-Width vs. Input Drivers for Operating Point A at 67 % Span.

Figure 4.22 depicts the suction side jet relative magnitude as compared to the inlet drivers for operating point A at 67 % span. The jet magnitude is relatively flat until unexpectedly dropping 10° prior to the screen. It is then quite random throughout the distorted region, and inexplicably has values lower than the undistorted magnitudes. Nowhere in this circumferential flow survey do suction side jet magnitude values appear to correspond to inlet total pressure or angle of attack values. Correlation to the inlet drivers as evidenced by this figure is extremely poor.

Figure 4.23 presents the wake semi-width as compared to the input drivers for operating point A at 67 % span. The wake semi-width begins to increase 20° in advance of the inlet total pressure change at the leading edge of the screen, and their peak values coincide 80° into the screen. Its return to undistorted values is exactly in phase as well. The wake semi-width increase is 20° ahead of the increase in angle of attack as the distortion screen is approached. Then they both peak 80° into the screen before returning in phase to their undistorted values. Once again, strong correlation is evident between the wake semi-width and the inlet drivers.

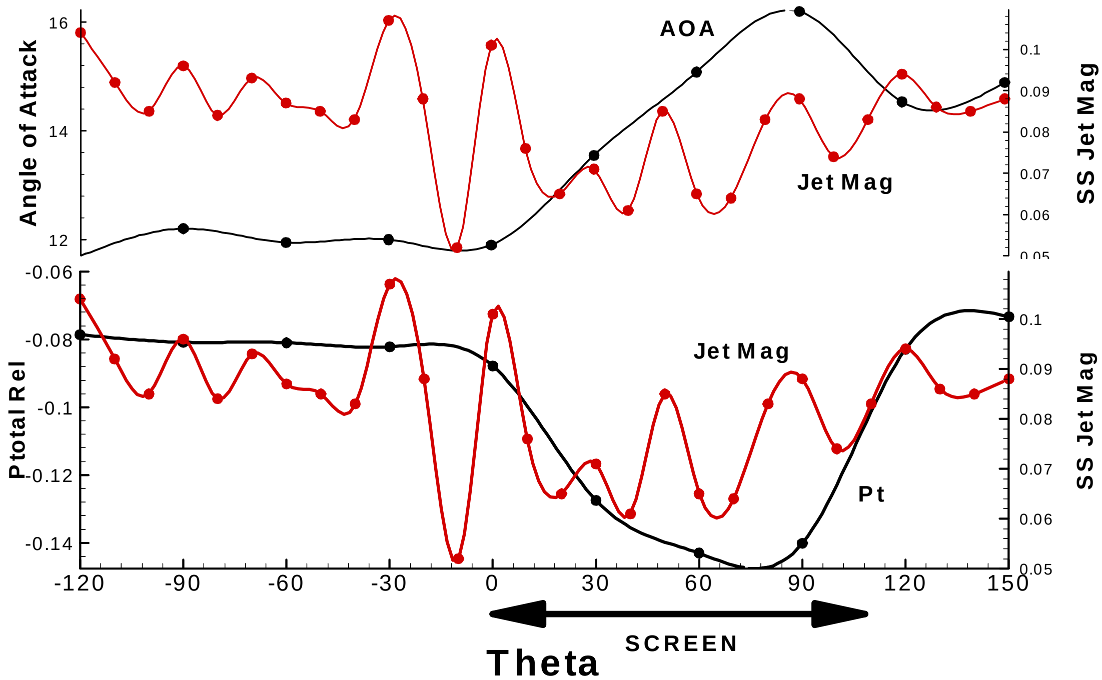

Figure 4.22: Suction Side Jet Relative Magnitude vs. Input Drivers for Operating Point A at 67 % Span.

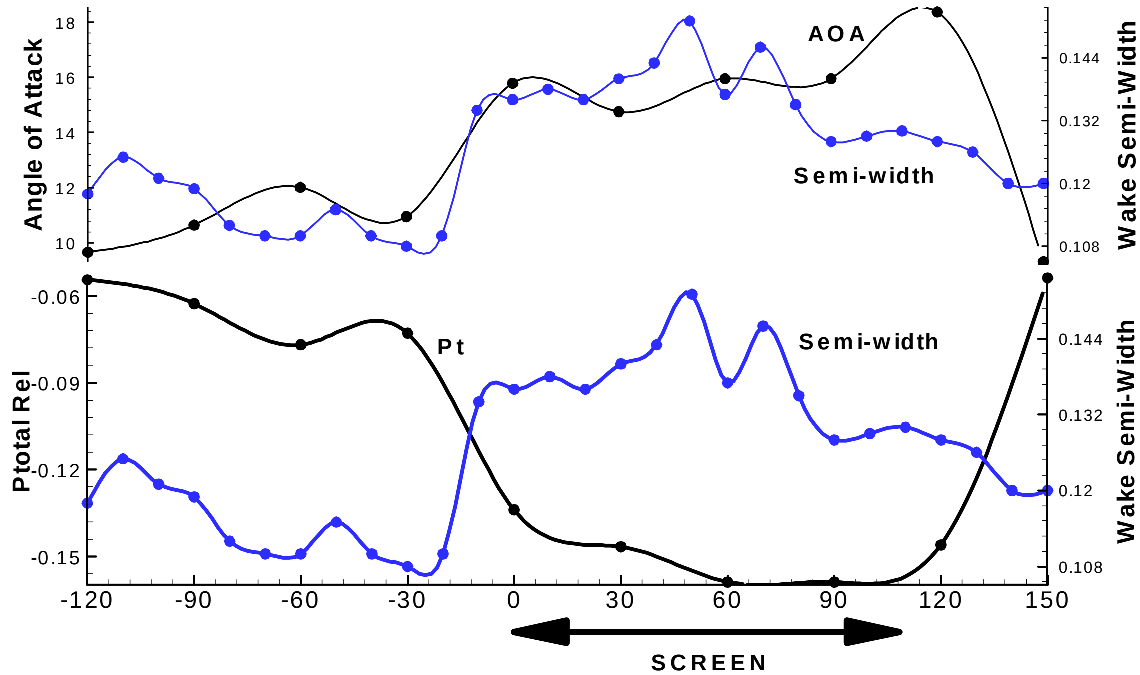

Figure 4.23: Wake Semi-Width vs. Input Drivers for
Operating Point A at 67 % Span.

Figure 4.24 presents the wake defect relative magnitude as compared to the input drivers for operating point A at 67 % span. The phase for changes in values of the inlet total pressure profile, angle of attack, and wake defect magnitude are identical throughout the circumferential flow survey. This suggests extremely strong correlation between the wake defect magnitude and the inlet drivers, as was true for the 50 % and 33 % measurement spans.

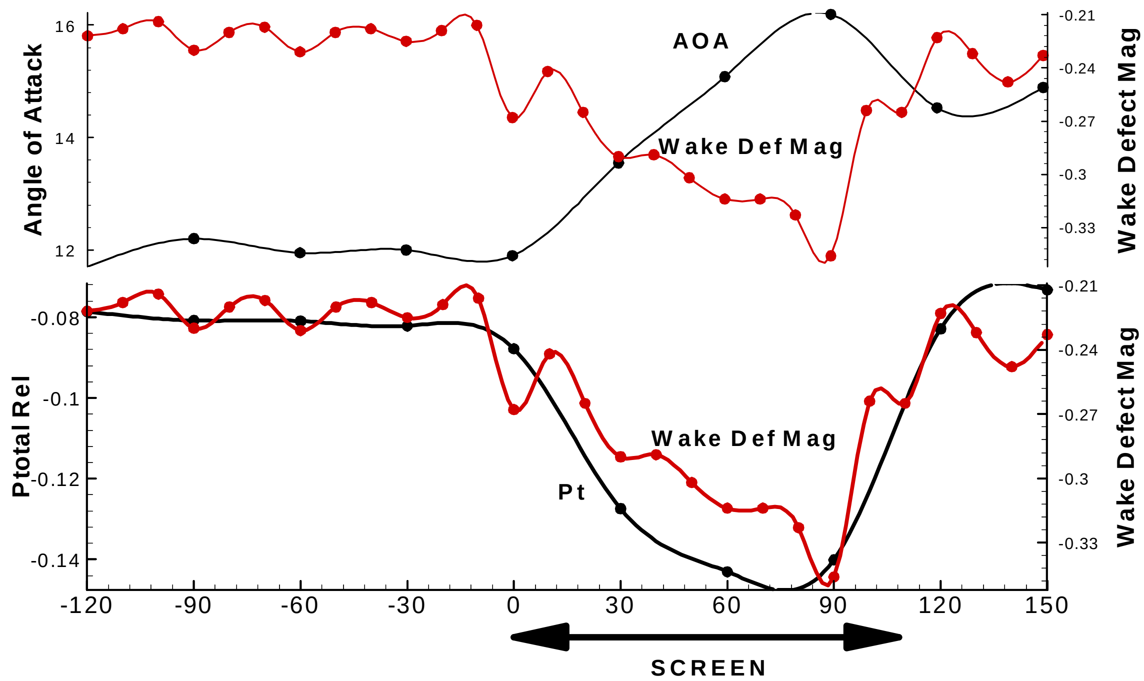

Figure 4.24: Wake Defect Relative Magnitude vs. Input Drivers for Operating Point A at 67 % Span.

Figure 4.25 depicts the rotor exit median total pressure as compared to inlet drivers for operating point A at 67 % span. Changes in inlet and exit total pressure profiles are in phase, although the maximum total pressure loss at the inlet occurs 40° after the minimum exit median total pressure. The identical trending is true for angle of attack as compared to exit median total pressure, suggesting strong correlation between the exit total pressure profile and the inlet drivers.

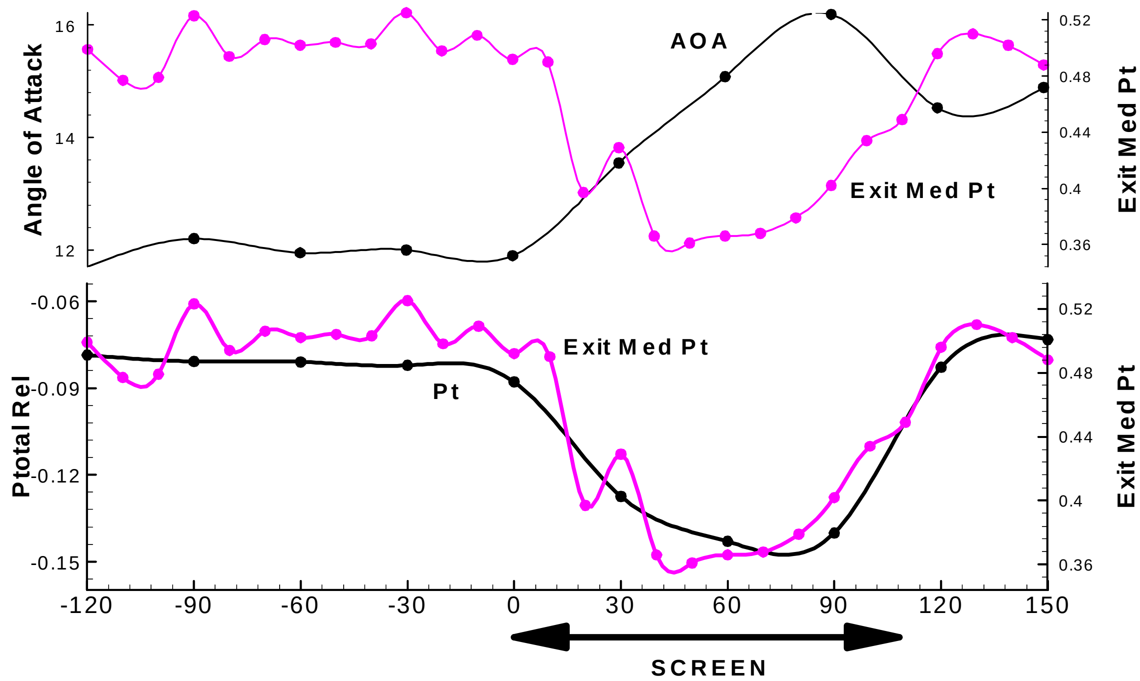

Figure 4.25: Rotor Exit Median Total Pressure vs. Input Drivers for Operating Point A at 67 % Span.

Several trends may be established for the response of the wake parameters with respect to the inlet drivers. They are listed as follows:

- *Suction side jet semi-width* – Varies a great deal in and out of the distorted region, depending on span. Often has the same phase as the inlet drivers, but the peak is usually in advance of them. Poorly correlated to the inlet driving functions for all three measurement spans.
- *Suction side jet relative magnitude* – Varies a great deal within and without the distorted region, depending on span. In one case, it had no correlation with the trends in the inlet drivers. Often peaks 20° in advance of the drivers. Appears to be poorly correlated to the inlet drivers for all three measurement spans.
- *Wake semi-width* – Often in phase with both drivers and peaks often coincide as well. Strong correlation is evident for all three measurement spans.

- *Wake defect relative magnitude* – Changes are always in phase with inlet drivers but often peaks in advance of driver peaks. Strong correlation is evident for all three measurement spans.
- *Exit median total pressure* – Trends are usually in phase with inlet drivers. Strong correlation is evident for all three measurement spans.

Analysis of the PSD functions for the exit flow measurements did not reveal the location of the 20 dominant frequencies to be a function of span, loading, or distortion screen.

4.3 Observations Regarding Inlet and Exit Flow Characteristics

A number of general trends in the inlet data were evident for all spans, loadings, and screen levels:

1.) The inlet static pressure profile tends to steadily decrease toward the distortion screen and remain relatively flat throughout the distorted region.

2.) The total pressure is relatively constant until the distorted screen region is entered, when it falls off rapidly and remains flat until peaking at the trailing edge of the distortion screen and returning to the undistorted total pressure value after exiting the distortion screen.

3.) The flow pitch angle tends to dip below the undistorted pitch angle prior to entering the distorted region. After entering the distorted region, it exceeds the undistorted value and peaks toward the trailing edge of the screen before returning to the its undistorted value outside of the screen.

4.) Angle of attack typically follows the same trend as does the flow pitch angle.

Similar to the rotor inlet flow characteristics, a number of general trends in the one-dimensional exit total pressure data were obvious for all spans, loadings, and screen levels:

1.) The non-dimensional suction side jet thickness remains relatively flat until peaking at or immediately after the trailing edge of the distorted region.
2.) The non-dimensionalized wake thickness was relatively flat until increasing through the distorted region and peaking at the trailing edge. This is indicative of boundary layer thickening on the suction side of the blades.
3.) The wake relative maximum depth is relatively constant until becoming much deeper through the distorted region and becoming greatest at the trailing edge of the distortion and returning to its original undistorted value.
4.) The median total pressure at the rotor exit indicates poor attenuation of the distortion through an isolated rotor, following the same trends as the rotor inlet total pressure profile.

In addition to the general trends of the rotor inlet and exit flow conditions it was possible to qualitatively analyze the three differing effects of varying span, loading, and distortion screen intensity on each of the rotor inlet and exit flow parameters. A description of the changing rotor inlet and exit flow parameter profiles with respect to the three experimental conditions is as follows:

a.) Effect of changing blade measurement span:

Inlet Static Pressure – No observable change in loss magnitude and little change in profile.
Inlet Total Pressure – Highest loss at mid-span where axial velocity is highest outside of the hub and tip boundary layers.

Inlet Flow Pitch Angle – Lowest at mid-span, very high at hub and tip.

Inlet Flow Angle of Attack – Lowest at mid-span, highest at hub and tip.

Suction Side Jet Thickness – Little observable change.

Suction Side Jet Relative Maximum – Little observable change.

Wake Thickness – Thickest near hub, smallest at tip.

Wake Relative Maximum Depth – Defect more pronounced with increasing span.

Exit Median Total Pressure – Highest toward tip region.

b.) Effect of changing loading:

Inlet Static Pressure – As loading is increased, static pressure loss decreases due to decreased axial flow velocity.

Inlet Total Pressure – As loading is increased, total pressure loss decreases due to decreased axial flow velocity.

Inlet Flow Pitch Angle – Increases with higher loading.

Inlet Flow Angle of Attack – Increases with higher loading.

Suction Side Jet Thickness – No observable change.

Suction Side Jet Relative Maximum – No observable change.

Wake Thickness – Increases with higher loading.

Wake Relative Maximum Depth – Defect increases with higher loading.

Exit Median Total Pressure – No observable change.

c.) Effect of changing screen distortion intensity:

Inlet Static Pressure – Increased distortion intensity increases static pressure drop.

Inlet Total Pressure – Increased distortion intensity increases total pressure drop.

Inlet Flow Pitch Angle – Higher when behind more intense distortions.

Inlet Flow Angle of Attack – Higher when behind more intense distortions.

Suction Side Jet Thickness – No observable change.

Suction Side Jet Relative Maximum – No observable change.

Wake Thickness – Increases when behind more intense distortions.

Wake Relative Maximum Depth – As distortion intensity increases, has a much greater defect in the distorted region.

Exit Median Total Pressure – Lower overall for more intense distortion and greater defect behind less porous screen.

5. CONCLUSIONS

The results of the present investigation have shown that based on a one-dimensional unsteady exit total pressure flow survey, blade response to an inlet pressure distortion is not a function of span, loading, or distortion intensity. However, the magnitudes of the changes in the inlet and exit flow parameters are functions of span, loading, and distortion intensity.

In addition, it was noted that as blade loading was increased, the suction side total pressure excess as measured in the stationary frame of reference increased in both thickness and magnitude. This appeared to be a response to corresponding increases in wake thickness and magnitude of wake total pressure defect. Suction side jet semi-width and magnitude varied a great deal within and without the distorted region and were poorly correlated to inlet flow conditions. For inlet angles of attack which exceeded the steady-state stalling angle, wake semi-width and momentum defects were extremely high, possibly indicating the presence of dynamic stalling of the blade boundary layers. Wake semi-width and magnitude parameters were strongly correlated to the inlet flow conditions of total pressure loss and angle of attack.

6. RECOMMENDATIONS

The following recommendations are submitted with respect to future dynamic wake studies in axial-flow fans and compressors:

- Perform the same experiment on a higher pressure ratio or transonic fan or compressor with a range from lightly loaded to pre-stall operation.
- Perform a higher resolution circumferential inlet flow survey in the transition regions at the leading and trailing edges of the distortion screen. This will allow more accurate determination of the wake parameter response with respect to the rotor inlet driving functions of total pressure loss and angle of attack.
- Perform a spanwise survey with a high-frequency response pressure transducer between the distortion screen and the rotor to quantify the unsteady interaction between the distortion screen and the inlet flow.
- Perform a three-dimensional thermal anemometry velocity survey in the wake of the same machine at a higher speed. This work is already in pursuit in the Mechanical Engineering Department of Virginia Tech.
- Employ signal analysis methods to determine the degree of correlation and phase shift between the various flow parameters.

7. REFERENCES

Cited Works

1. Boytos, J.F. "State-of-the-Art Review: Aircraft Gas Turbines – Inlet Distortion Indices." NAPTC-PE-95, March 1977.

2. Viswanath, K., Govardhan, M. "Effect of Circumferential Inlet Flow Distortion and Swirl on the Flow Field of an Axial Flow Fan Stage." ASME Paper No. 96-GT-263, 1996.

3. Andrew, Philip L. "An Experimental Investigation of Unsteady Loss Variation with Reduced Frequency in a Low Speed, Single Stage Axial Compressor." VKI Project Report 1988-07.

4. Kimzey, W.F. "An Analysis of the Influence of Some External Disturbances on the Aerodynamic Stability of Turbine Engine Axial Flow Fans and Compressors." AEDC-TR-77-80, August 1977.

5. Calogeras, J.E., Mehalic, C.M., Burstadt, P.L., "Experimental Investigation of the Effect of Screen-Induced Total-Pressure Distortion on Turbojet Stall Margin." NASA TMX-2239, March 1971.

6. Yocum, A.M. "An Experimental and Numerical Investigation of the Performance of Compressor Cascades with Stalled Flow." Ph.D. Dissertation, Virginia Polytechnic Institute & State University, Blacksburg, Virginia, 1988.

7. McCarthy, J.H. "Steady Flow Past Non-Uniform Wire Grids." Journal of Fluid Mechanics, Vol. 19, 1964.

8. Soeder, R.H., Bobula, G.A. "Effect of Steady-State Pressure Distortion on Flow Characteristics Entering a Turbofan Engine." NASA TM 79134, April, 1979.

9. Cousins, W.T., "Techniques for the Analysis of Unsteady Pressure Measurements in an Axial-Flow Compressor." M.S. Thesis, Virginia Polytechnic Institute & State University, Blacksburg, Virginia, 1979.

10. Gauden, W.H. "Performance and Stalling Behavior of an Axial-Flow Compressor Subjected to Three Circumferential Inlet Distortion Levels." M.S. Thesis, Virginia Polytechnic Institute & State University, 1977.

11. Dancy, B.B. "Performance and Stalling Behavior of an Axial Flow Compressor With Circumferential Inlet Flow Distortion." M.S. Thesis, Virginia Polytechnic Institute & State University, Blacksburg, Virginia, 1976.

12. Sexton, M.R. "An Investigation of the Dynamic Stalling Characteristics of Rotating Axial-Flow Compressor Blades." Ph.D. Dissertation, Virginia Polytechnic Institute & State University, Blacksburg, Virginia, 1980.

13. Neal, T.E. "The Lift Response of a Rotating Blade of an Axial-Flow Compressor to Inlet Flow Distortion." M.S. Thesis, Virginia Polytechnic Institute & State University, Blacksburg, Virginia, 1975.

14. Melick, H.C., "Analysis of Inlet Flow Distortion and Turbulence Effects on Compressor Stability." NASA CR 114577, 1973.

15. Henderson, R.E., and Horlock, J.H., "An Approximate Analysis of the Unsteady Lifts on Airfoils in a Cascade." ASME Paper No. 72-GT-5, 1972.

16. Fox, R.W., McDonald, A.T. <u>Introduction to Fluid Mechanics</u>, Ed. 4. John Wiley and Sons, Inc. New York. 1992.

17. Reynolds, B. and Lakshminarayana, B. "Characteristics of Lightly Loaded Fan Rotor Blade Wakes." NASA CR-3188, October, 1979.

18. Lakshminarayana, B., Govindan, T.R., Reynolds, B. "Effects of Rotation and Blade Incidence on the Properties of the Turbomachinery Rotor Wake." AIAA Paper No. 81-0054, AIAA 19th Aerospace Sciences Meeting, January 12-15, 1981 St. Louis, Missouri.

19. Shreeve, R.P., Neuhoff, F. "Measurements of the Flow From a High-Speed Compressor Rotor Using a Dual Probe Digital Sampling (DPDS) Technique." ASME Journal of Engineering for Gas Turbines and Power, Vol. 106 pp. 366-375, April 1984.

20. Henderson, R.E., Shen, I.C. "The Influence of Unsteady Rotor Response on a Distorted Flow Field." ASME Paper No. 81-GT-185, International Gas Turbine Conference and Products Show, March 9-12, 1981 Houston, Texas.

21. Reynolds, B., Lakshminarayana, B., and Ravindranath, A. "Characteristics of the Near Wake of a Compressor Rotor." AIAA Paper No. 78-1141, AIAA 11th Fluid and Plasma Dynamics Conference, July 10-12, 1978 Seattle, Washington.

22. Ravindranath, A., Lakshminarayana, B. “Mean Velocity and Decay Characteristics of the Near and Far-Wake of a Compressor Rotor Blade of Moderate Loading.” ASME Journal of Engineering for Power, Vol. 102, pp. 535-548, July 1980.

23. Muhlemann, E. “Experimentelle Untersuchungen an einer axialen Geblasestufe,” Mitteilungen Aus Dem Institut fur Aerodynamik, No. 12, 1946.

24. Ufer, H. “Analysis of the Velocity Distribution at the Blade Tips of Axial-Flow Technische Mitteilungen Krupp (Forschung Sberichte), Vol. 26, No. 2, 1968, pp. 33-45, English Translation, NASA TTF-16 366.

25. Kerrebrock, J.L., Epstein, A.H., Haines, D.M., and Thompkins, W.T. “The M.I.T. Blowdown Compressor Facility.” ASME Journal of Engineering for Power, October, 1974 pp. 394-406.

26. Shreeve, R.P., Dodge, F.J., Hawkins, W.R., and Larson, V.J. “Probe Measurements of Velocity and Losses From a Small Axial Transonic Rotor.” AIAA Paper No. 79-1198, AIAA 11th Fluid and Plasma Dynamics Conference, July 10-12, 1978 Seattle, Washington.

27. Shreeve, R.P., Simmons, J.M., West, J.C., and Winters, K.A. “Determination of Transonic Compressor Flow Field by Synchronized Sampling of Stationary Fast Response Transducers.” Nonsteady Fluid Dynamics Proceedings of the Winter Annual Meeting, pp. 91-101, December 10-15, 1978 San Francisco, California.

28. Schmidt, D.P., Okiishi, T.H. “Detailed Measurements of the Periodically Unsteady Flow Produced by Rotor and Stator Wake Interaction in a Multi-stage Turbomachine.” AIAA Paper No. 77-202, AIAA 15th Aerospace Sciences Meeting, January 24-26, 1977 Los Angeles, California.

29. Ng, W.F., Epstein, A.H. “Unsteady Losses in Transonic Compressors.” ASME Journal of Engineering for Gas Turbines and Power, Vol. 107, 1985, pp. 345-353.

30. Cherrett, M.A., Bryce, J.D., and Ginder, R.B. “Unsteady Three-Dimensional Flow in a Single-Stage Transonic Fan: Part I – Unsteady Rotor Exit Flow Field.” ASME Journal of Turbomachinery, Vol. 117, October 1995, pp. 506-513.

31. Colpin, J. Kool, P. “Experimental Study of an Axial Compressor Rotor Transfer Function with Non-Uniform Inlet Flow.” ASME Paper No. 78-GT-69, Gas Turbine Conference and Products Show, April 9-13, 1978 London, England.

32. Mazzawy, R.S., “Multiple Segment Parallel Compressor Model for Circumferential Flow Distortion.” AGARD CP 177, 1975.

33. Carta, F.O., “Analysis of Unsteady Aerodynamic Effects on Axial Flow Compressor Stage with Distorted Inflow.” Project Squid – Techn. Rep. UARL – A – UP, 1972.

34. Hetherington, R., and Moritz, R.R., “Influence of Unsteady Flow Phenomena on the Design and Operation of Aero Engines.” AGARD CP 177, 1975.

35. Verdesoto, G.A. “An Experimental Study of Rotating Stall in an Axial-Flow Compressor.” M.S. Thesis, Virginia Polytechnic Institute & State University, 1977.

36. Treaster, A.L., Yocum, A.M. “The Calibration and Application of Five-hole Probes.” ISA Transactions, Vol. 18, No. 3, 1979 pp. 23-34.

37. Drost, U. “An Experimental Investigation of the Corner Stall Behaviour of a Linear Compressor Cascade at High Angles of Attack.” Diploma Project, Swiss Federal Institute of Technology – Lausanne, February, 1994.

38. Yocum, A.M., Henderson, R.E., “The Effects of Some Design Parameters of an Isolated Rotor on Inlet Flow Distortions." ASME Journal of Engineering for Power, Vol. 102, January 1980 pp. 178-186.

39. Kline, S.J., McClintock, F.A., “Describing Uncertainties in Single Sample Experiments.” Mechanical Engineering, January 1953, pg. 3.

40. Burden, R.L., Faires, J.D. Numerical Analysis, 6th ed. Brooks/Cole. Pacific Grove. 1997.

Uncited Works

41. Calogeras, J.E., Johnsen, R., Burstadt, P., “Effect of Screen-Induced Total Pressure Distortion on Axial Flow Compressor Stability.” NASA TMX-3017, 1974.

42. Hale, A.A., “A 3D Turbine Engine Analysis Compressor Code (TEACC) for Steady-State Inlet Distortion.” Ph.D. Dissertation, Virginia Polytechnic Institute & State University, 1996.

43. Korn, J.A., “Estimated Effect of Circumferential Distortion on Axial Compressors Using Parallel Compressor Theory and Dynamic Stall Delay.” AIAA Paper No. 74-233, 1974.

44. Longley, J.P., Greitzer, E.M. “Inlet Distortion effects in Aircraft Propulsion System Integration.” AGARD-LS-183. Advisory Group for Aerospace Research & Development Lecture Series, May, 1992.

45. Mazzawy, R.S., Banks, G.A. "Modeling and Analysis of the TF30-P-3 Compressor System with Inlet Pressure Distortion." NASA-CR-134996, April, 1976.

46. Mazzawy, R.S., Banks, G.A. "Circumferential Distortion Modeling of the TF30-P-3 Compression System." NASA-CR-135124, January, 1977.

47. Mazzawy, R.S. "Multiple Segment Parallel Compressor Model for Circumferential Flow Distortion." ASME Journal of Engineering for Power, April, 1977.

48. Pearson, H., McKenzie, A., "Wakes in Axial Compressors." *Journal of Royal Aeronautical Society*, Vol. 63, July, 1959.

49. Reid, C. "The Response of Axial Flow Compressors to Intake Flow Distortion." ASME Paper No. 69-GT-29, 1969.

50. Roberts, F., Plourde, G.A., Smakula, F. "Insights into Axial Compressor Response to Distortion." AIAA Paper No. 68-565, 1968.

51. Sexton, M.R., O'Brien, W.F., Moses, H.L., "An On-Rotor Investigation of Rotating Stall in an Axial-Flow Compressor." Unsteady Phenomena in Turbomachinery, AGARD Conference Preprint No. 177, 1975.

52. Shahrokhi, K.A., "Application of Modified Dynamic Compression System Model to a Low-Aspect Ratio Fan: Effects of Inlet Distortion." M.S. Thesis, Vanderbilt University, Nashville, TN, 1995.

53. Steenken, W.G. "Modeling Compression Component Stability Characteristics – Effects of Inlet distortion and Fan Bypass Duct Disturbances." AGARD-CP-324. Advisory Group for Aerospace Research & Development Conference Proceedings, February, 1983.

54. Dominy, R.G., Hodson, H.P., "An Investigation of Factors Influencing the Calibration of Five-Hole Probes for Three-Dimensional Flow Measurements." *Journal of Turbomachinery*, Vol. 115, July 1993.

55. Ehrich, F. "Circumferential Inlet Distortions in Axial Flow Turbomachinery." *Journal of Aeronautical Sciences*, Vol. 24, June 1957.

56. Lakshminarayana, B. "Techniques for Aerodynamic and Turbulence Measurements in *Measurement Methods in Rotating Components of Turbomachinery*. ASME Joint Fluids Engineering Gas Turbine Conference and Products Show, March 10-13, 1980.

57. SAE Aerospace Information Report, AIR-1419, “Inlet Total Pressure Distortion Considerations for Gas Turbine Engines.” May 1983.

58. SAE Aerospace Recommended Practice, ARP-1420. “Gas Turbine Engine Inlet Flow Distortion Guidelines.” March 1978.

59. Seyler, D.R., Gostelow, J.P. “Single Stage Experimental Evaluation of High Mach Number Compressor Rotor Blading Part 2 – Performance of Rotor 1B.” NASA-CR-54582, September, 1967.

8. APPENDIX A

Experimental Data For Undistorted Rotor and Rotor With Distortion Level 1, Level 2, and Level 3

UNDISTORTED DATA

OPERATING POINT A	***33 % Span***	***50 % Span***	***67 % Span***
Angle of Attack	12.6	12.3	12.3
Pitch Angle	20.9	5.3	33.8
Exit Median Total Pressure (non-dim)	0.424	0.486	0.528
Wake Defect Relative Maximum (non-dim)	-0.204	-0.244	-0.241
Wake Semi-Width (non-dim)	0.083	0.089	0.086
Suction Side Jet Relative Maximum (non-dim)	0.114	0.102	0.104
Suction Side Jet Semi-Width (non-dim)	0.095	0.081	0.086

OPERATING POINT B	***33 % Span***	***50 % Span***	***67 % Span***
Angle of Attack	11.1	10.1	11
Pitch Angle	15.3	3.3	25.4
Exit Median Total Pressure (non-dim)	0.418	0.479	0.515
Wake Defect Relative Maximum (non-dim)	-0.191	-0.234	-0.228
Wake Semi-Width (non-dim)	0.063	0.085	0.081
Suction Side Jet Relative Maximum (non-dim)	0.11	0.096	0.105
Suction Side Jet Semi-Width (non-dim)	0.09	0.077	0.08

OPERATING POINT C	***33 % Span***	***50 % Span***	***67 % Span***
Angle of Attack	10.2	8	8.9
Pitch Angle	10.7	2	18
Exit Median Total Pressure (non-dim)	0.414	0.454	0.508
Wake Defect Relative Maximum (non-dim)	-0.185	-0.211	-0.211
Wake Semi-Width (non-dim)	0.054	0.079	0.081
Suction Side Jet Relative Maximum (non-dim)	0.11	0.1	0.088
Suction Side Jet Semi-Width (non-dim)	0.087	0.081	0.074

Figure A.1: Table of Inlet and Exit Flow Characteristics for Undistorted Rotor.

DATA		***LOCATION***	
Distortion Screen	**Operating Point**	**Measurement Span**	**Page Numbers**
Level 1	Operating Point A	50 %, 33 %, 67 %	pp. 92-97
Level 1	Operating Point B	50 %, 33 %, 67 %	pp. 98-103
Level 1	Operating Point C	50 %, 33 %, 67 %	pp. 104-109
Level 2	Operating Point A	50 %, 33 %, 67 %	pp. 110-115
Level 2	Operating Point B	50 %, 33 %, 67 %	pp. 116-121
Level 2	Operating Point C	50 %, 33 %, 67 %	pp. 122-127
Level 3	Operating Point D	50 %, 33 %, 67 %	pp. 128-133

Figure A.2: Table of Locations for Distorted Data.

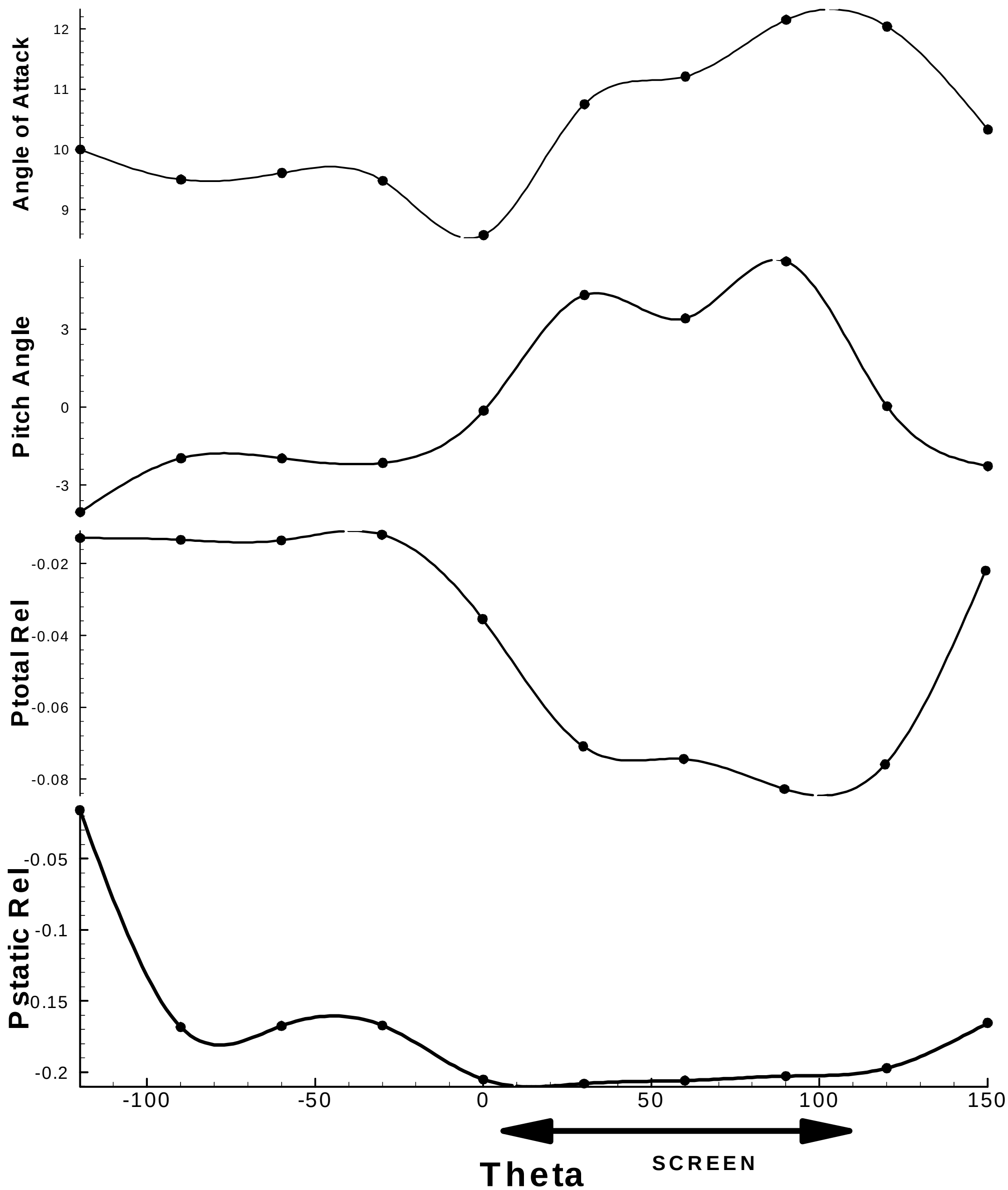

Figure A.3: Inlet Flow Characteristics for Level 1, Operating Point A at 50% Span.

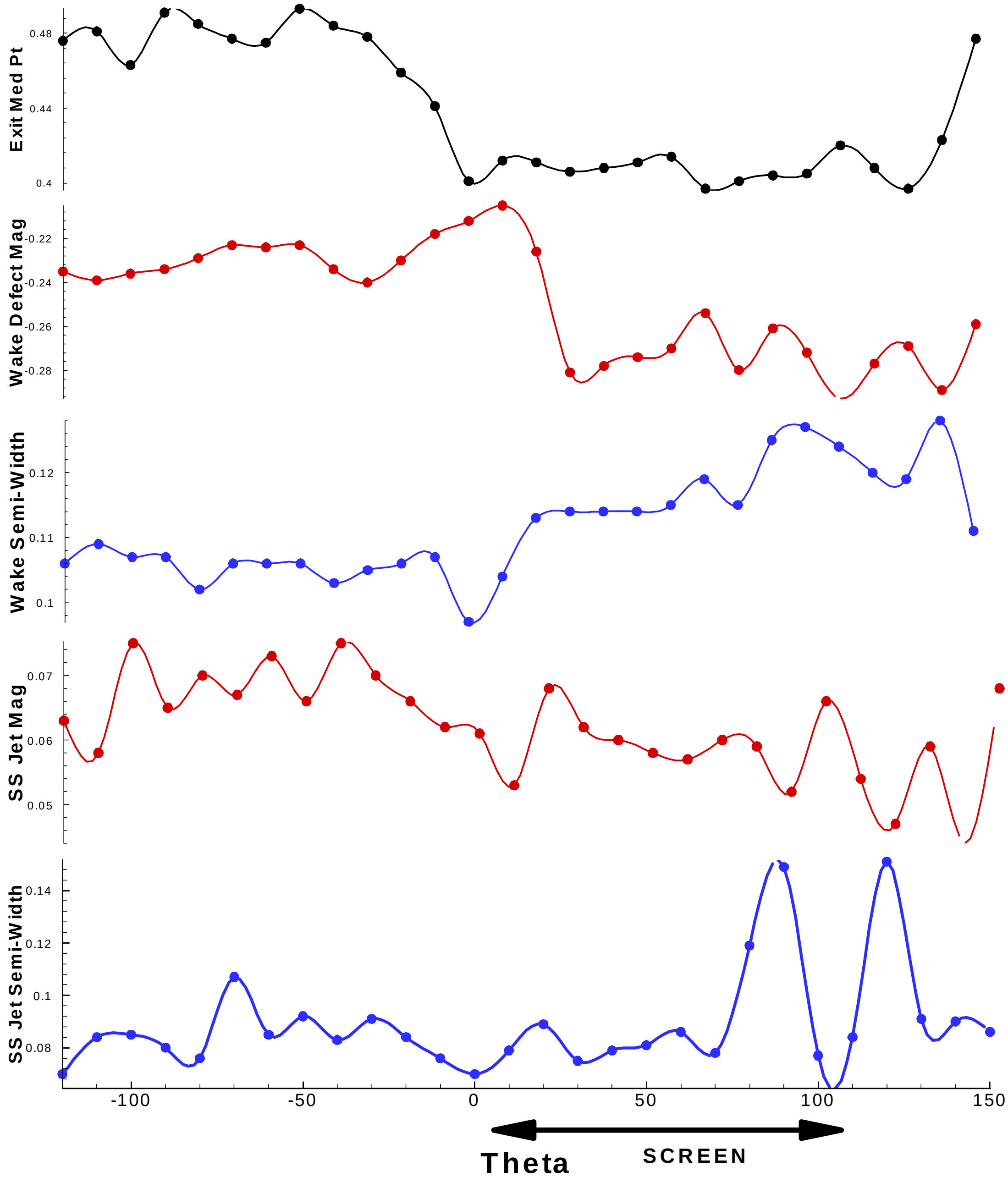

Figure A.4: Exit Flow Characteristics for Level 1, Operating Point A at 50% Span.

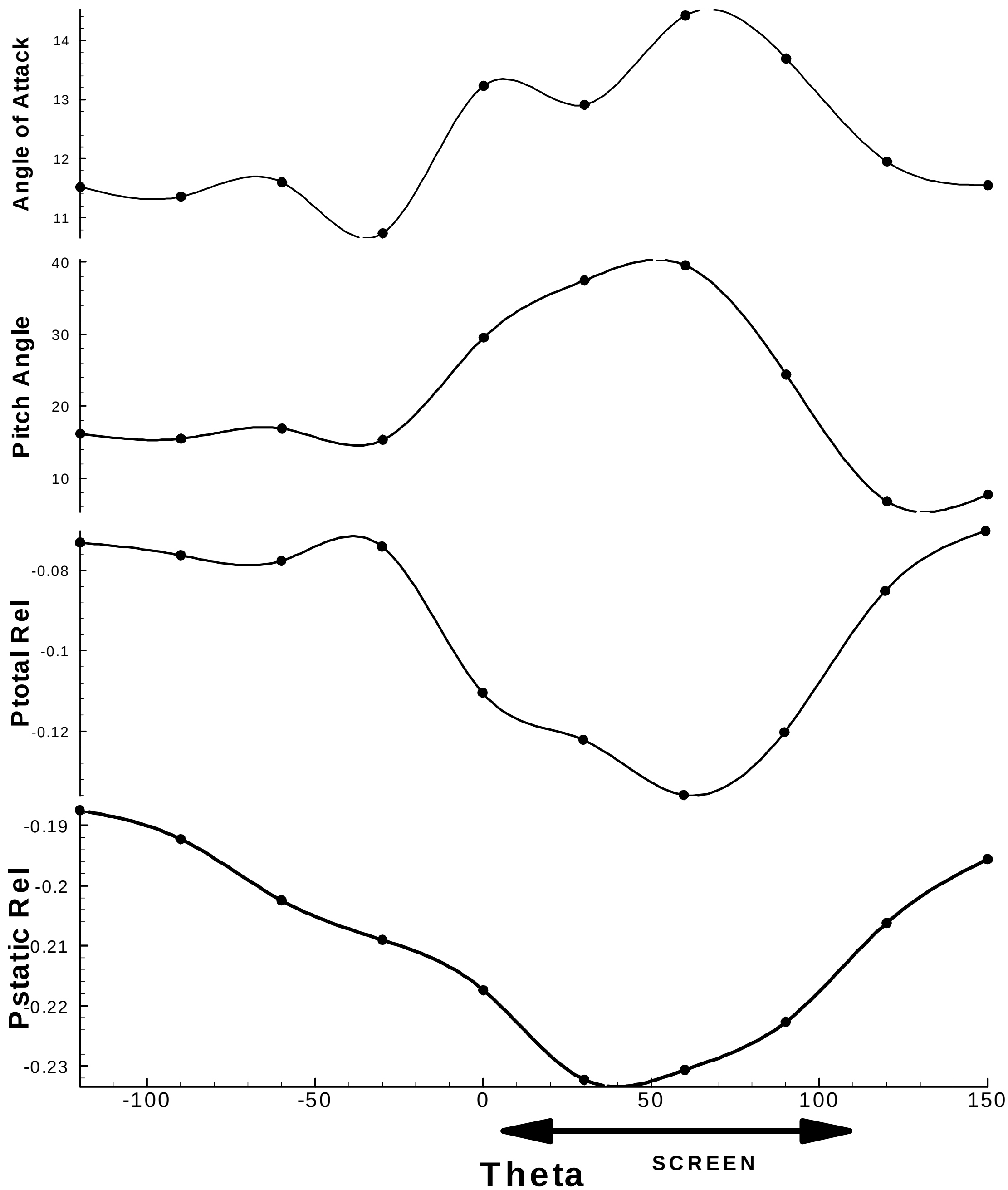

Figure A.5: Inlet Flow Characteristics for Level 1, Operating Point A at 33% Span.

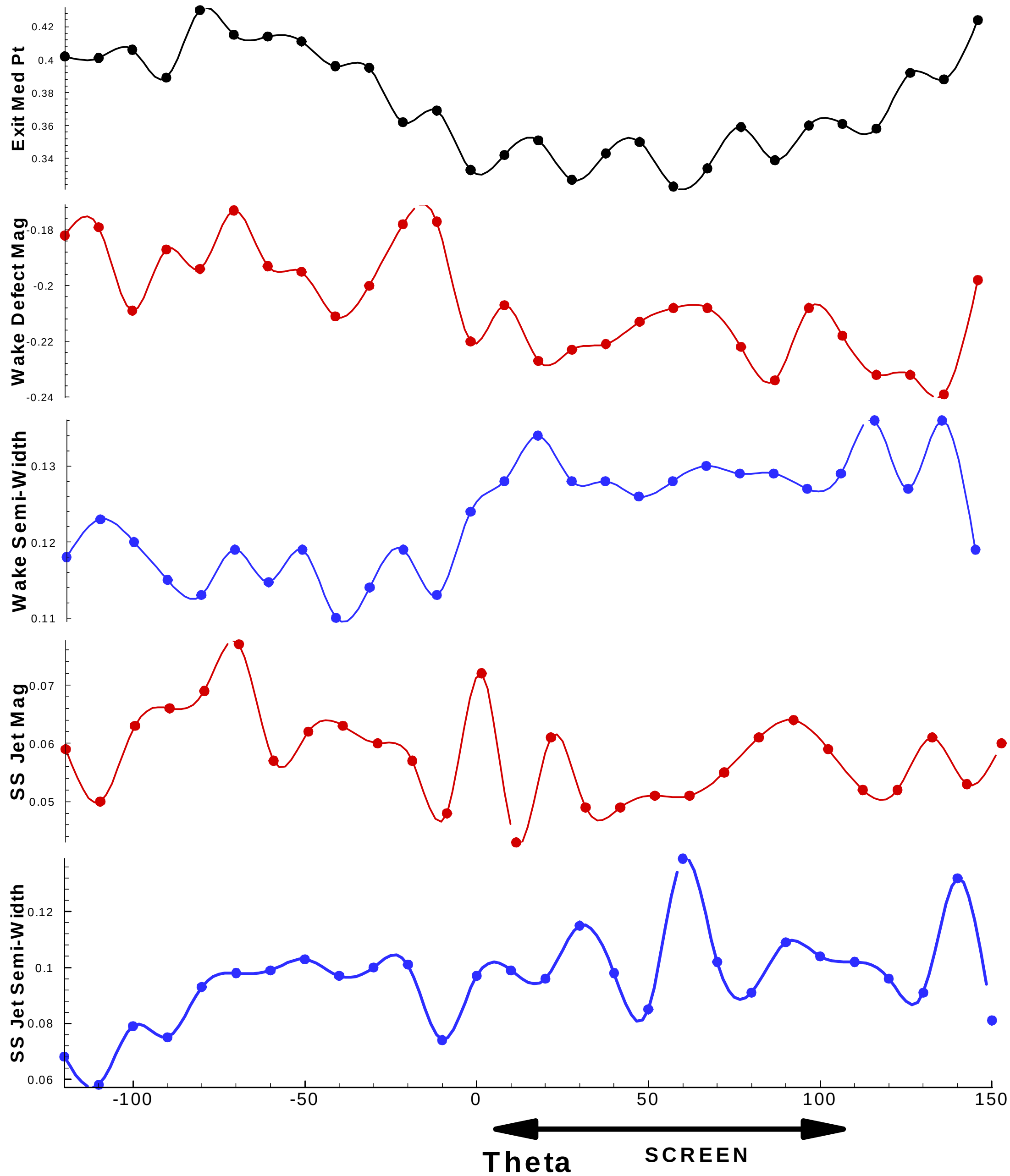

Figure A.6: Exit Flow Characteristics for Level 1, Operating Point A at 33% Span.

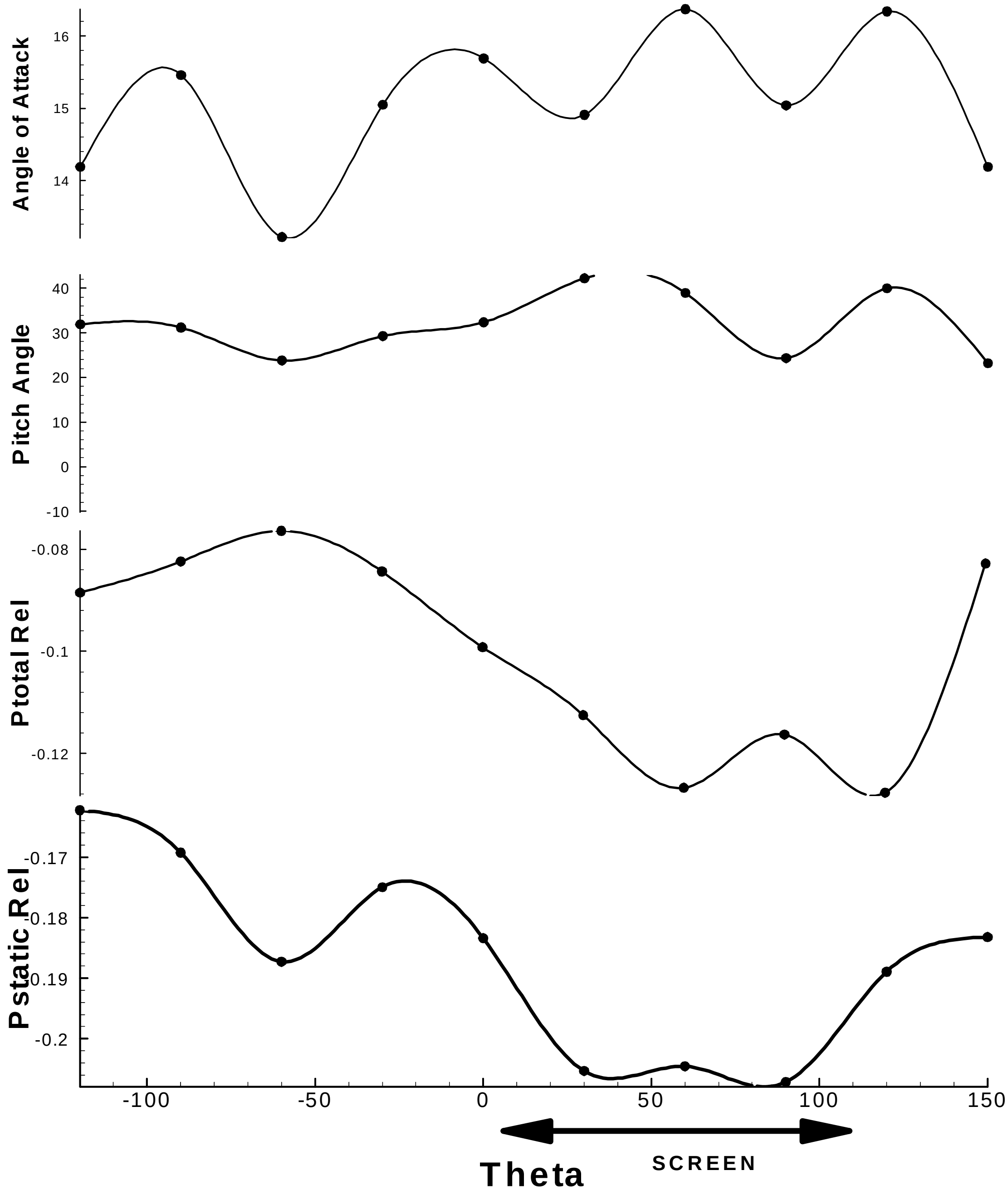

Figure A.7: Inlet Flow Characteristics for Level 1, Operating Point A at 67% Span.

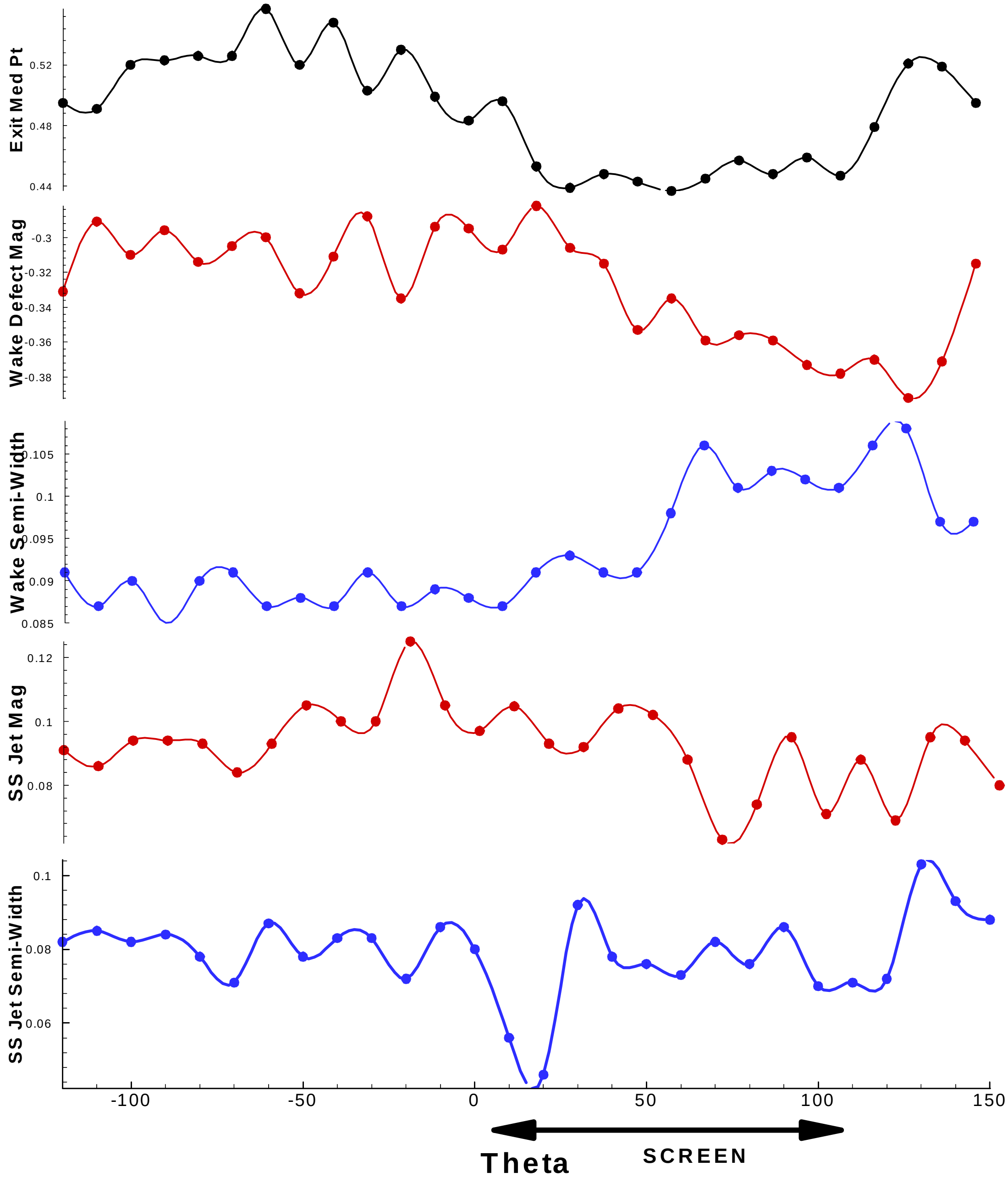

Figure A.8: Exit Flow Characteristics for Level 1, Operating Point A at 67% Span.

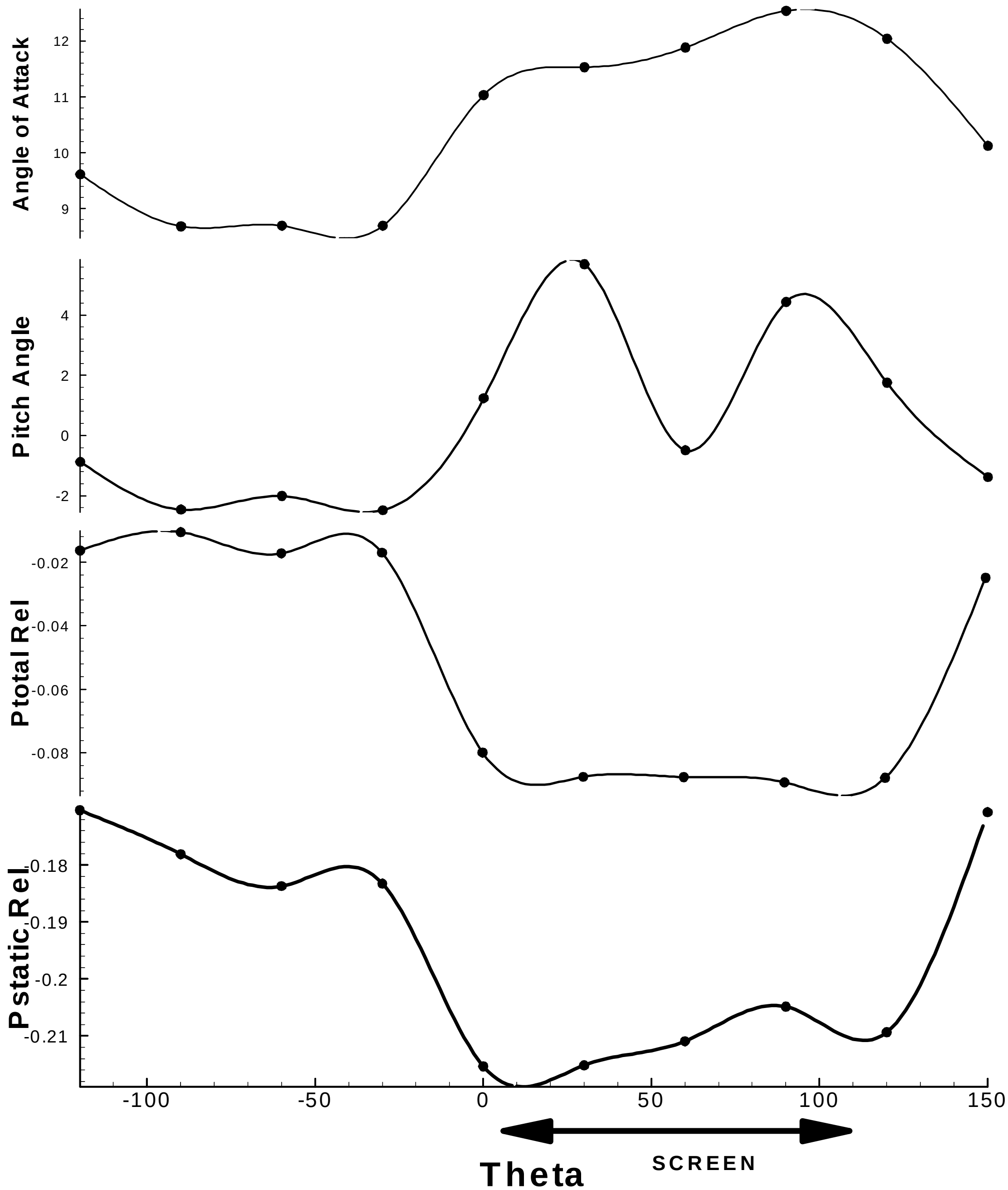

Figure A.9: Inlet Flow Characteristics for Level 1, Operating Point B at 50% Span.

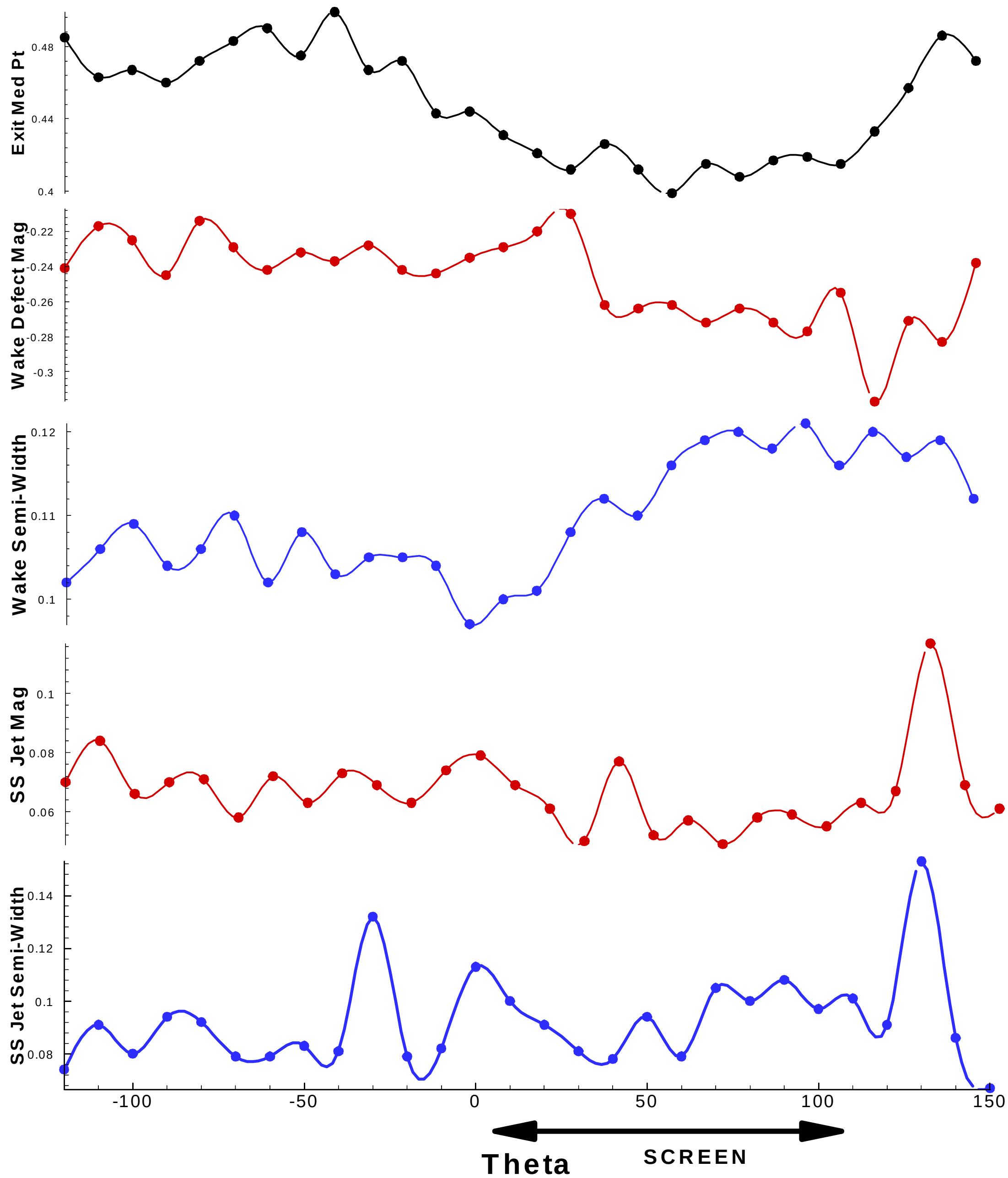

Figure A.10: Exit Flow Characteristics for Level 1, Operating Point B at 50% Span.

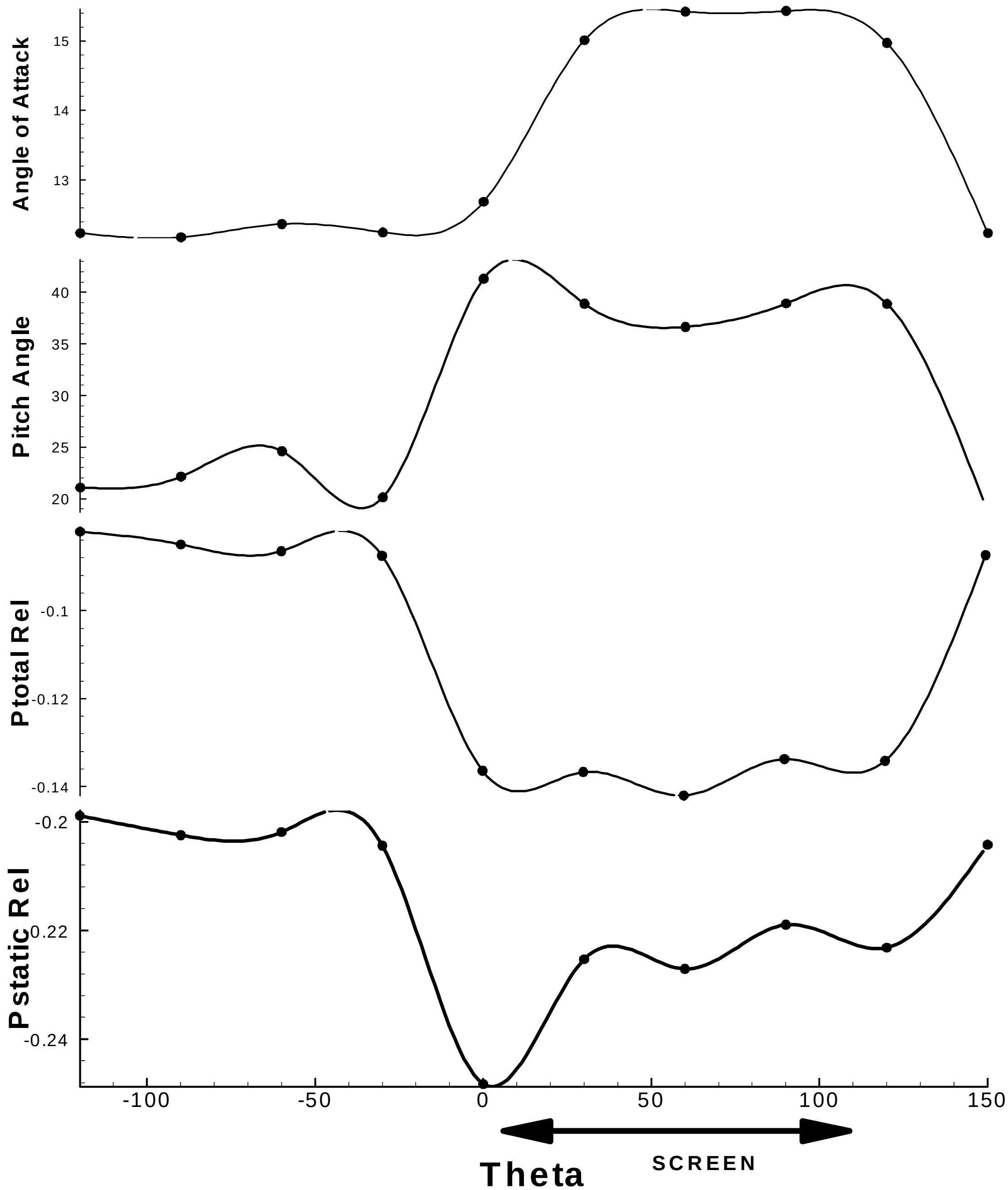

Figure A.11: Inlet Flow Characteristics for Level 1, Operating Point B at 33% Span.

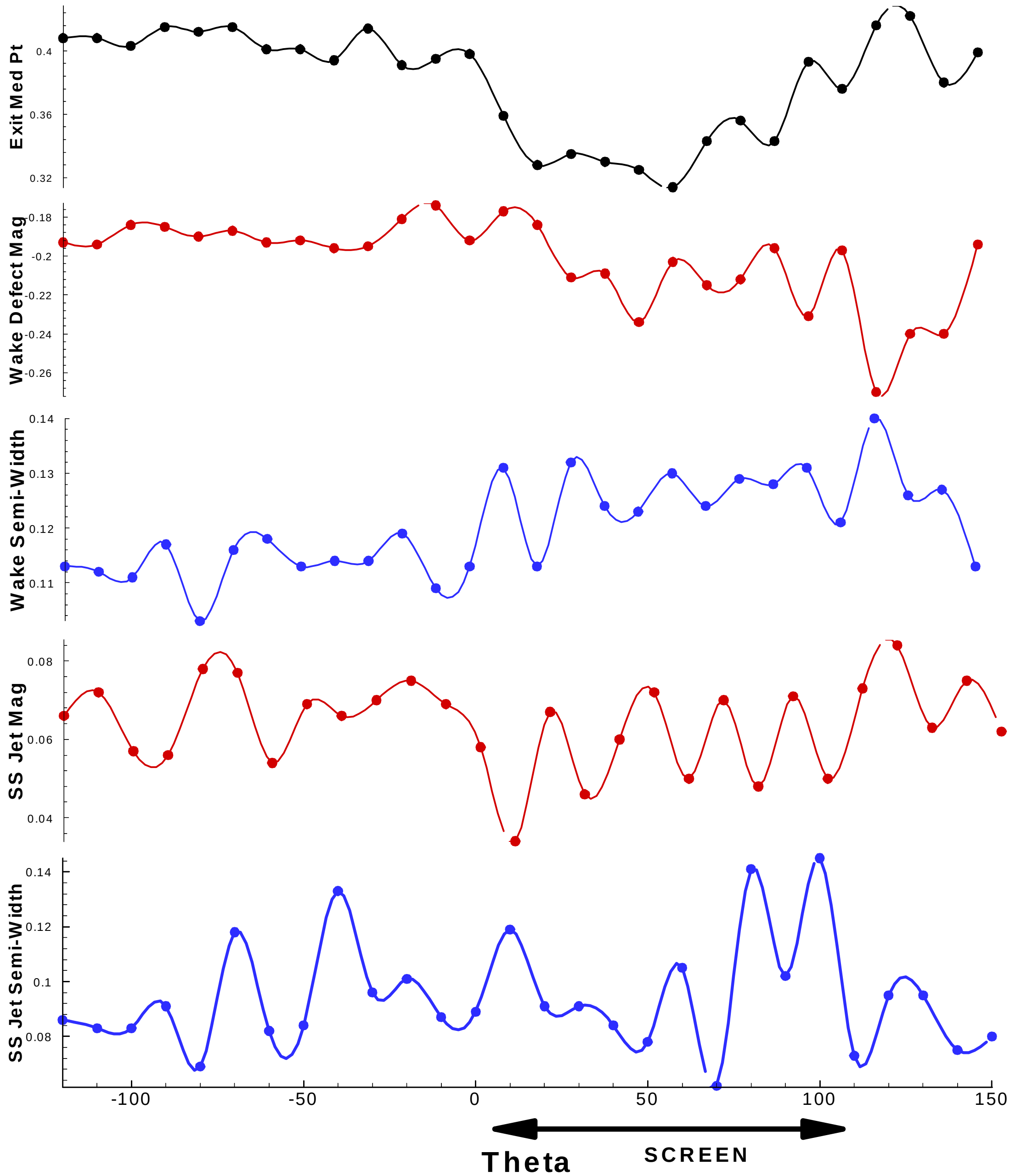

Figure A.12: Exit Flow Characteristics for Level 1, Operating Point B at 33% Span.

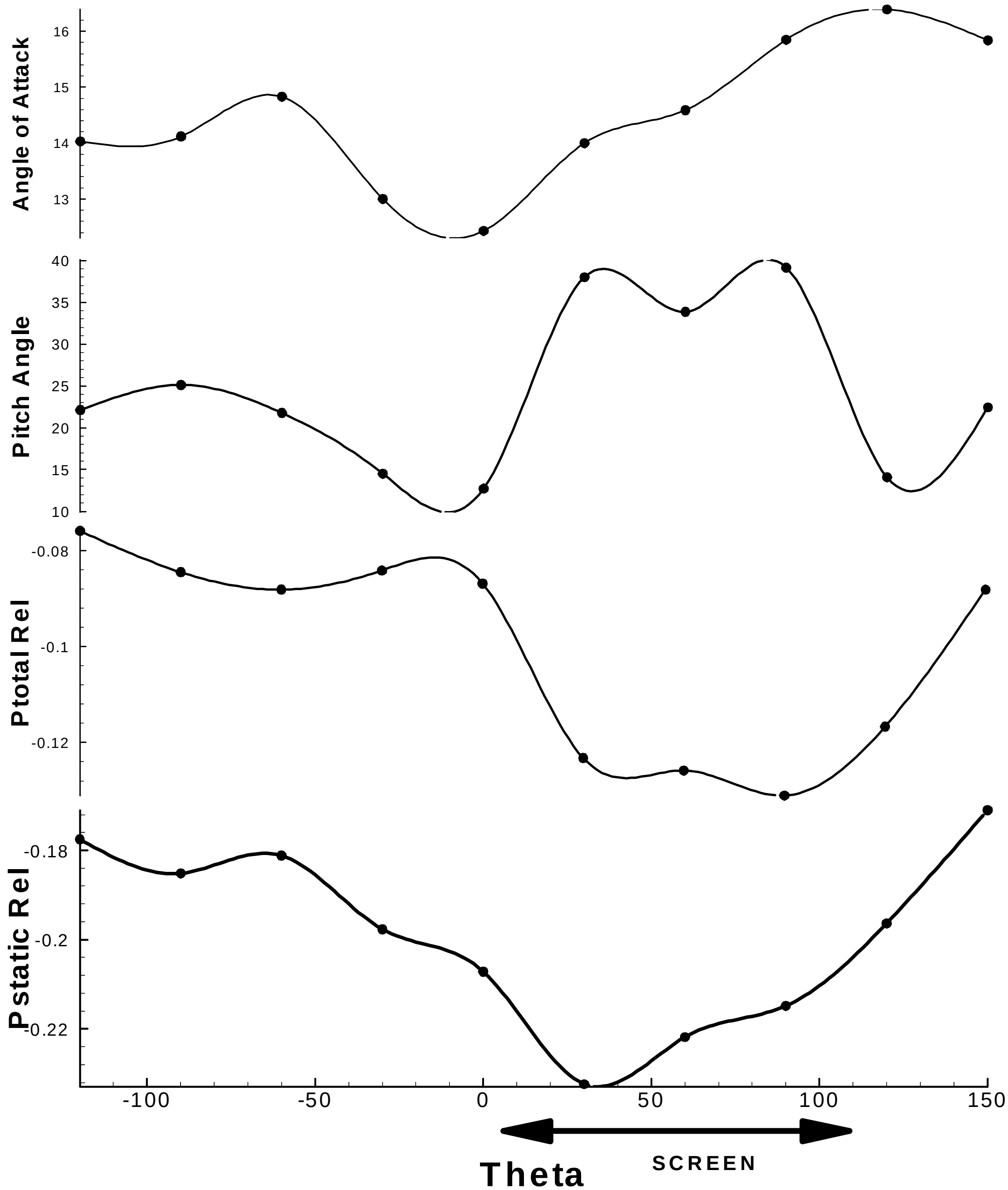

Figure A.13: Inlet Flow Characteristics for Level 1, Operating Point B at 67% Span.

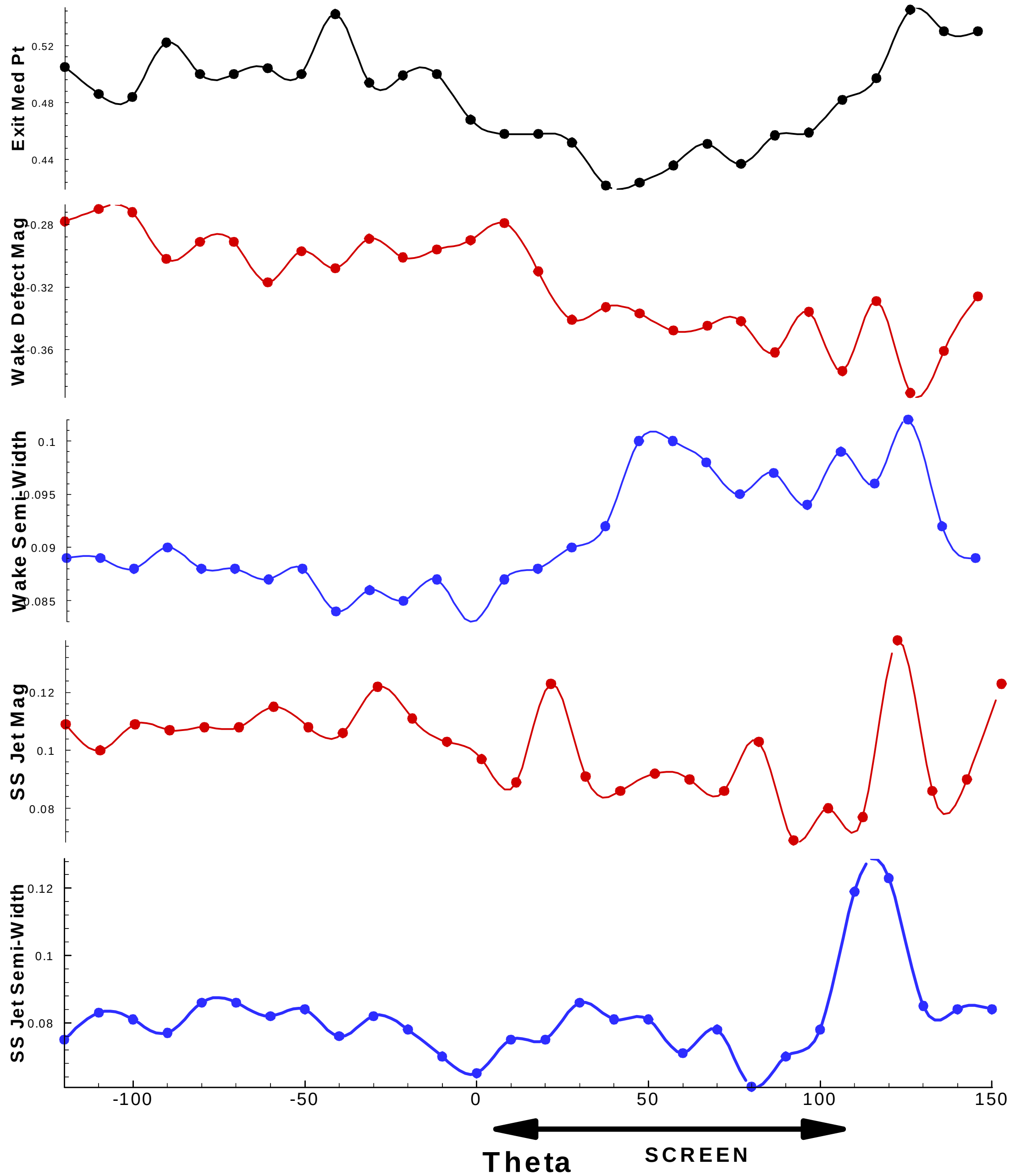

Figure A.14: Exit Flow Characteristics for Level 1, Operating Point B at 67% Span.

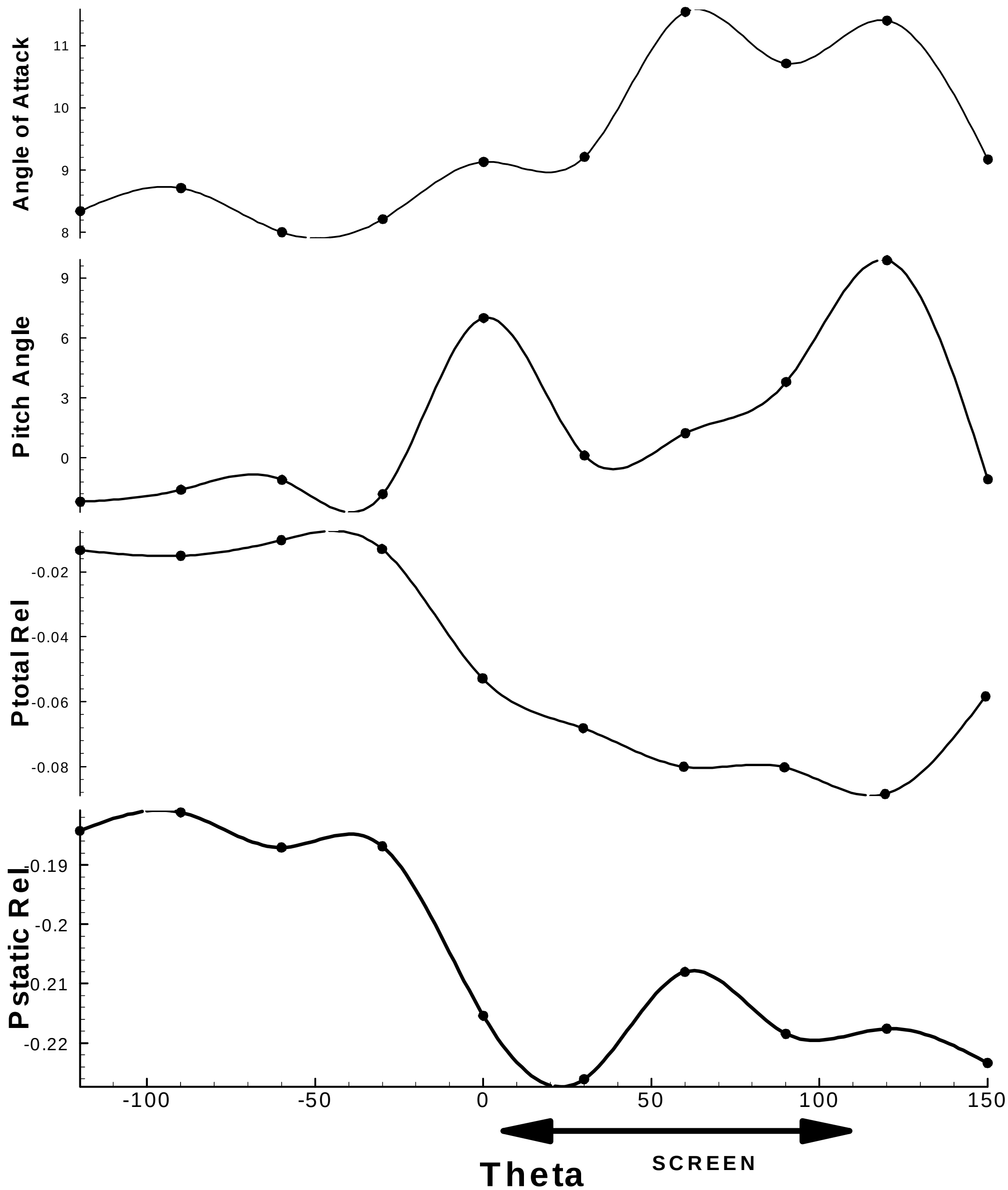

Figure A.15: Inlet Flow Characteristics for Level 1, Operating Point C at 50% Span.

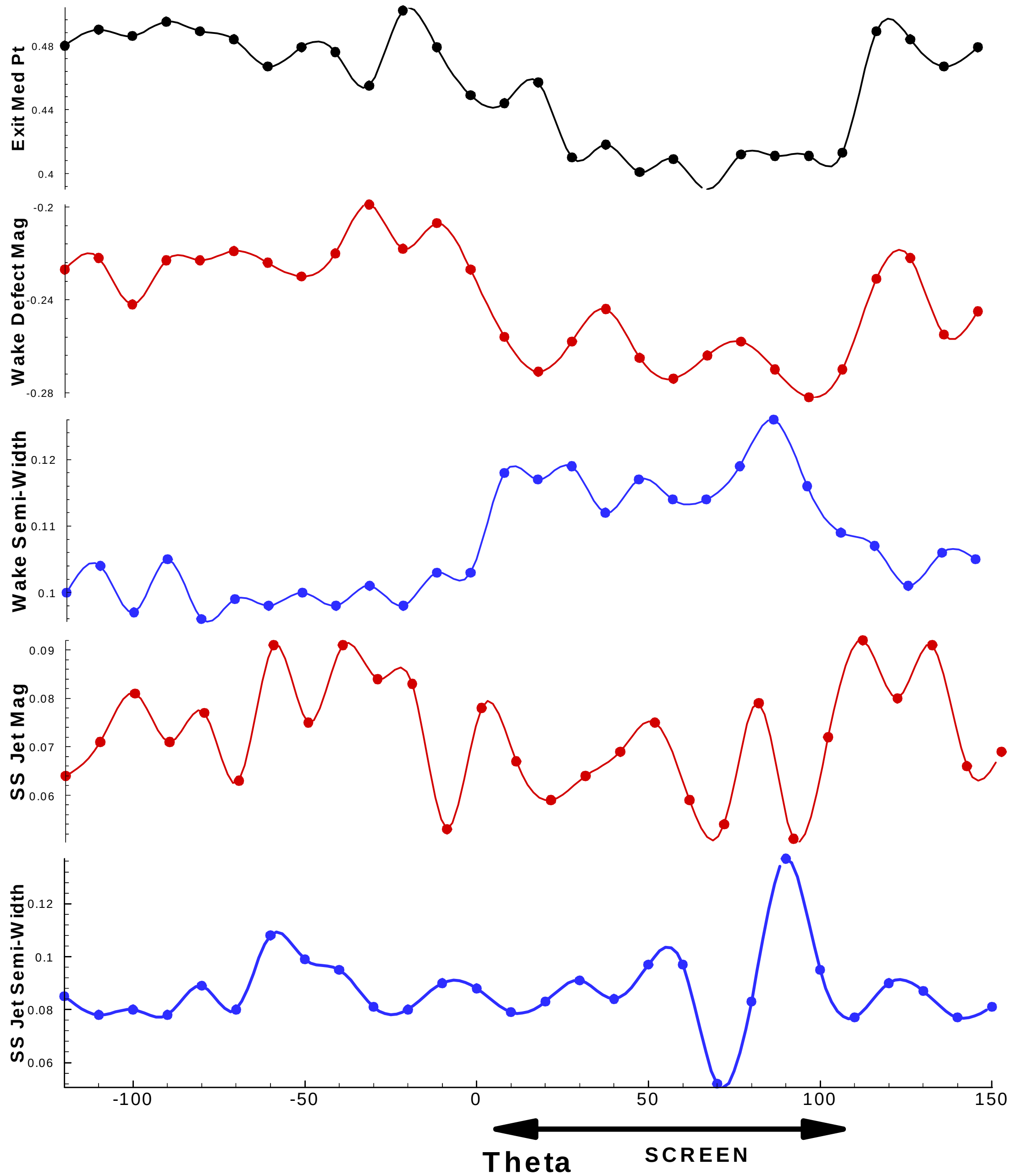

Figure A.16: Exit Flow Characteristics for Level 1, Operating Point C at 50% Span.

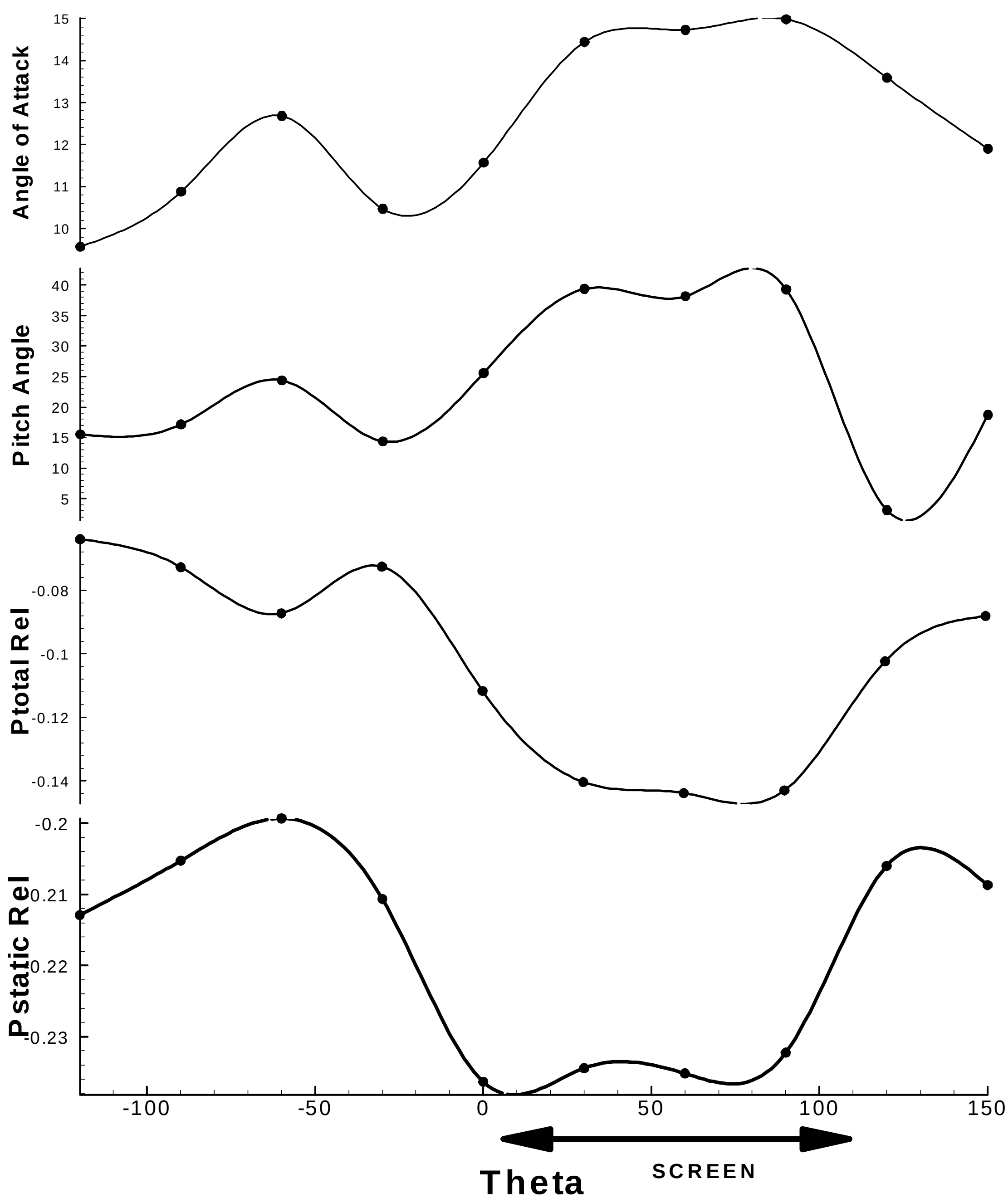

Figure A.17: Inlet Flow Characteristics for Level 1, Operating Point C at 33% Span.

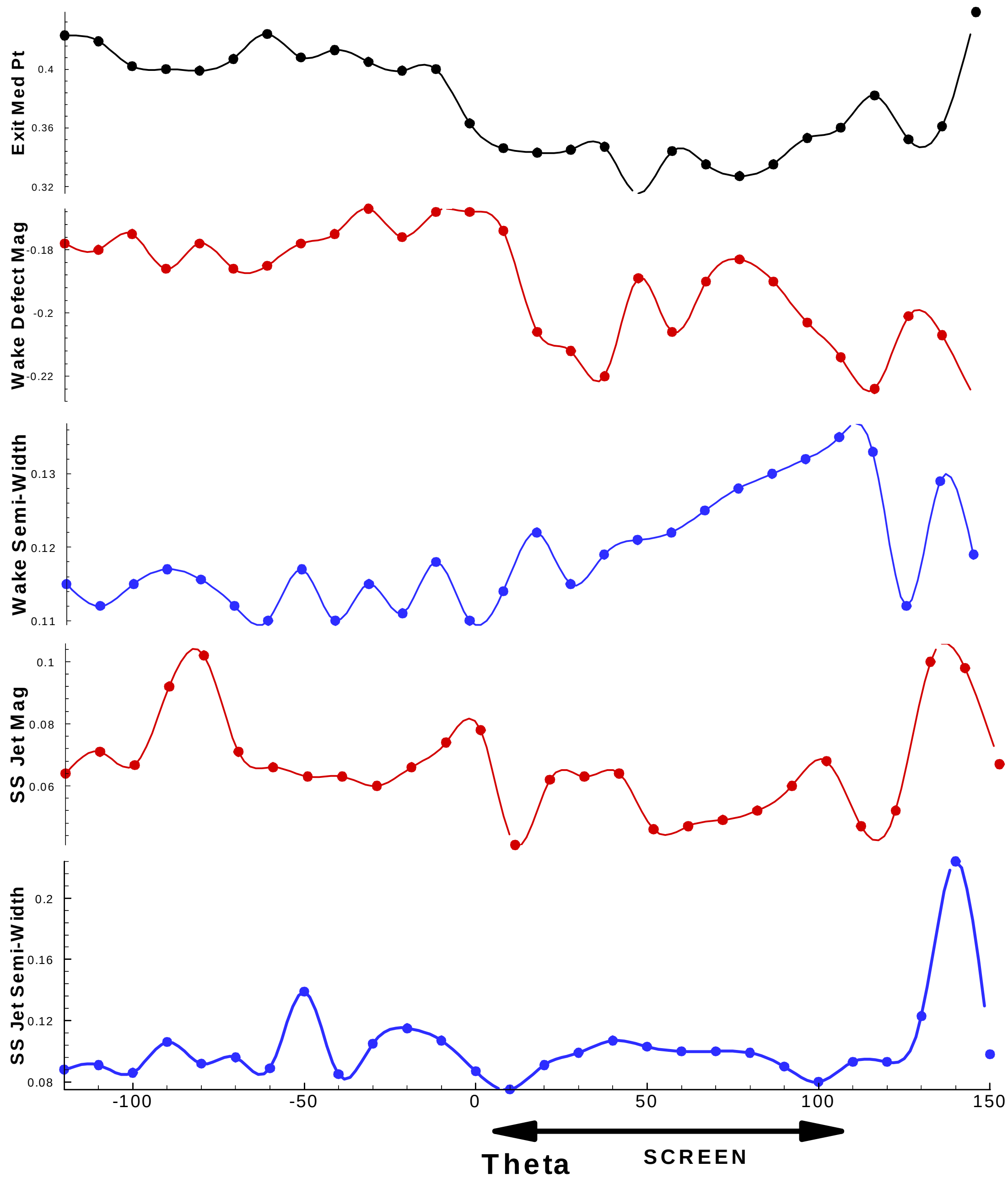

Figure A.18: Exit Flow Characteristics for Level 1, Operating Point C at 33% Span.

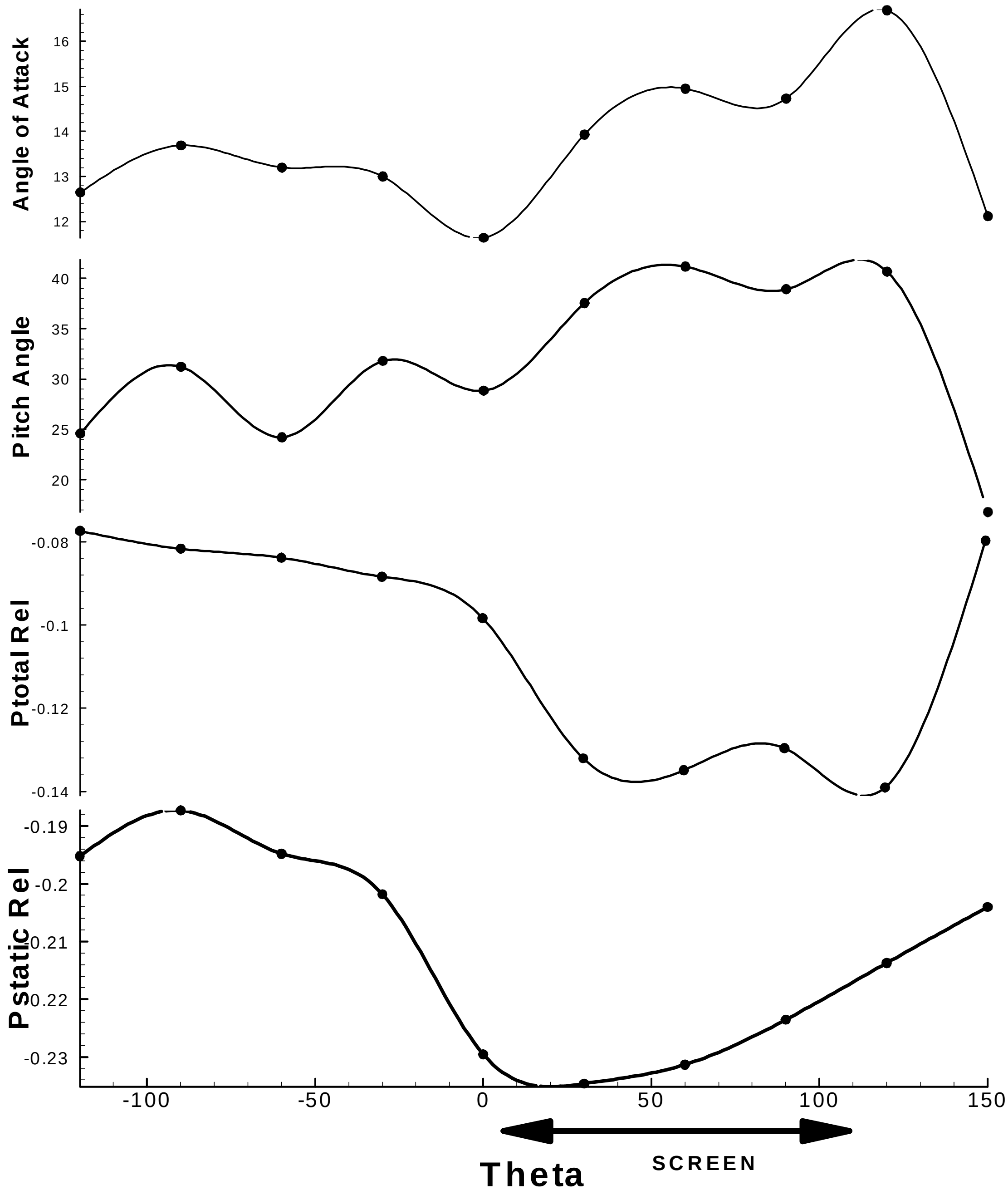

Figure A.19: Inlet Flow Characteristics for Level 1, Operating Point C at 67% Span.

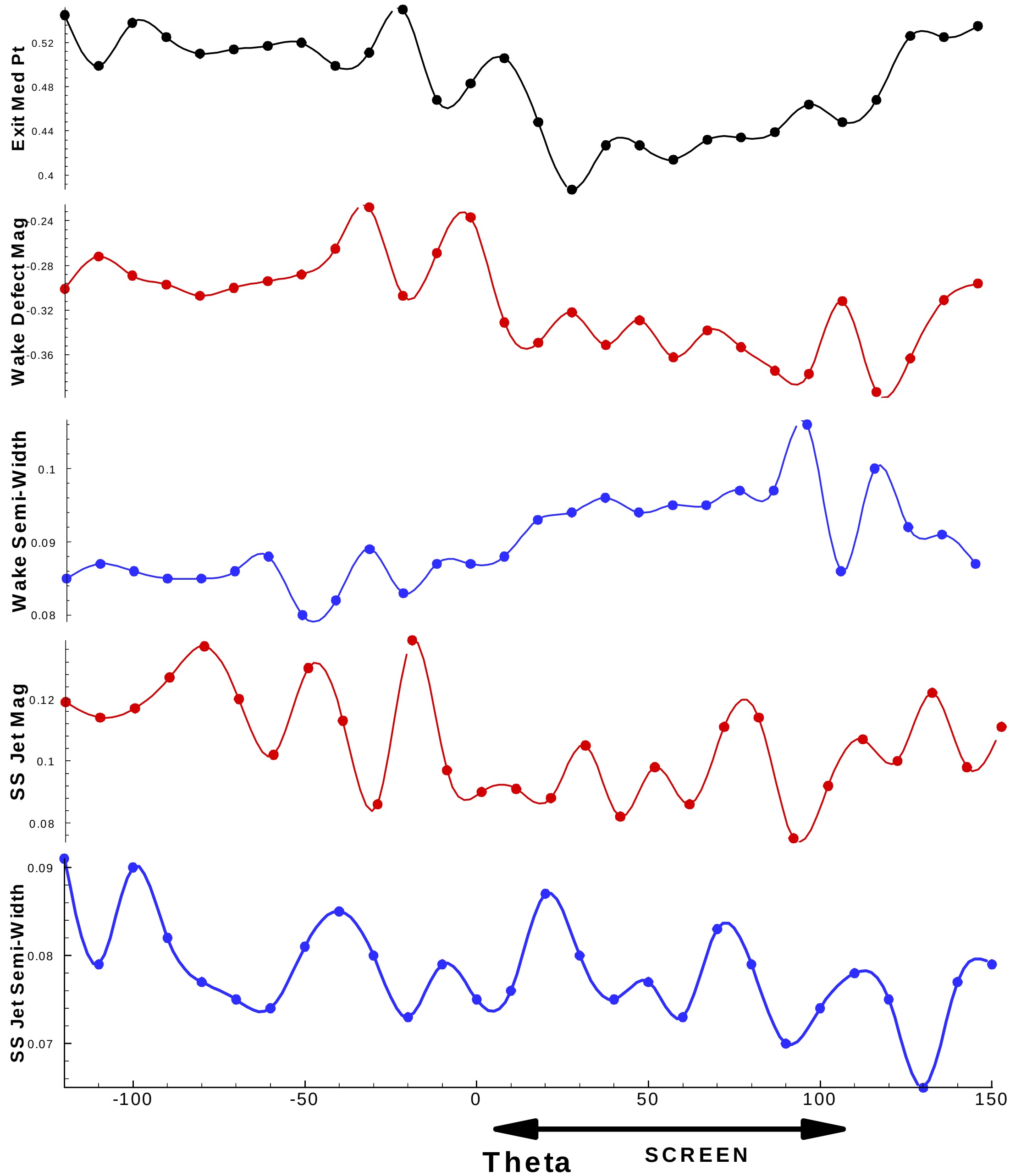

Figure A.20: Exit Flow Characteristics for Level 1, Operating Point C at 67% Span.

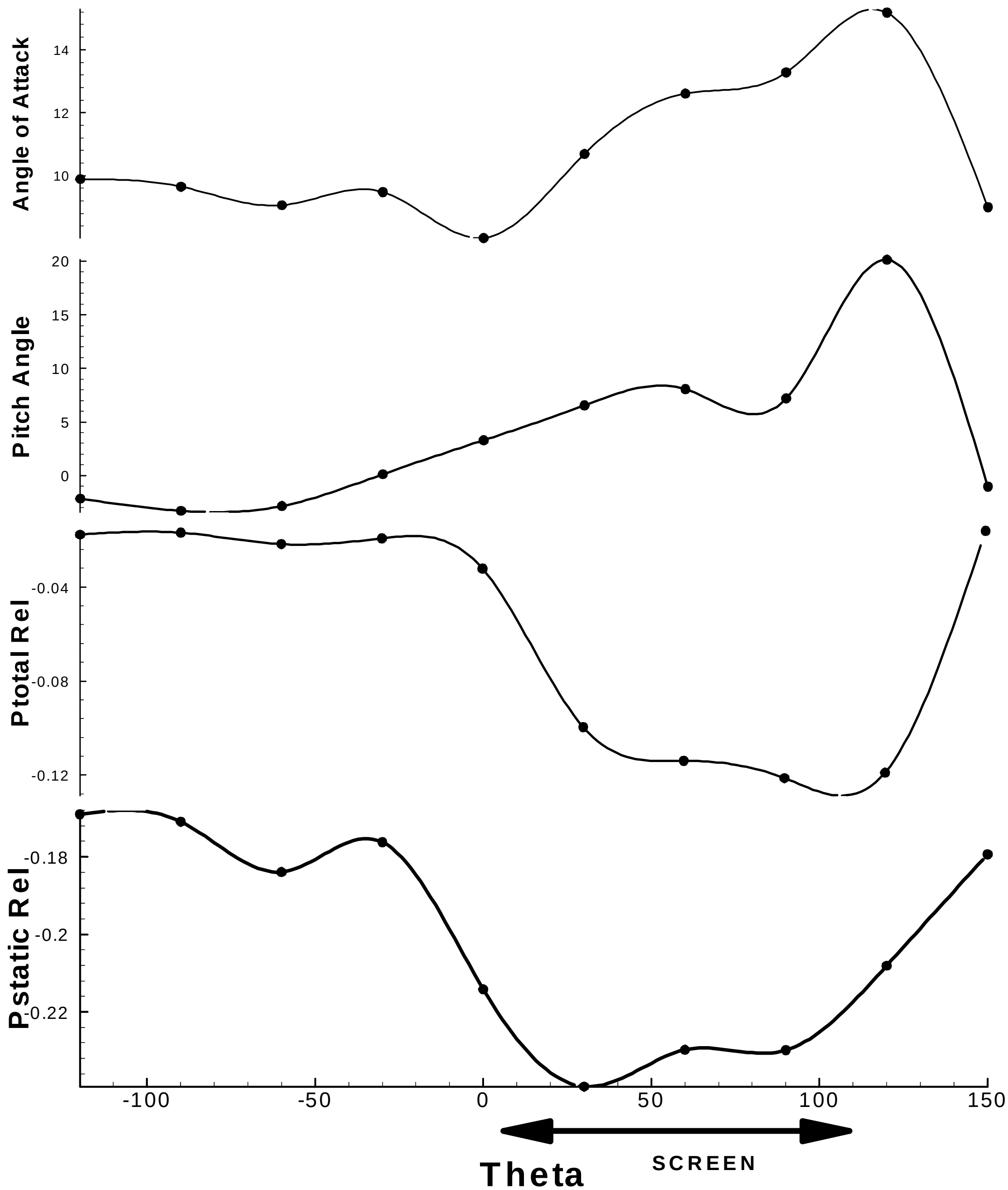

Figure A.21: Inlet Flow Characteristics for Level 2, Operating Point A at 50% Span.

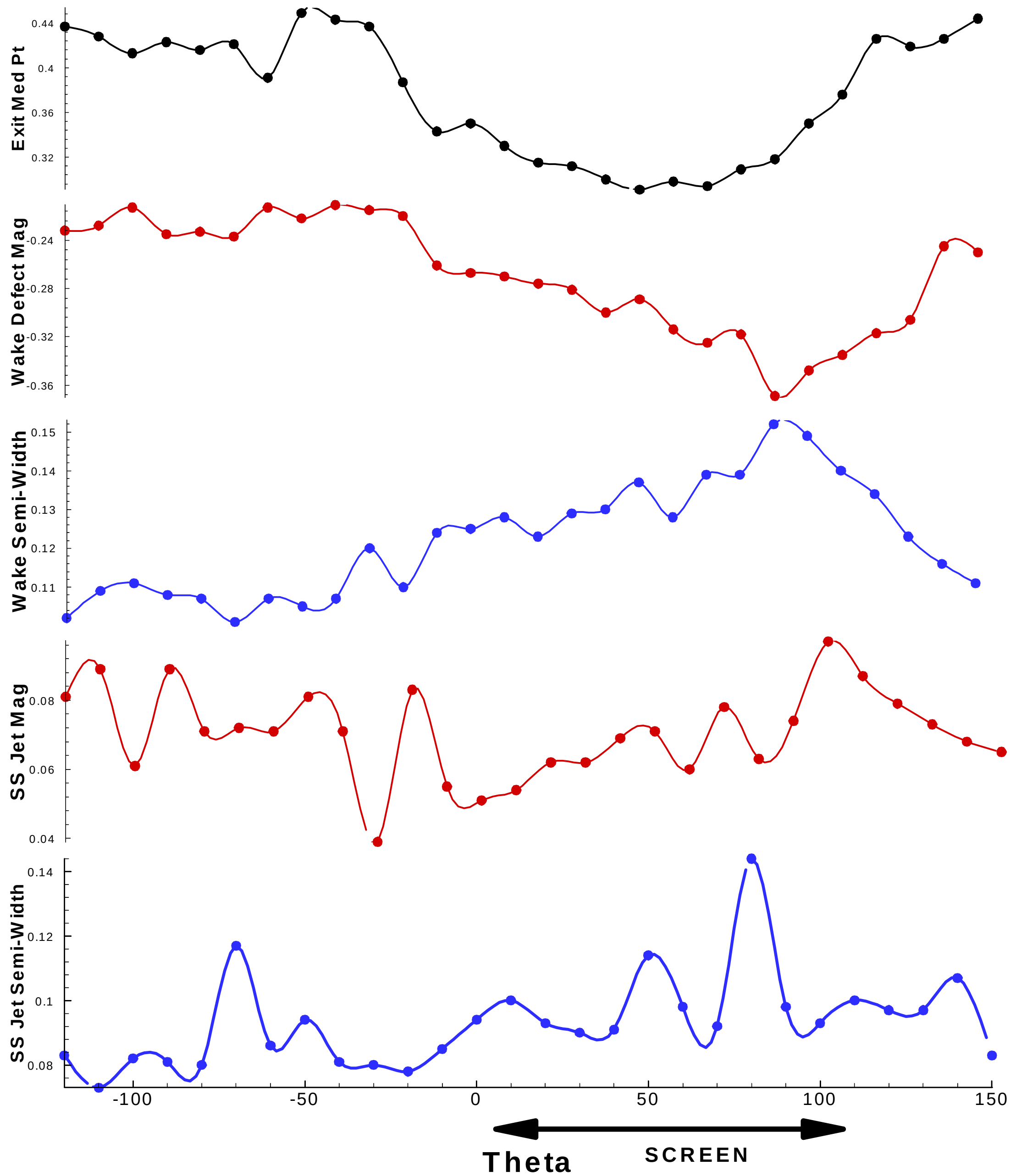

Figure A.22: Exit Flow Characteristics for Level 2, Operating Point A at 50% Span.

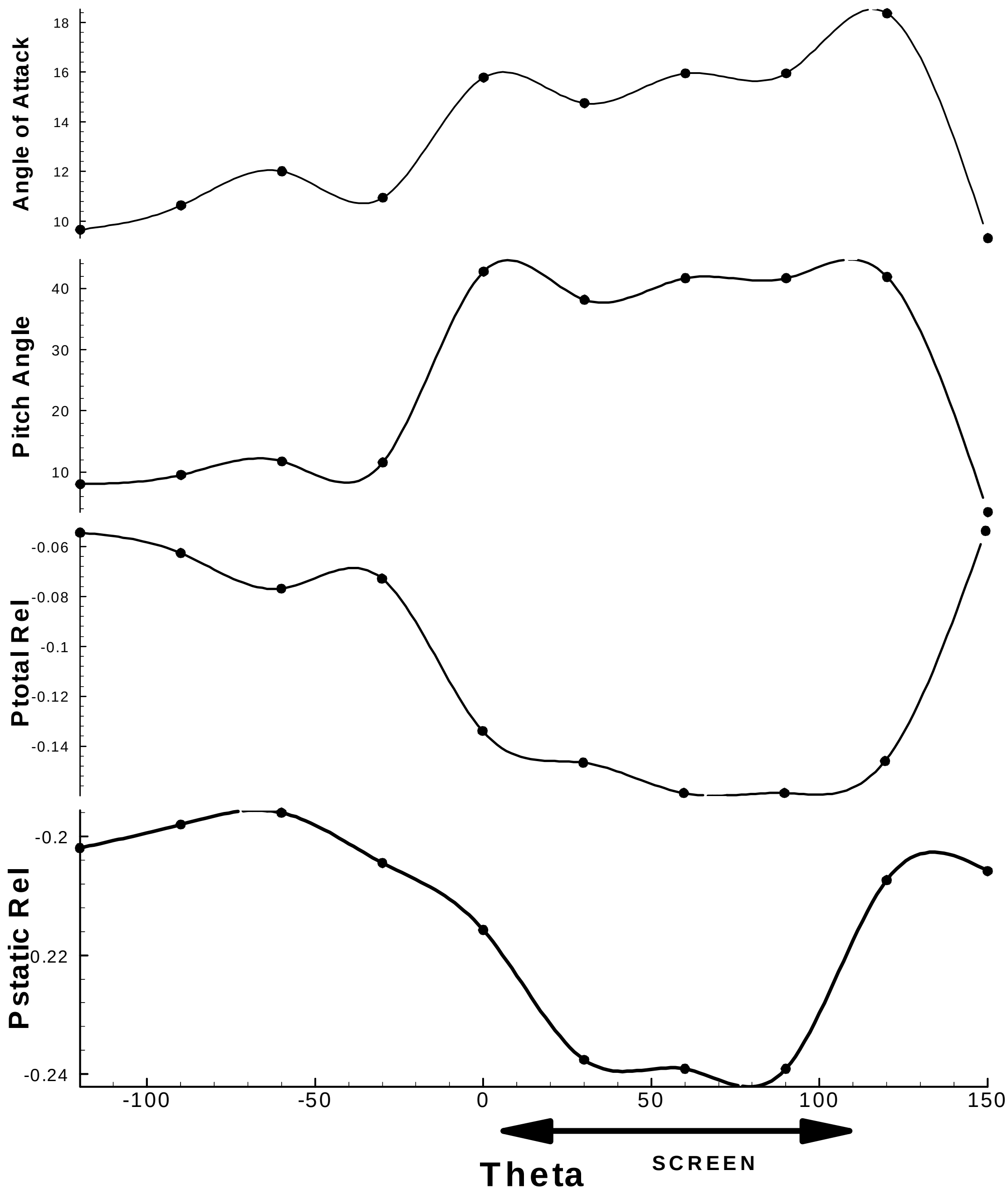

Figure A.23: Inlet Flow Characteristics for Level 2, Operating Point A at 33% Span.

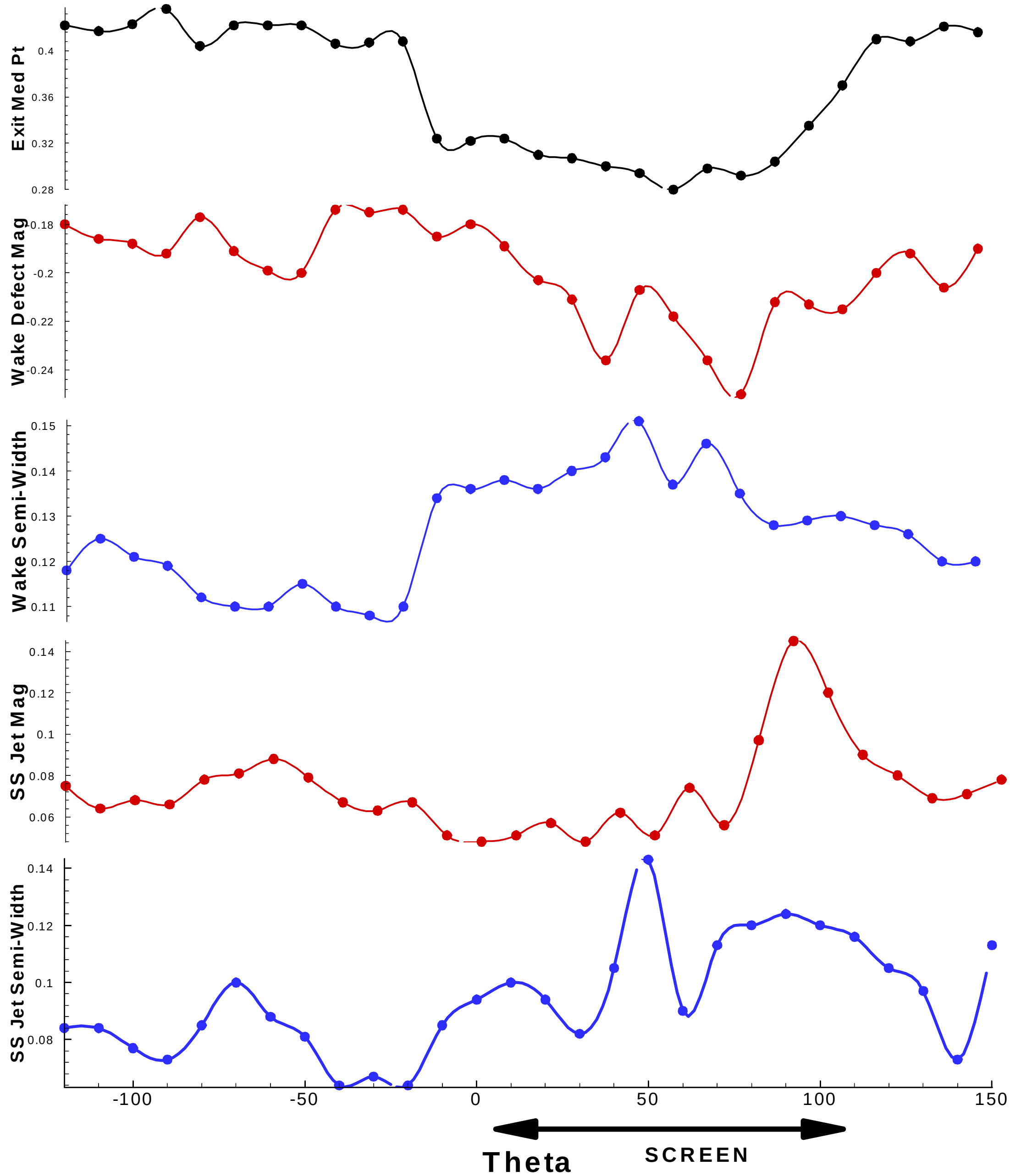

Figure A.24: Exit Flow Characteristics for Level 2, Operating Point A at 33% Span.

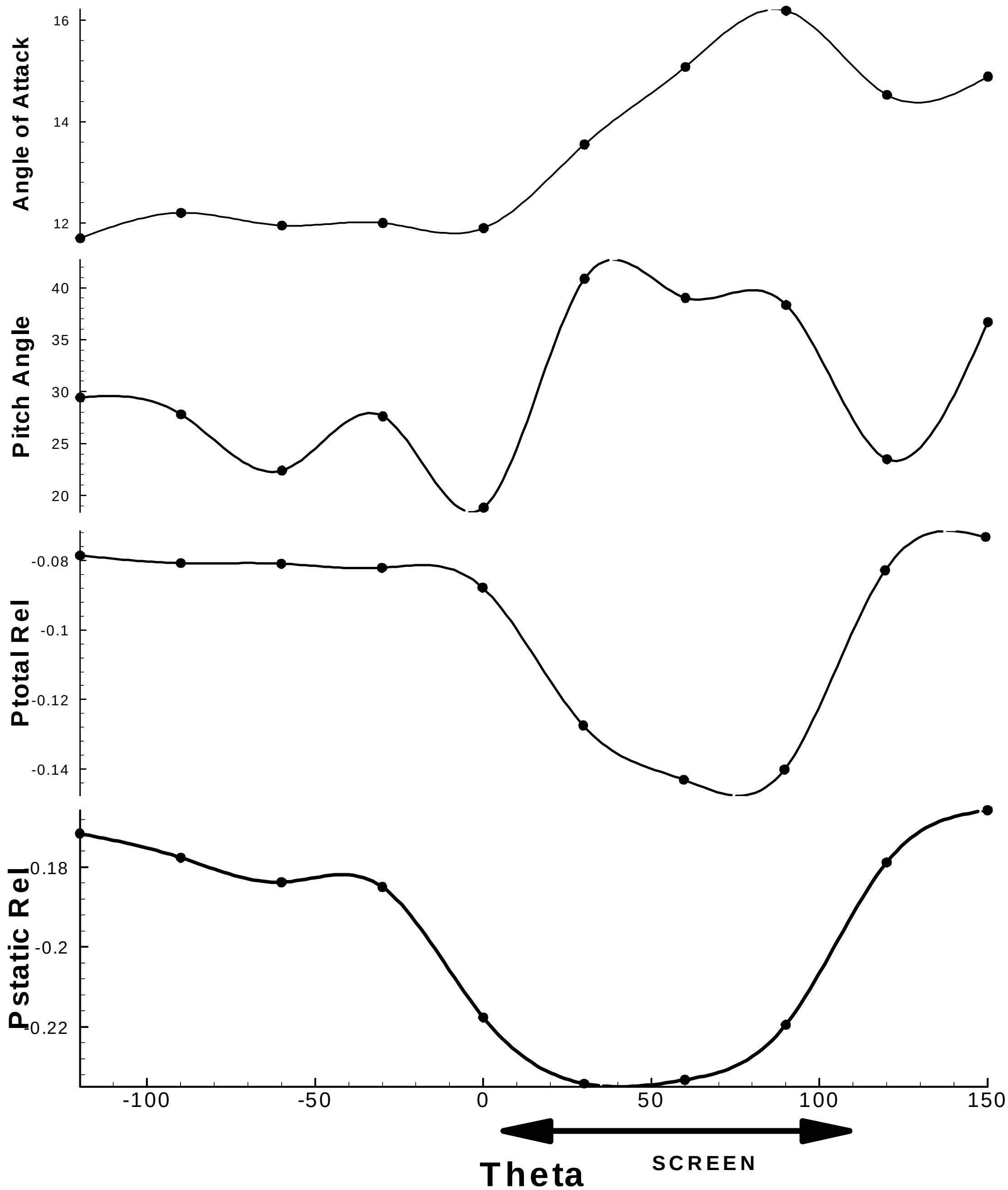

Figure A.25: Inlet Flow Characteristics for Level 2, Operating Point A at 67% Span.

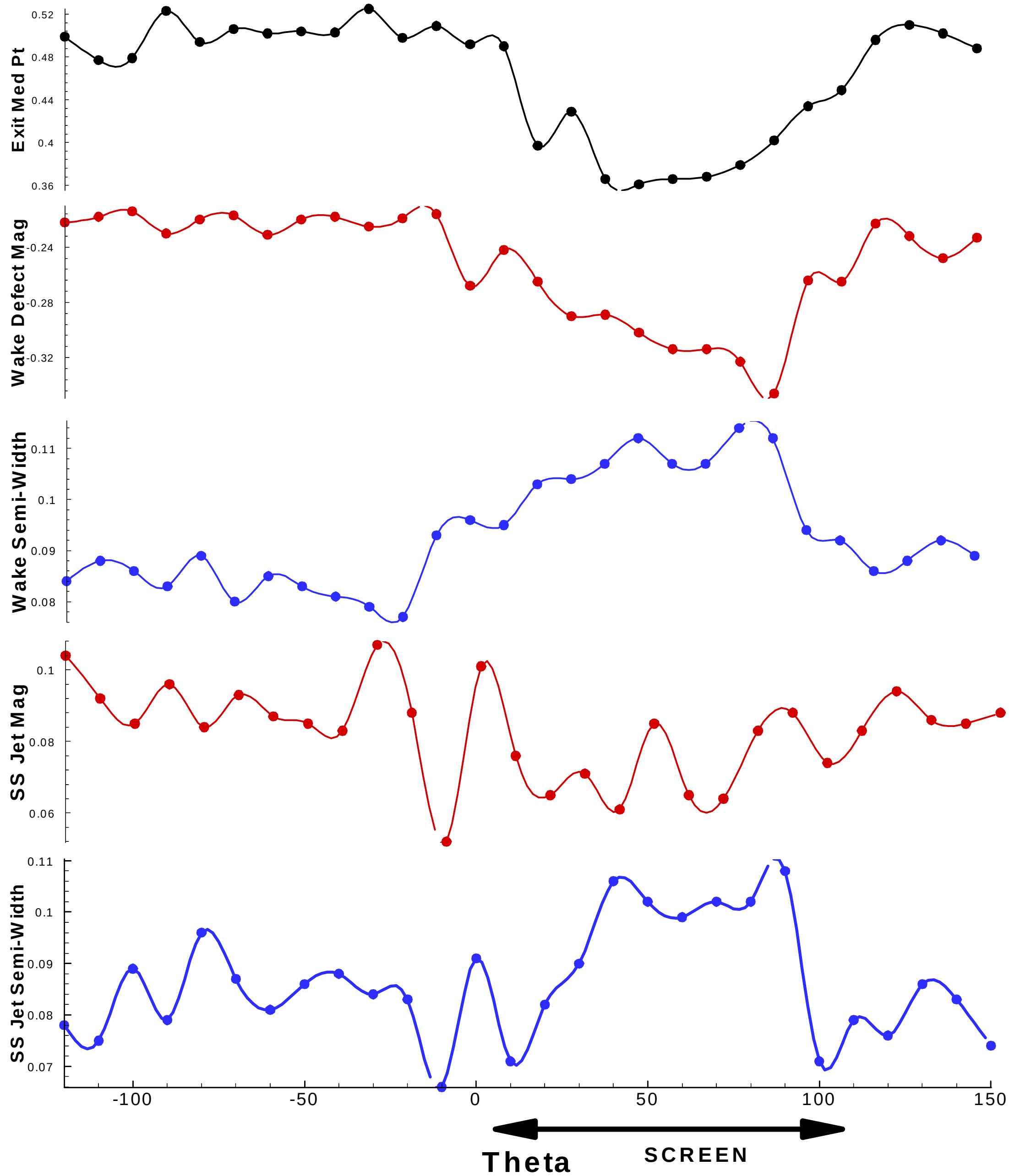

Figure A.26: Exit Flow Characteristics for Level 2, Operating Point A at 67% Span.

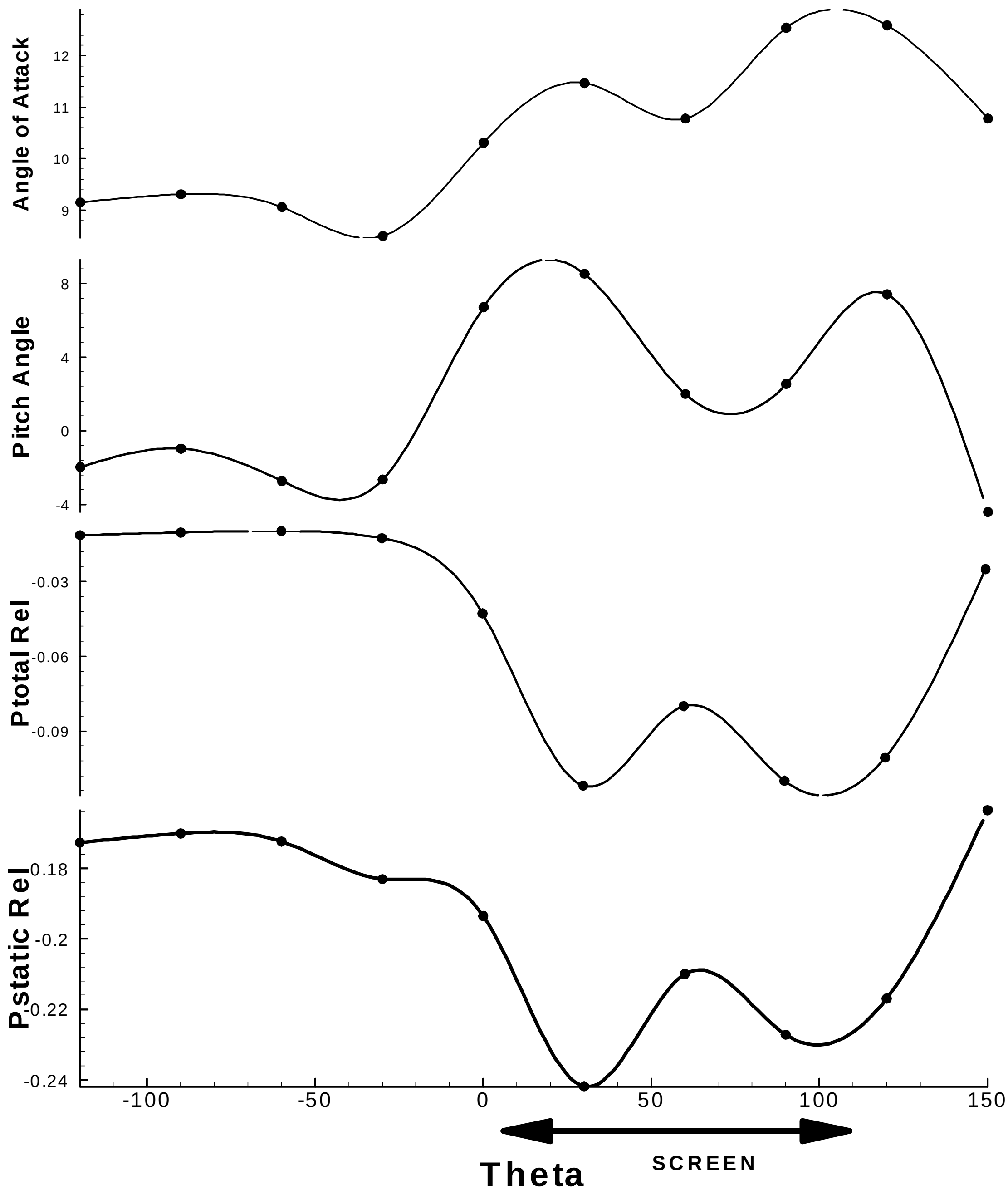

Figure A.27: Inlet Flow Characteristics for Level 2, Operating Point B at 50% Span.

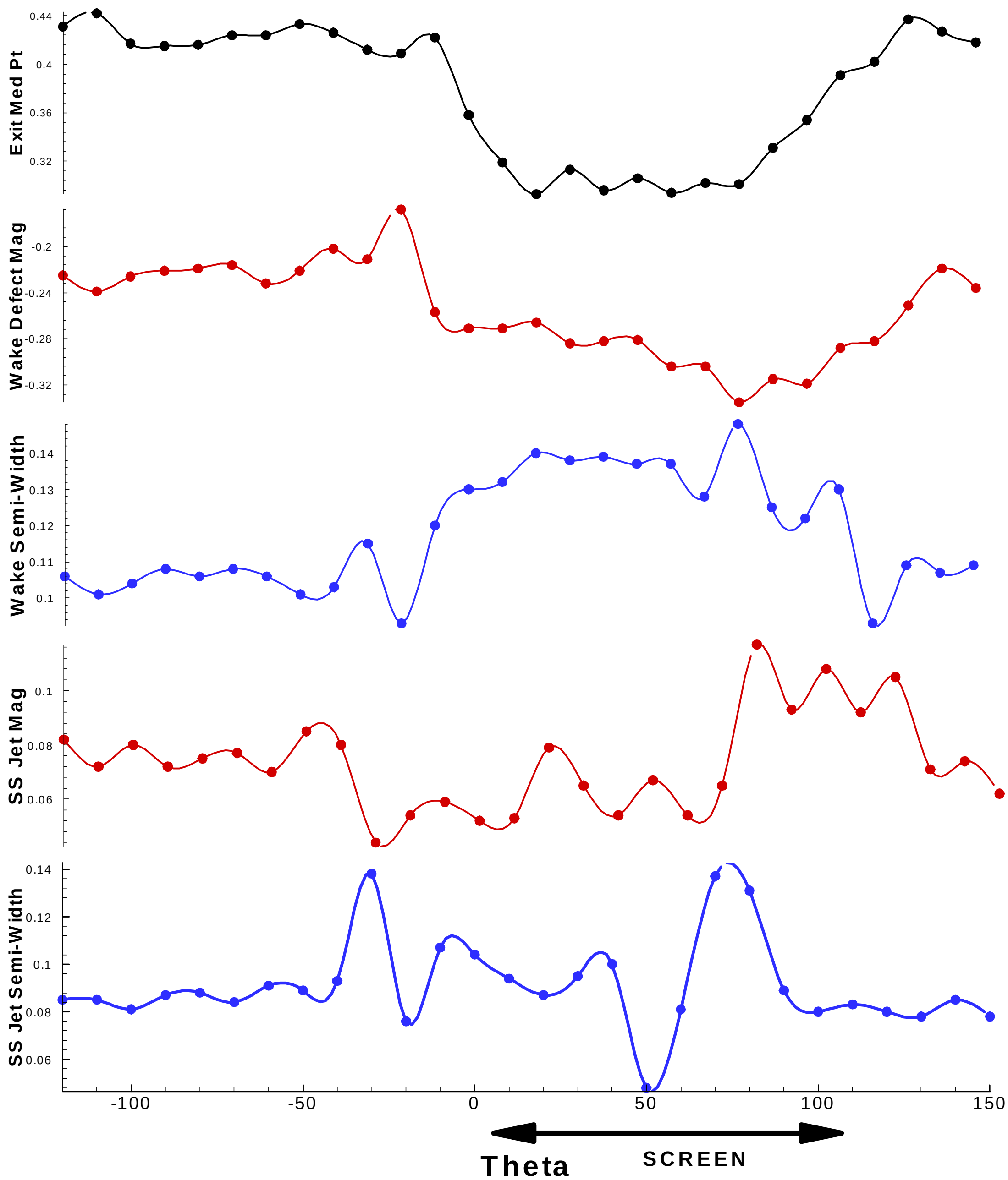

Figure A.28: Exit Flow Characteristics for Level 2, Operating Point B at 50% Span.

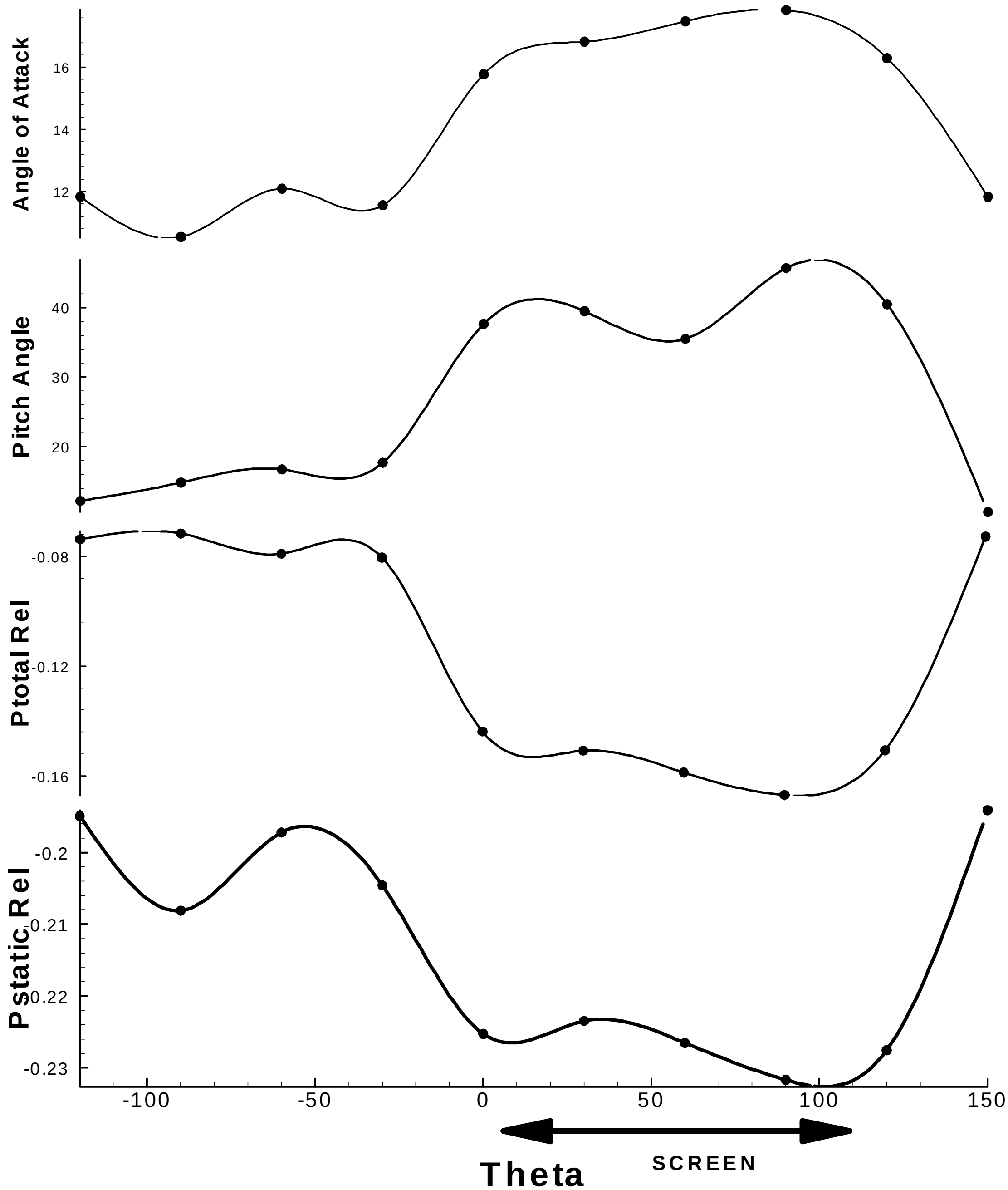

Figure A.29: Inlet Flow Characteristics for Level 2, Operating Point B at 33% Span.

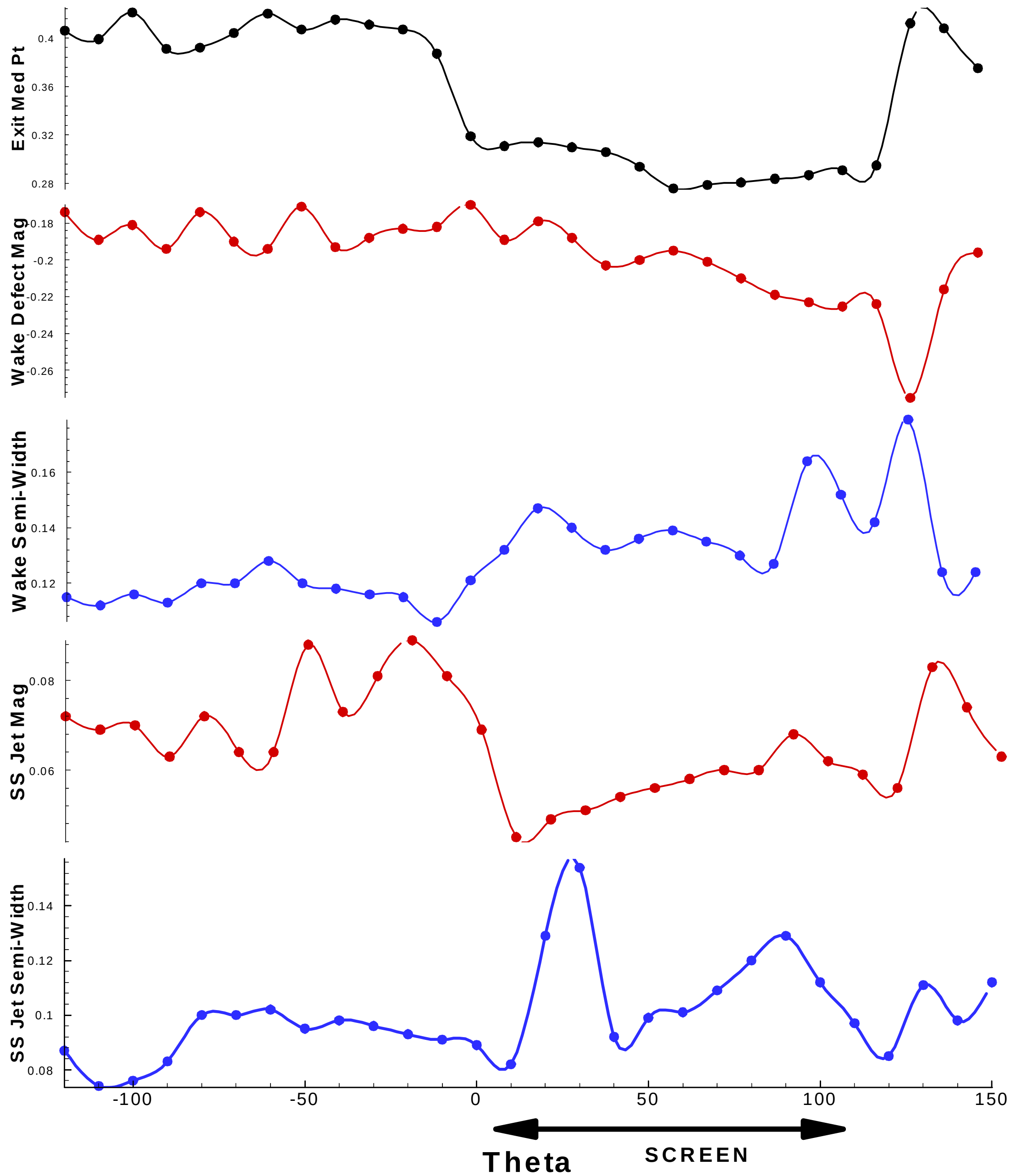

Figure A.30: Exit Flow Characteristics for Level 2, Operating Point B at 33% Span.

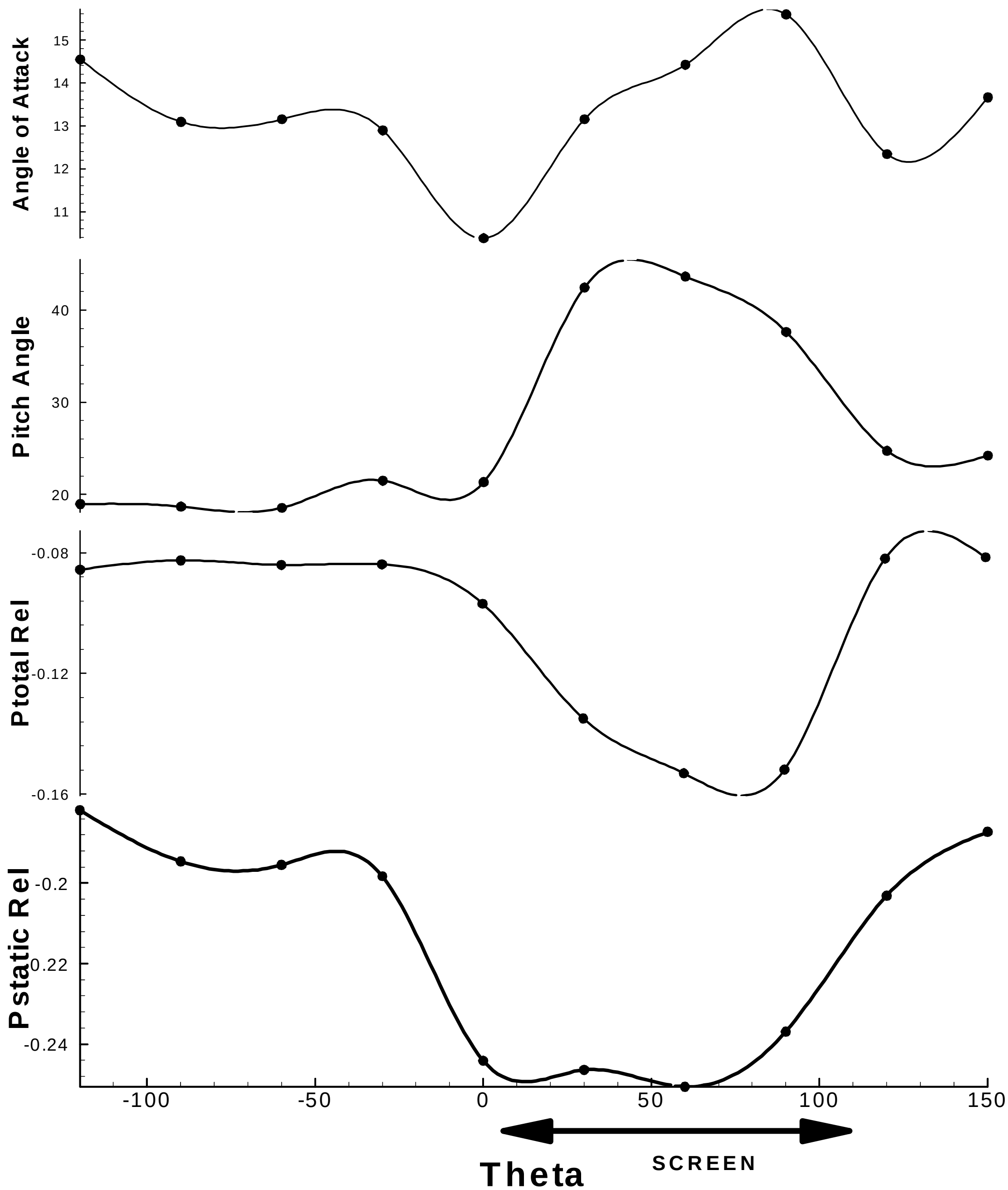

Figure A.31: Inlet Flow Characteristics for Level 2, Operating Point B at 67% Span.

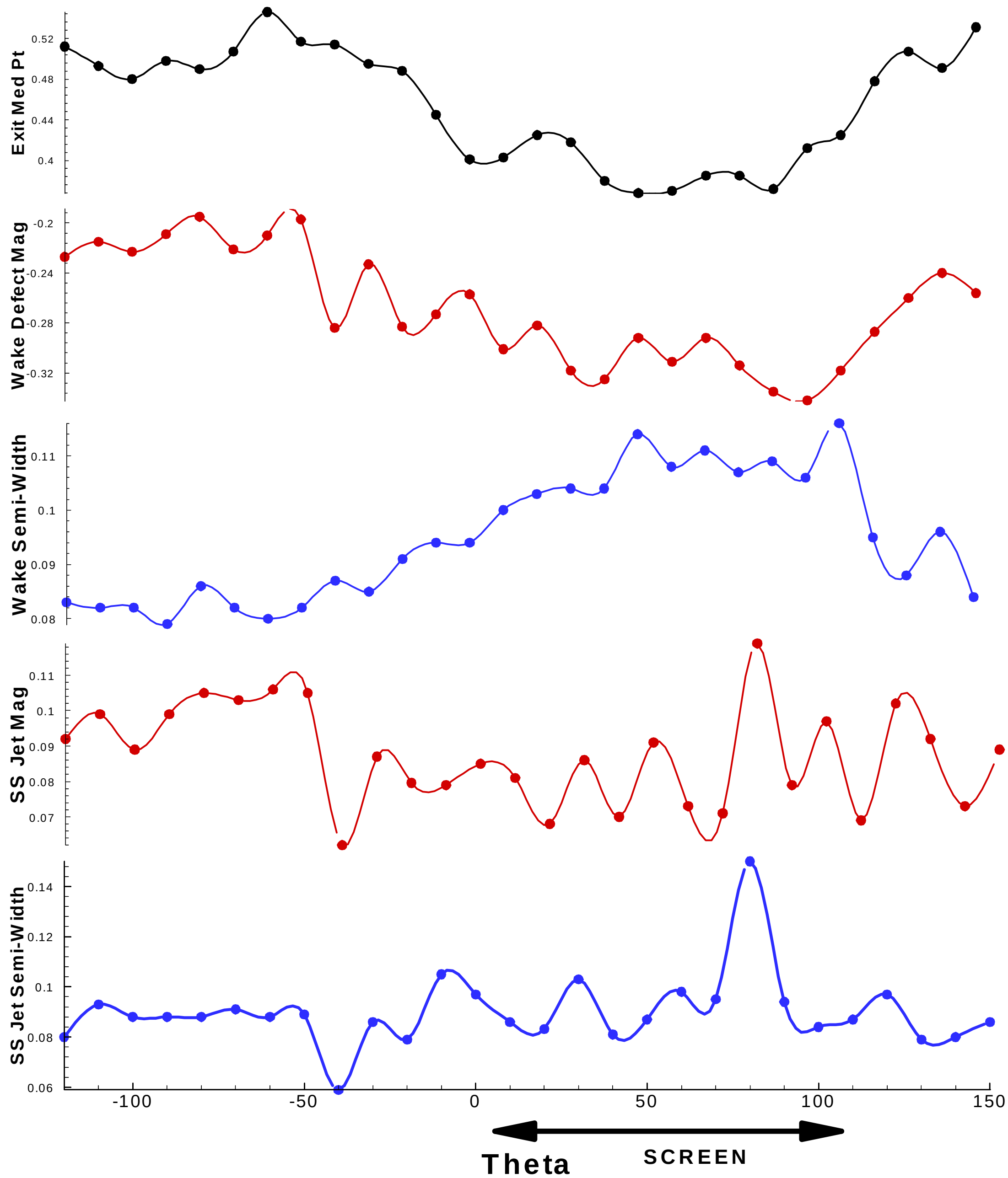

Figure A.32: Exit Flow Characteristics for Level 2, Operating Point B at 67% Span.

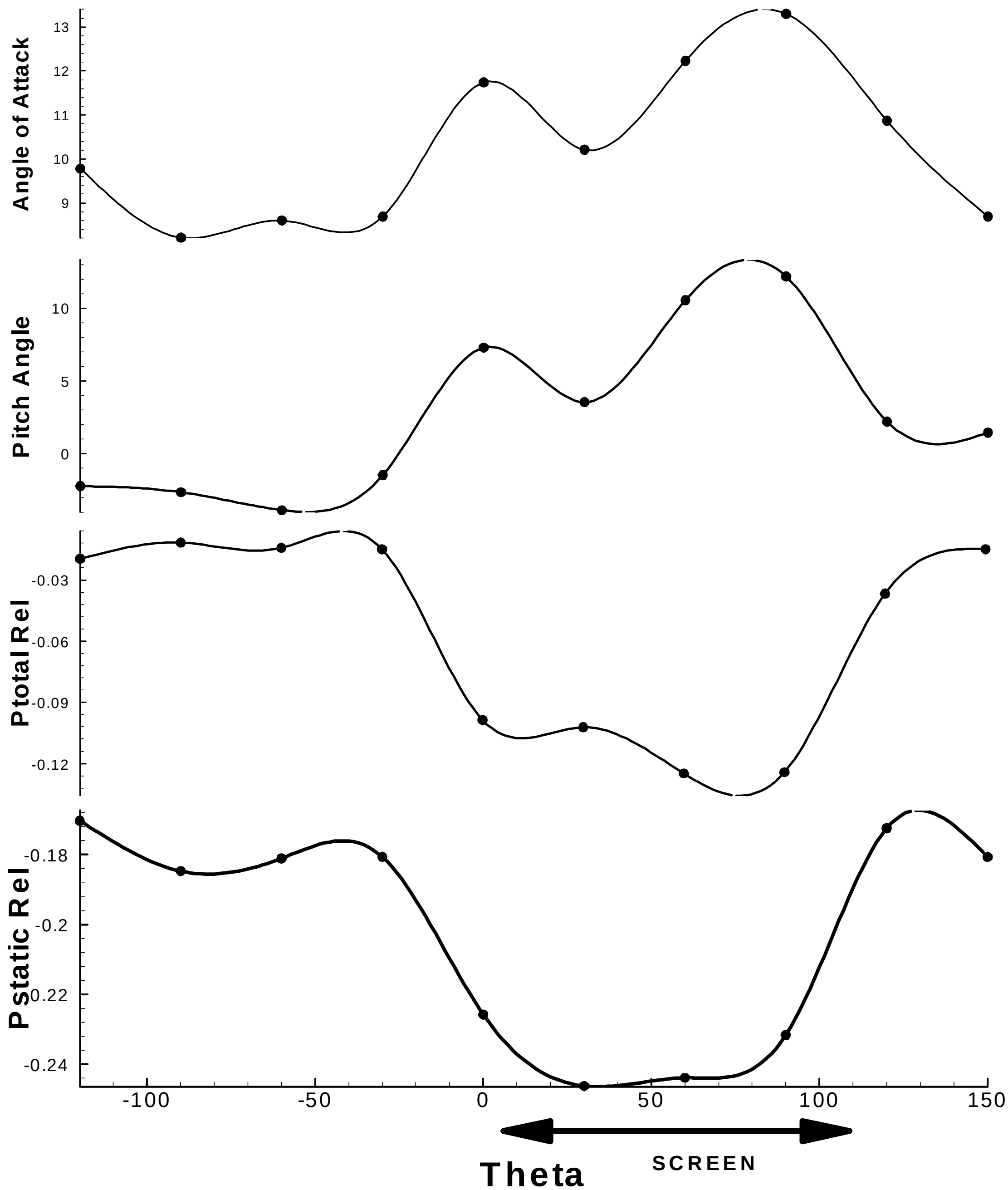

Figure A.33: Inlet Flow Characteristics for Level 2, Operating Point C at 50% Span.

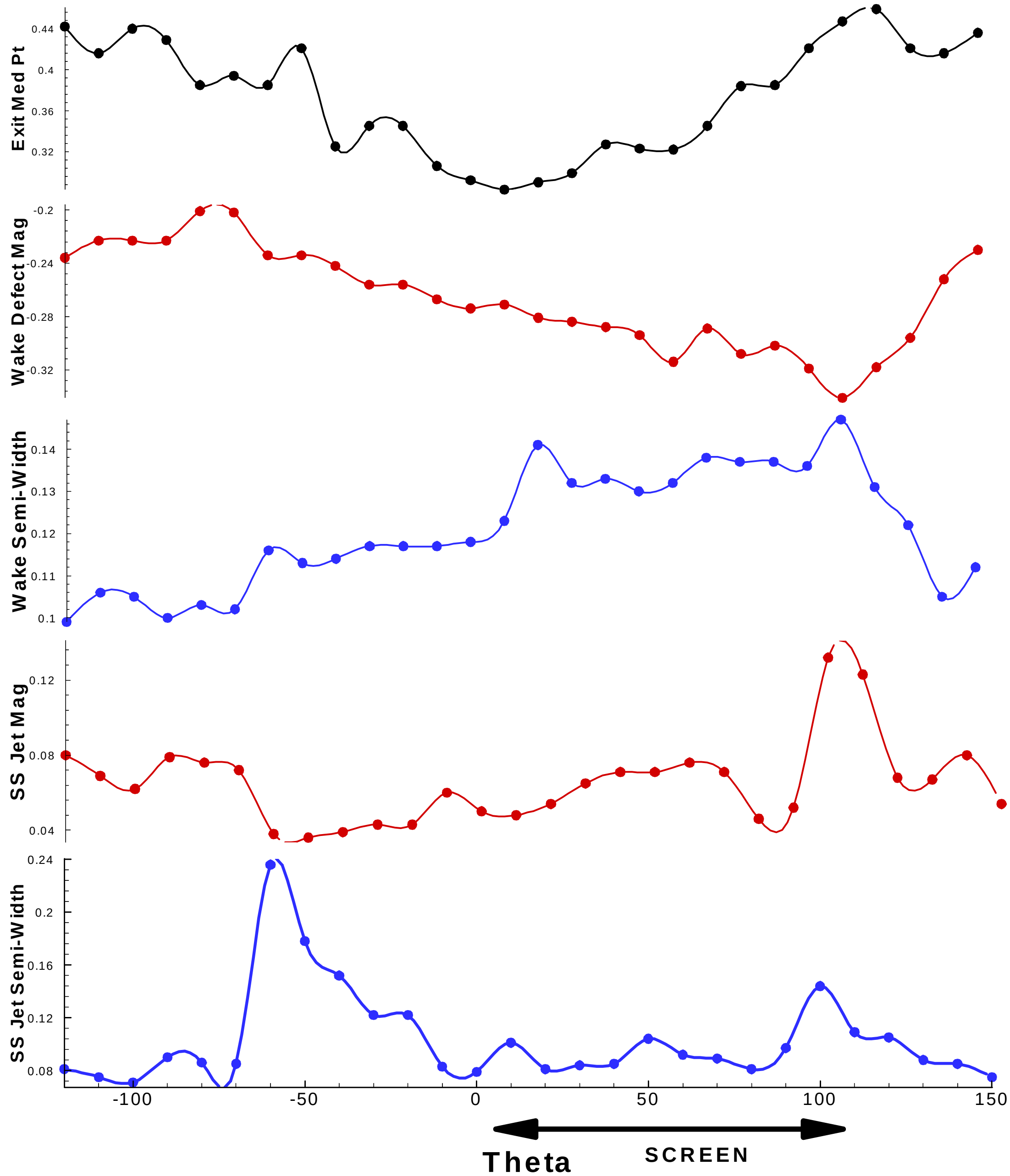

Figure A.34: Exit Flow Characteristics for Level 2, Operating Point C at 50% Span.

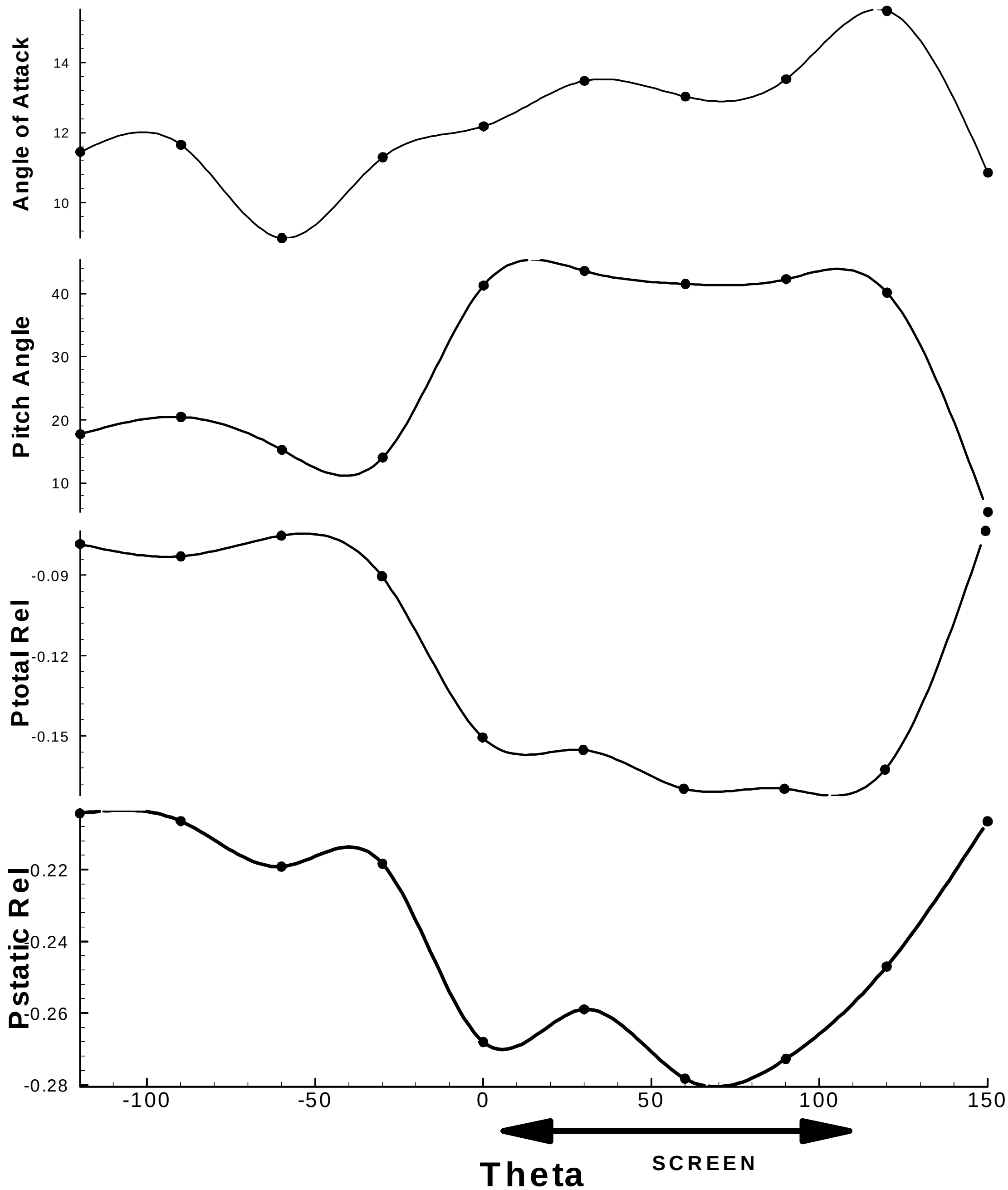

Figure A.35: Inlet Flow Characteristics for Level 2, Operating Point C at 33% Span.

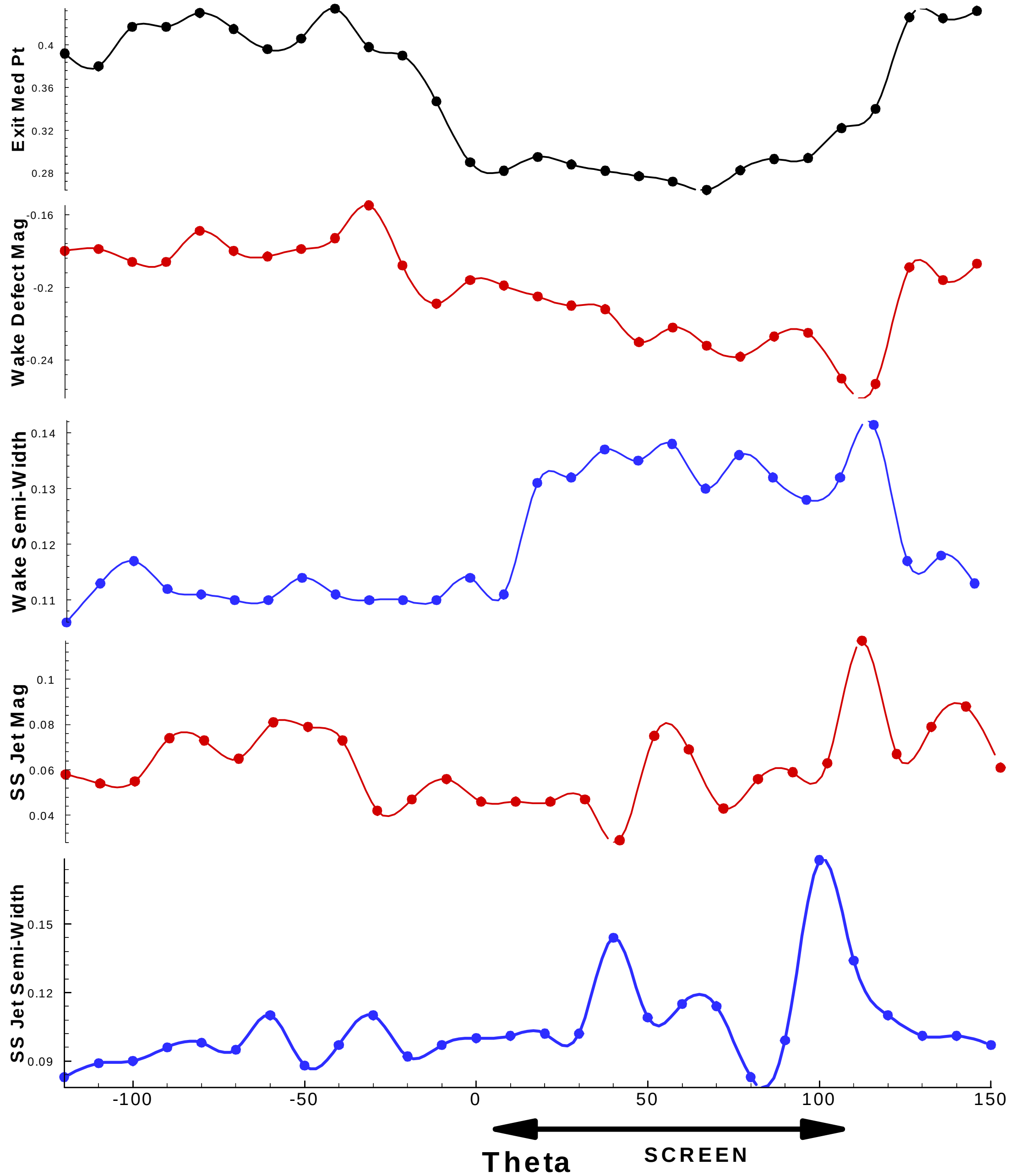

Figure A.36: Exit Flow Characteristics for Level 2, Operating Point C at 33% Span.

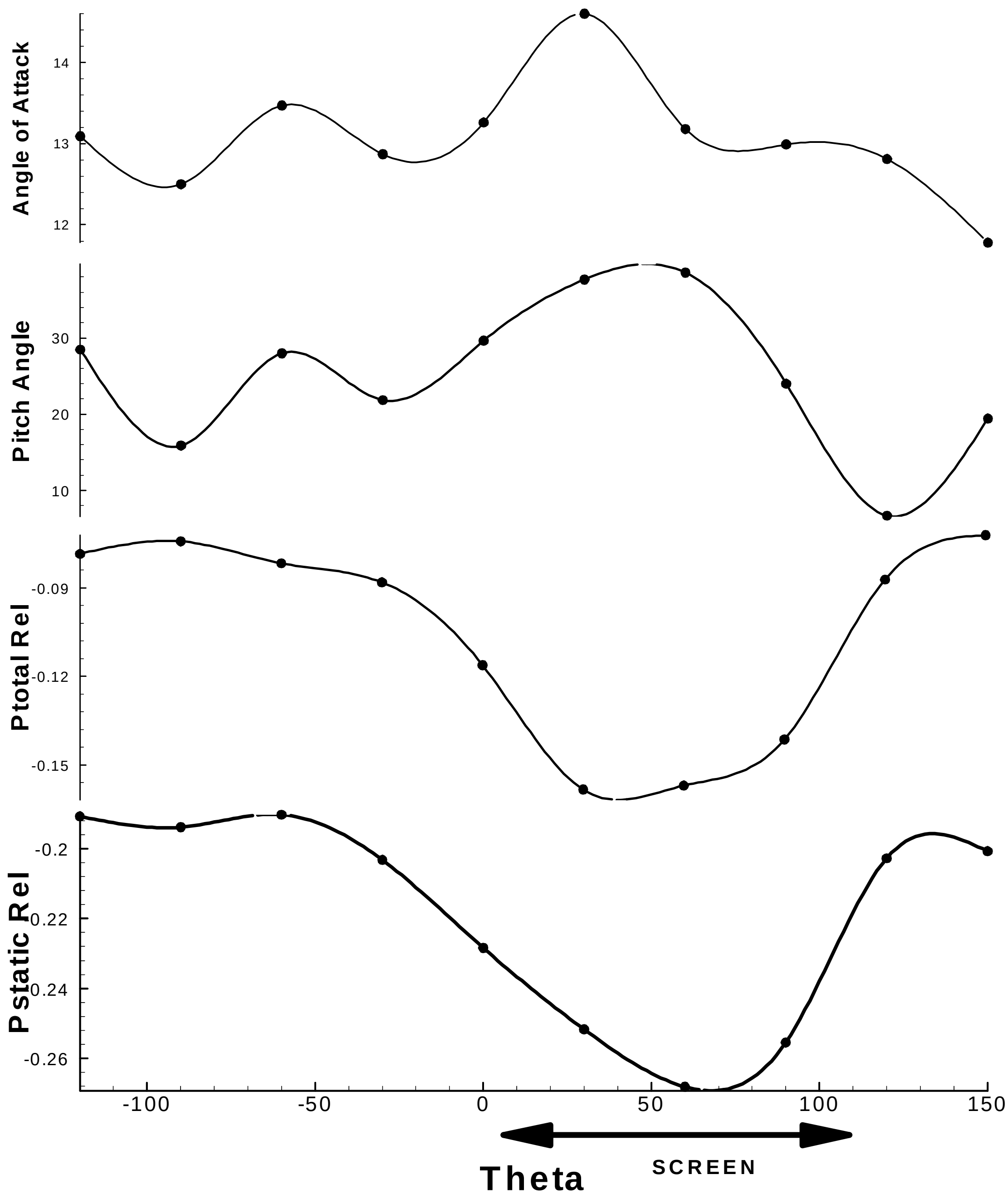

Figure A.37: Inlet Flow Characteristics for Level 2, Operating Point C at 67% Span.

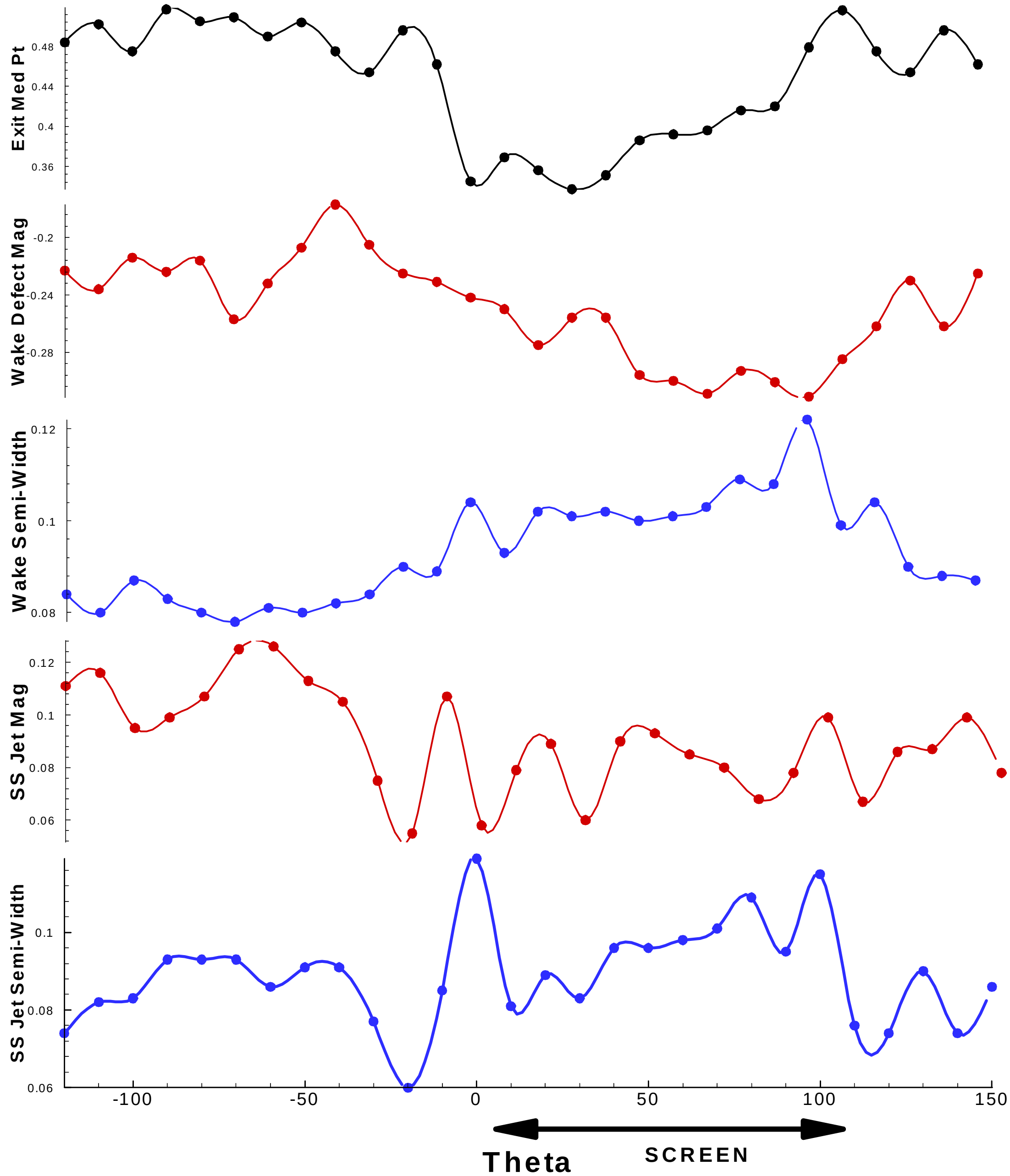

Figure A.38: Exit Flow Characteristics for Level 2, Operating Point C at 67% Span.

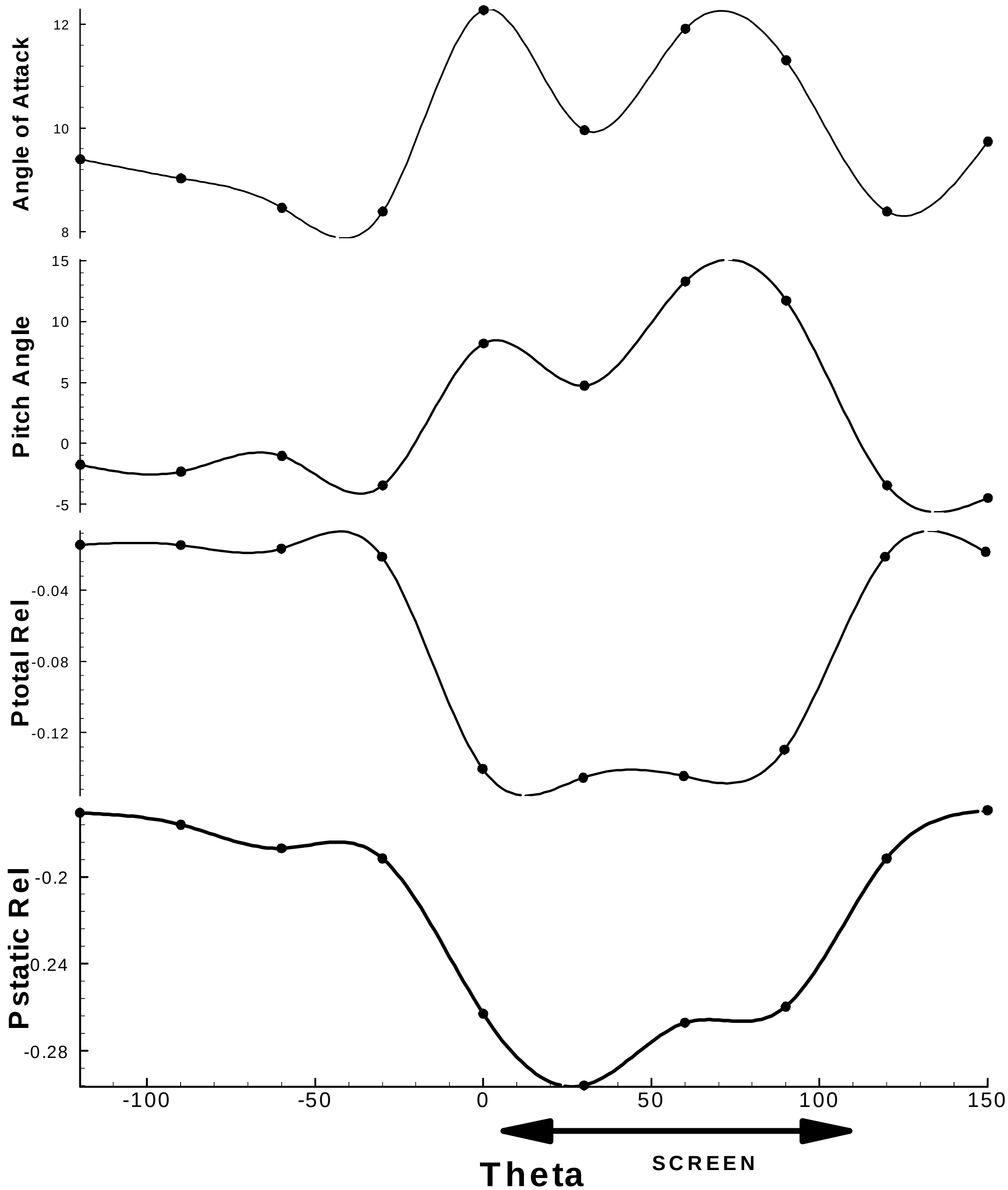

Figure A.39: Inlet Flow Characteristics for Level 3, Operating Point D at 50% Span.

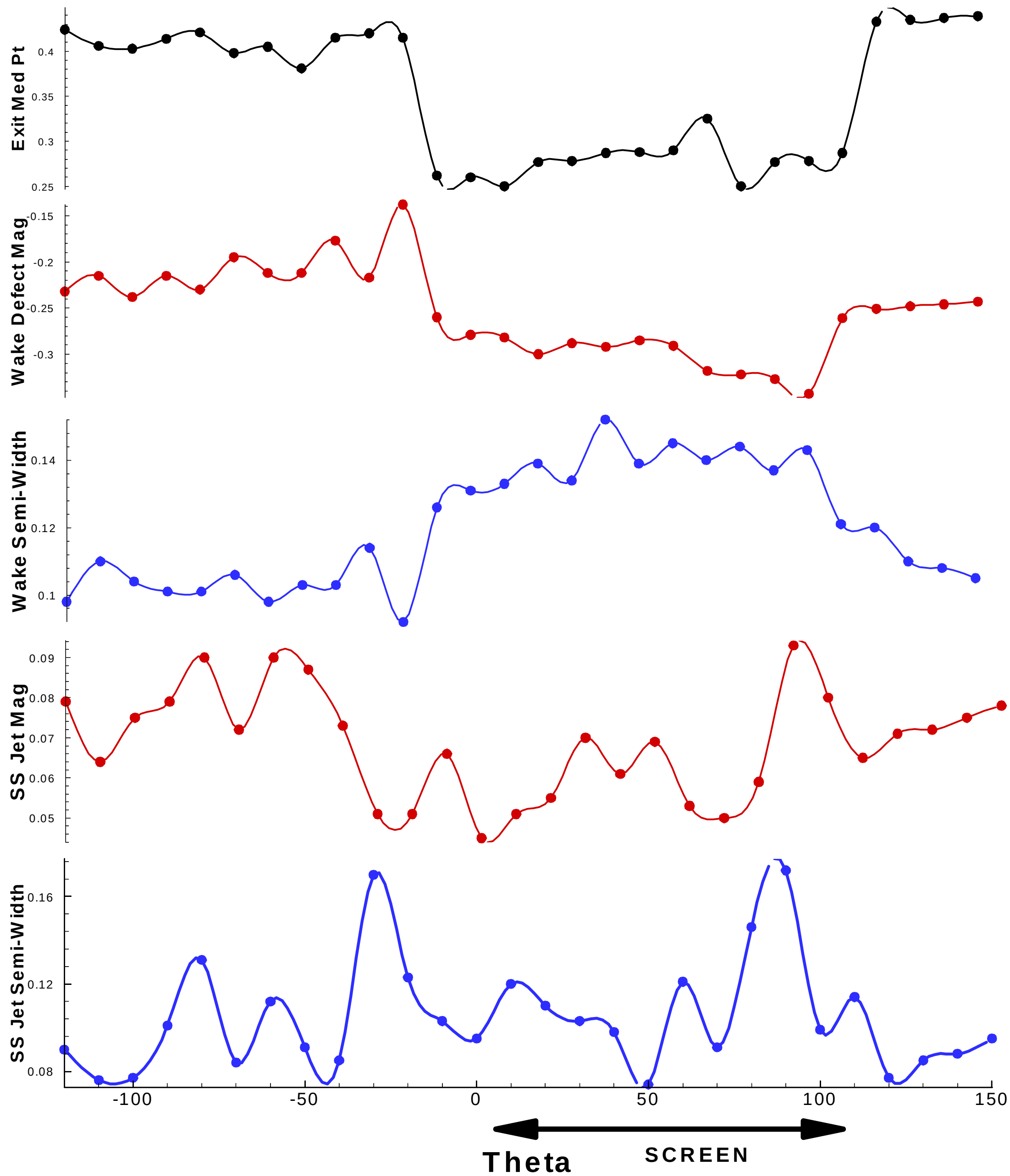

Figure A.40: Exit Flow Characteristics for Level 3, Operating Point D at 50% Span.

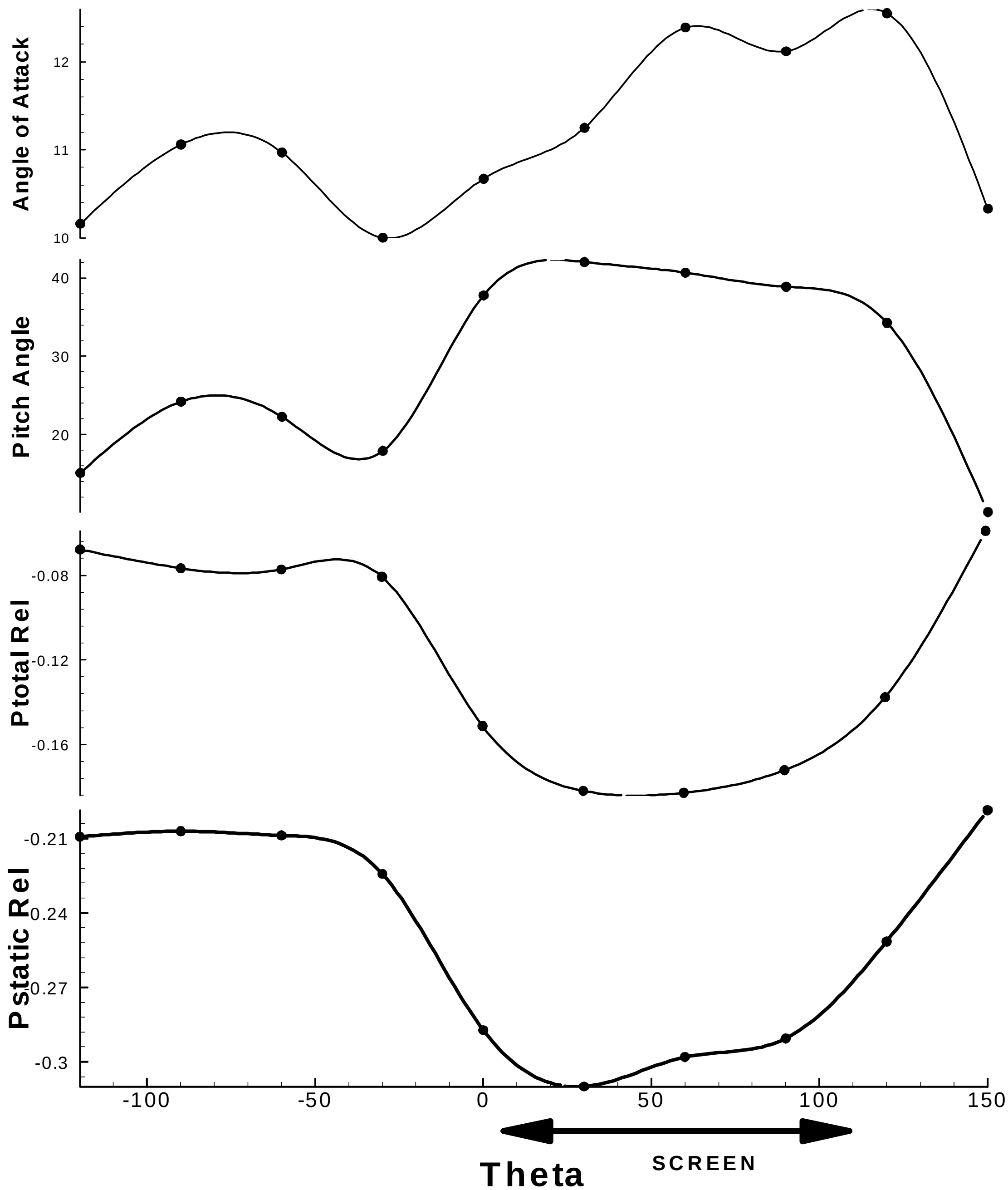

Figure A.41: Inlet Flow Characteristics for Level 3, Operating Point D at 33% Span.

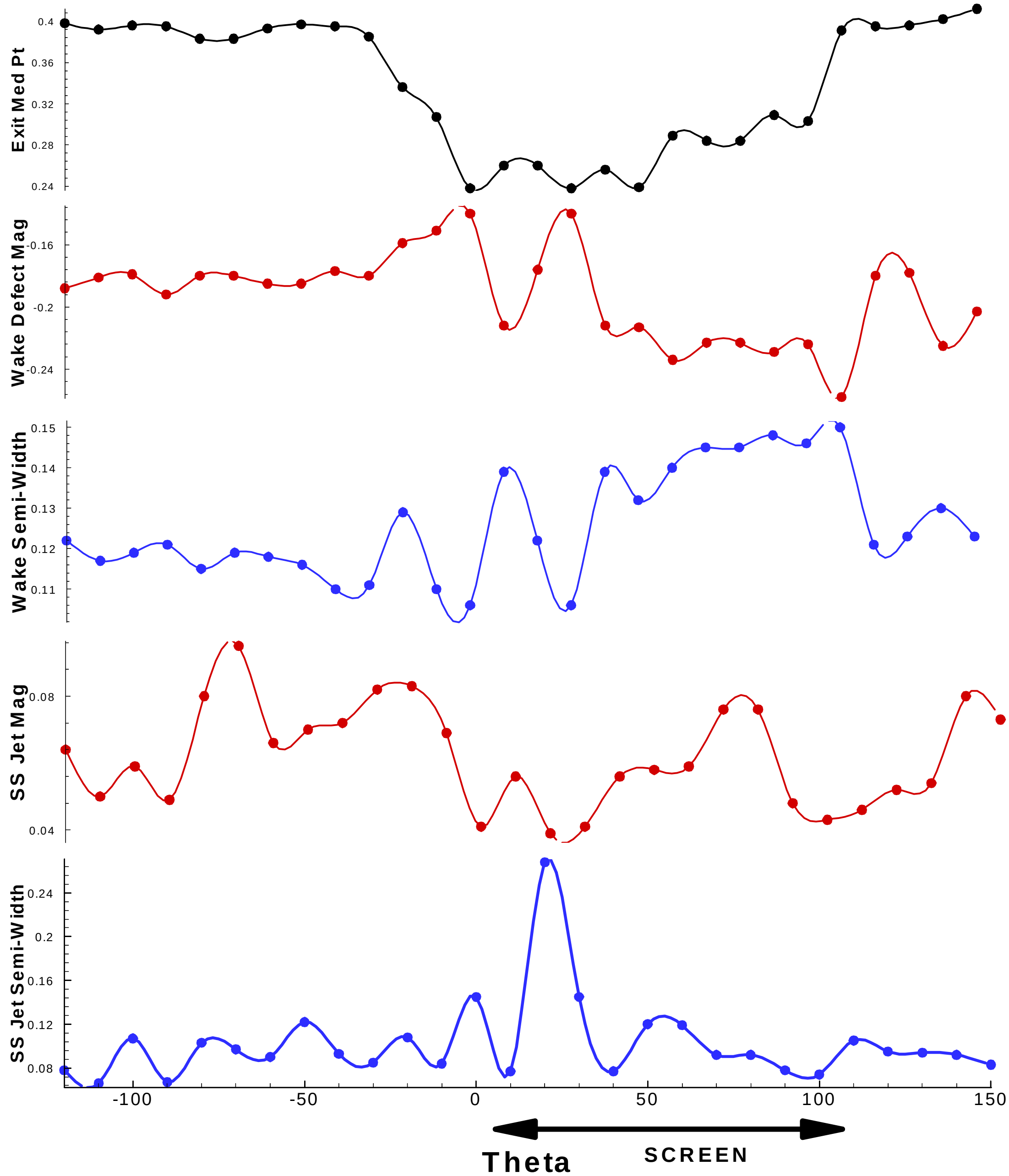

Figure A.42: Exit Flow Characteristics for Level 3, Operating Point D at 33% Span.

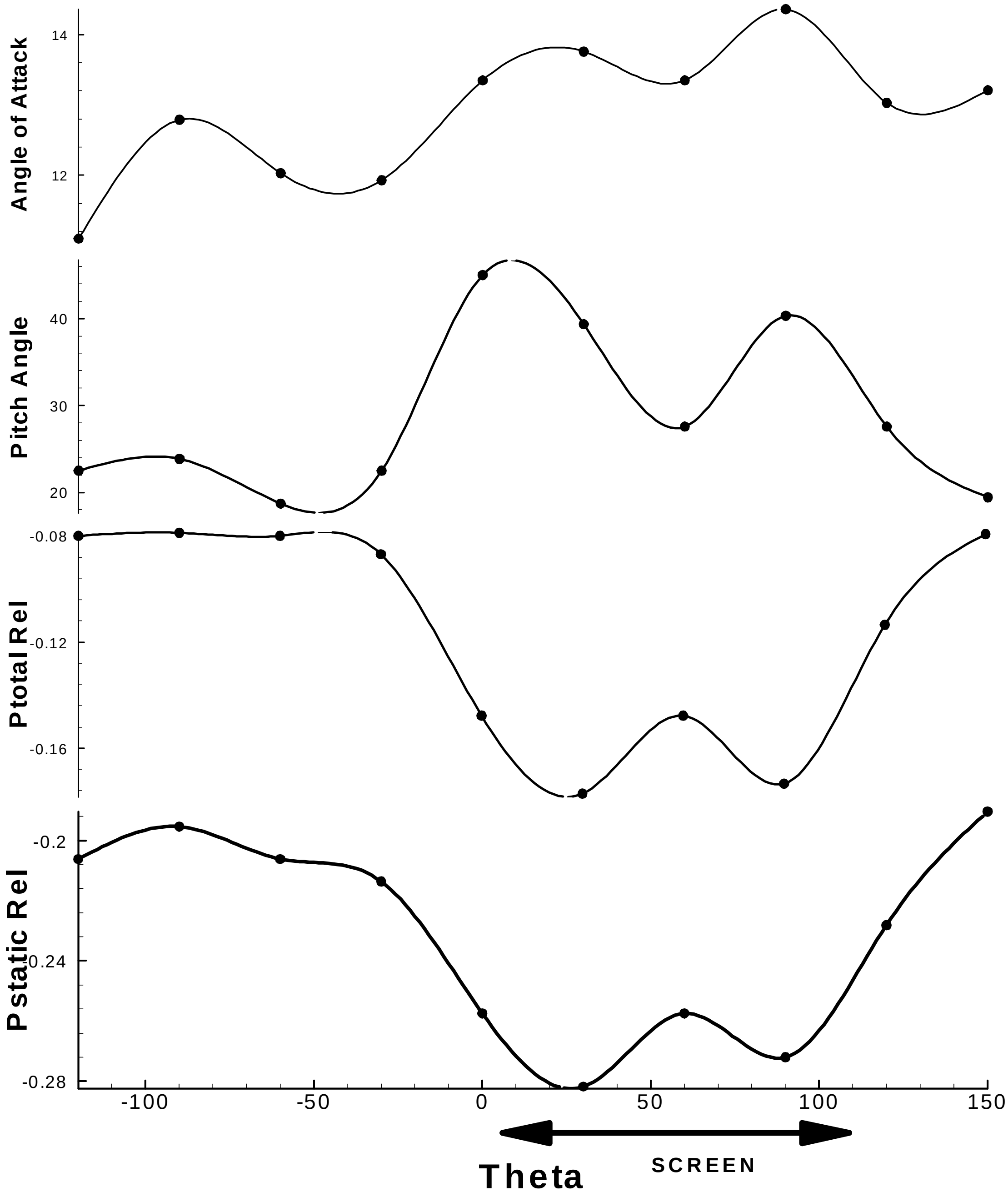

Figure A.43: Inlet Flow Characteristics for Level 3, Operating Point D at 67% Span.

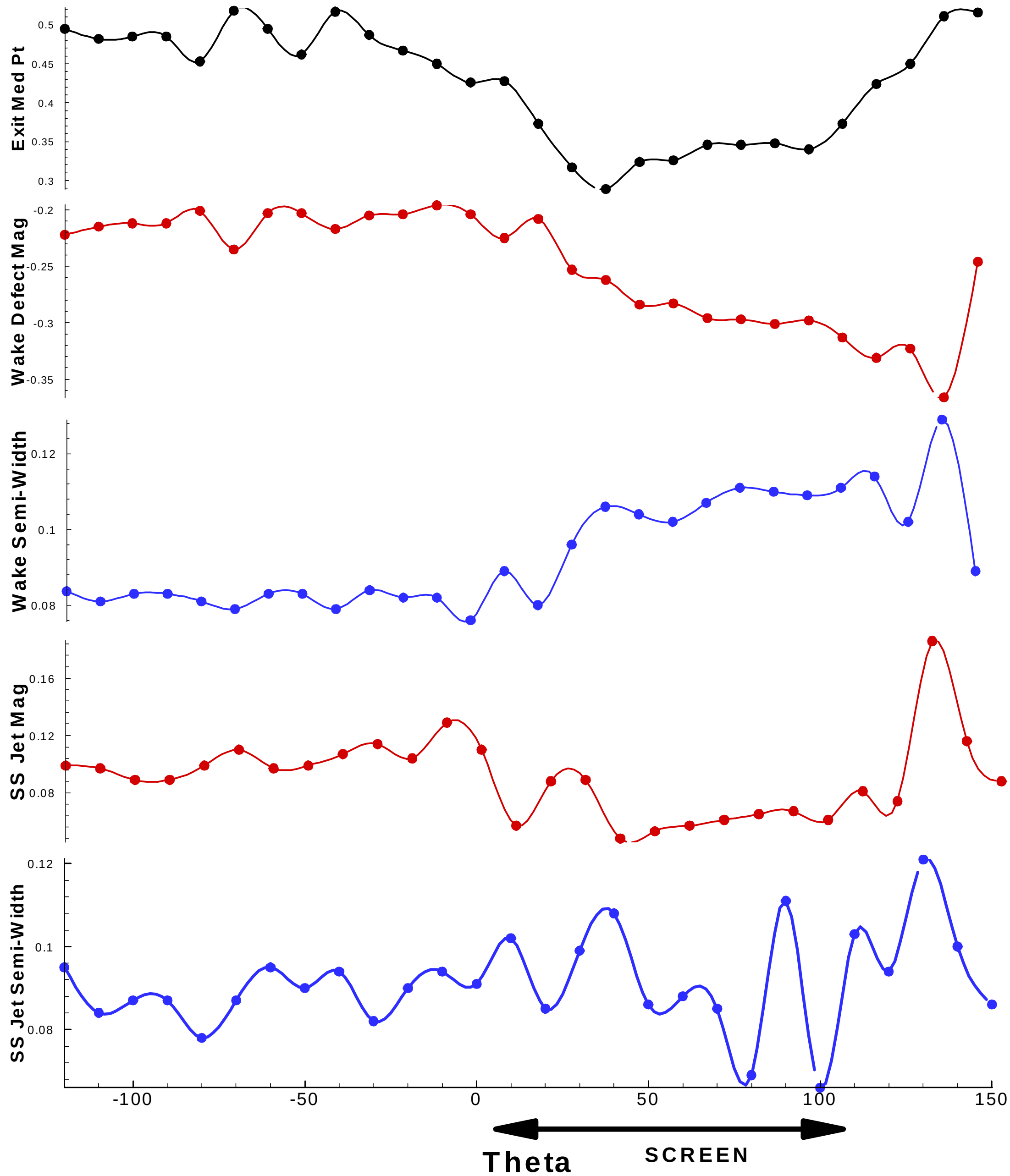

Figure A.44: Exit Flow Characteristics for Level 3, Operating Point D at 67% Span.

9. APPENDIX B

Measurement Uncertainty Analysis

This appendix presents an analysis of the measurement uncertainty for the inlet and exit flow measurements using the procedure of Kline and McClintock (39). This approach estimates experimental value uncertainty by summing the squares of the contributions of error from measured quantities and taking the square root of the sum to provide the final uncertainty of the experimental value.

9.1 Uncertainty in Five-Hole Probe Measurements

The uncertainty calculations for the five-hole probe are identical to those of Drost (37). The magnitude of the velocity is calculated according to the equation

$$V = \sqrt{\frac{2}{r}(p_1 - \bar{p})(1 + Cp_{static} - Cp_{total})} \qquad \textbf{(B.1)}$$

and the uncertainty of the velocity is given by

$$W_v = \sqrt{\left(\frac{\partial V}{\partial r} W_r\right)^2 + \left(\frac{\partial V}{\partial p_1} W_{p_1}\right)^2 + \left(\frac{\partial V}{\partial \bar{p}} W_{\bar{p}}\right)^2 + \left(\frac{\partial V}{\partial Cp_{static}} WC_{p\ static}\right)^2 + \left(\frac{\partial V}{\partial Cp_{total}} W_{Cp_{total}}\right)^2}$$

(B.2)

Drost approximated the partial derivatives by perturbing his data reduction program and observing the effects. Partial derivatives were found using the formula

$$\frac{\partial V}{\partial x} = \frac{V(x + \Delta x) - V(x)}{\Delta x} \qquad \textbf{(B.3)}$$

with V as a dependent variable and x an independent variable perturbed in the program. The maximal values were found by entering the following data with large angle variations

$$\frac{\partial V}{\partial \rho} = -10.4755 \frac{m/s}{kg/m^3}$$

$$\frac{\partial V}{\partial p_1} = +0.0696 \frac{m/s}{Pa}$$

$$\frac{\partial V}{\partial \bar{p}} = -0.0687 \frac{m/s}{Pa}$$

$$\frac{\partial V}{\partial Cp_{static}} = +11.0653 m/s$$

$$\frac{\partial V}{\partial Cp_{total}} = -11.0653 m/s$$

Solving Equation **(B.2)** required an estimation of the uncertainties in the measurements of the independent variables. Estimate of the uncertainty in the air density is as follows.

According to the ideal gas equation

$$\rho = \frac{p_a}{R \cdot T_a} \qquad \textbf{(B.4)}$$

therefore the uncertainty in the density is

$$W_p = \sqrt{\left(\frac{\partial \rho}{\partial p_a} W_{p_a}\right)^2 + \left(\frac{\partial \rho}{\partial T_a} W_{T_a}\right)^2} \qquad \textbf{(B.5)}$$

where the partial derivatives were found by differentiation of Equation **(B.4)** and substituting some typical values.

$$\frac{\partial \rho}{\partial p_a} = \frac{1}{R \cdot T_a} = +0.0000115 \frac{kg/m^3}{Pa}$$

$$\frac{\partial \rho}{\partial T_a} = -\frac{1}{R \cdot {T_a}^2} = -0.0036029 \frac{kg/m^3}{K}$$

$W_p \;= \pm 33.763 Pa$ (0.01 in. H_g)(readability of mercury barometer)

$W_{T\,a} = \pm 0.56 K (\pm 1^{o} F)$ (least readable thermometer)

Substituting the above values into Equation **(B.5)** results in

$$W\rho \;= 0.00205 \frac{kg}{m^3}$$

Assuming a normal distribution about the mean value, an estimate in the measured pressures was made. The uncertainty was expressed in the following manner

$$W = 2\sigma \qquad \textbf{(B.6)}$$

where

$$\sigma = \left(\frac{\sum_{i=1}^{N} (x_i - \bar{x})^2}{N - 1} \right)^2 \qquad \textbf{(B.7)}$$

and

x_i = measured value

$\bar{x}$ = mean of measured value

N = number of samples

Using a sample of 100 pressure values for identical flow conditions and evaluating Equation **(B.6)**, the uncertainty in pressure measurements was found to be

$$W_p = W_{p_1} = W_{\bar{p}} = 4.248 Pa$$

The static and total pressure coefficients are functions of both probe yaw angle β and pitch angle α.

$$Cp_{total} = f(\alpha,\beta)$$
$$Cp_{static} = f(\alpha,\beta) \quad \textbf{(B.8)}$$

The uncertainties for these coefficients are then

$$W_{Cp_{static}} = \sqrt{\left(\frac{\partial Cp_{static}}{\partial a} W_a\right)^2 + \left(\frac{\partial Cp_{static}}{\partial b} W_b\right)^2}$$

(B.9)

$$W_{Cp_{total}} = \sqrt{\left(\frac{\partial Cp_{total}}{\partial a} W_a\right)^2 + \left(\frac{\partial Cp_{total}}{\partial b} W_b\right)^2}$$

The partial derivatives in these equations are found by inspection of the calibration data and selection of the highest apparent values.

$$\frac{\partial Cp_{static}}{\partial a} = -0.03734 \frac{1}{\deg}$$

$$\frac{\partial Cp_{static}}{\partial b} = +0.064275 \frac{1}{\deg}$$

$$\frac{\partial Cp_{total}}{\partial a} = -0.03430 \frac{1}{\deg}$$

$$\frac{\partial Cp_{total}}{\partial \mathrm{b}} = -0.09337 \frac{1}{\mathrm{deg}}$$

The probe yaw and pitch angles are functions of the five pressures at the probe tip as expressed in terms of yaw and pitch pressure coefficients, the uncertainties of which are found by

$$\mathrm{W}_{\mathrm{a}} = \sqrt{\left(\frac{\partial \mathrm{a}}{\partial Cp_{yaw}} W_{Cp_{yaw}}\right)^2 + \left(\frac{\partial \mathrm{a}}{\partial Cp_{pitch}} W_{Cp_{pitch}}\right)^2}$$

$$\mathrm{W}_{\mathrm{b}} = \sqrt{\left(\frac{\partial \mathrm{b}}{\partial Cp_{yaw}} W_{Cp_{yaw}}\right)^2 + \left(\frac{\partial \mathrm{b}}{\partial Cp_{pitch}} W_{Cp_{pitch}}\right)^2} \qquad \textbf{(B.10)}$$

The partial derivatives are found in the same manner as mentioned above by inspection of the calibration data.

$$\frac{\partial \mathrm{a}}{\partial Cp_{yaw}} = 3.6078 \text{ degrees}$$

$$\frac{\partial \mathrm{a}}{\partial Cp_{pitch}} = 3.7837 \text{ degrees}$$

$$\frac{\partial \mathrm{b}}{\partial Cp_{yaw}} = 5.3639 \text{ degrees}$$

$$\frac{\partial \mathrm{b}}{\partial Cp_{pitch}} = 2.3090 \text{ degrees}$$

Finally, the yaw and pitch pressure coefficients depend on the measured five pressures at the probe tip, which are given by the following relations:

$$Cp_{yaw} = \frac{(P_2 - P_3)}{(P_1 - \bar{P})}$$

$$Cp_{pitch} = \frac{(P_4 - P_5)}{(P_1 - \bar{P})}$$

$$\bar{P} = \frac{(P_2 + P_3 + P_4 + P_5)}{4}$$

As the uncertainty in each of the five pressures was the same, it was the same for the average pressure $\bar{P}$ as well. Therefore, the uncertainty for the yaw and pitch pressure coefficients may be expressed as

$$W_{Cpyaw} = \sqrt{(\frac{\partial Cp_{yaw}}{\partial p_2} W_{\mathrm{r}})^2 + (\frac{\partial Cp_{yaw}}{\partial p_3} W_{p_1})^2 + (\frac{\partial Cp_{yaw}}{\partial p_1} W_p)^2 + (\frac{\partial Cp_{yaw}}{\partial \bar{p}} W_p)^2} \qquad \textbf{(B.12)}$$

$$W_{Cppitch} = \sqrt{(\frac{\partial Cp_{pitch}}{\partial p_4} W_{\mathrm{r}})^2 + (\frac{\partial Cp_{pitch}}{\partial p_5} W_{p_1})^2 + (\frac{\partial Cp_{pitch}}{\partial p_1} W_p)^2 + (\frac{\partial Cp_{pitch}}{\partial \bar{p}} W_p)^2}$$

Where

$Wp = Wp_1 = Wp_2 = Wp_3 = Wp_4 = Wp_5 = W\bar{p} = 4.248$ Pa

The partial derivatives from **(B.12)** were found by perturbing the cubic spline data evaluation program described in Appendix D using input data for a variety of flow angle combinations, with maximal values as follows:

$$\frac{\partial Cp_{yaw}}{\partial p_2} = +0.0047 \frac{1}{Pa}$$

$$\frac{\partial Cp_{yaw}}{\partial p_3} = -0.0091\frac{1}{Pa}$$

$$\frac{\partial Cp_{yaw}}{\partial p_1} = +0.0184\frac{1}{Pa}$$

$$\frac{\partial Cp_{yaw}}{\partial \bar{p}} = -0.0200\frac{1}{Pa}$$

$$\frac{\partial Cp_{pitch}}{\partial p_4} = +0.0041\frac{1}{Pa}$$

$$\frac{\partial Cp_{pitch}}{\partial p_5} = -0.0047\frac{1}{Pa}$$

$$\frac{\partial Cp_{pitch}}{\partial p_1} = +0.0014\frac{1}{Pa}$$

$$\frac{\partial Cp_{pich}}{\partial \bar{p}} = -0.0015\frac{1}{Pa}$$

Now based on **(B.12)** the yaw and pitch pressure coefficient uncertainties may be obtained:

$$W_{Cp_{yaw}} = 0.04498$$

$$W_{Cp_{pitch}} = 0.02762$$

Using **(B.10)** the uncertainties in yaw and pitch angle are obtained as

$$W_{\mathrm{b}} = 0.24999 \text{ degrees}$$

$$W_{\mathrm{a}} = 0.94737 \text{ degrees}$$

Therefore, uncertainties in the yaw and pitch angles round off to 0.25 degrees and 0.95 degrees, respectively. However, the accuracy of probe placement within the annulus was assumed to have a ± 3° uncertainty, and this number was deemed adequate for both yaw and pitch angles.

Now from **(B.9)**

$$W_{Cp_{static}} = 0.038841$$

$$W_{Cp_{static}} = 0.039985$$

Therefore, the uncertainty in velocity using **(B.2)** is

$$W_V = 0.74399\frac{m}{s}$$

or 0.7 meters per second.

9.2 Uncertainty in Performance Measurements

Flow density is calculated according to the ideal gas equation of state

$$\rho = \frac{p_a}{R \cdot T_a} \quad \textbf{(B.4)}$$

therefore the uncertainty in the density is as before

$$W_p = \sqrt{\left(\frac{\partial \rho}{\partial p_a} W_{p_a}\right)^2 + \left(\frac{\partial \rho}{\partial T_a} W_{T_a}\right)^2} \quad \textbf{(B.5)}$$

where the partial derivatives were found by differentiation of Equation **(B.4)** and substituting some typical values.

$$\frac{\partial \rho}{\partial p_a} = \frac{1}{R \cdot T_a} = +0.0000115 \frac{kg/m^3}{Pa}$$

$$\frac{\partial \rho}{\partial T_a} = -\frac{1}{R \cdot T_a^{\ 2}} = -0.0036029 \frac{kg/m^3}{K}$$

$W_p = \pm 33.763 Pa$ (0.01 in. H_g)(readability of mercury barometer)

$W_{T\,a} = \pm 0.56 K (\pm 1^\circ F)$ (least readable thermometer)

Substituting the above values into Equation **(B.5)** resulted in

$$W_\rho = 0.00205 \frac{kg}{m^3}$$

The flow at the inlet of the compressor was assumed to be incompressible and velocities from the Pitot rakes and Pitot-static probes were calculated from the reduced Bernoulli equation

$$V = \sqrt{2(P_t - P_s)/\rho} \quad \textbf{(3.1)}$$

where P_t is inlet total pressure, P_s is inlet static pressure, and ρ is flow density at the inlet. The uncertainty in velocity calculations is then

$$W_V = \sqrt{\left(\frac{\partial V}{\partial \rho} W_\rho\right)^2 + \left(\frac{\partial V}{\partial P_t} W_{P_t}\right)^2 + \left(\frac{\partial V}{\partial P_s} W_{P_s}\right)^2} \qquad \textbf{(B.13)}$$

and the partial derivatives are

$$\frac{\partial V}{\partial \rho} = -\left(\frac{P_t - P_s}{\rho^2}\right)\left(\frac{2}{\rho}(P_t - P_s)\right)^{-1/2}$$

$$\frac{\partial V}{\partial P_t} = \frac{1}{\rho}\left(\frac{2}{\rho}(P_t - P_s)\right)^{-1/2}$$

$$\frac{\partial V}{\partial P_s} = -\frac{1}{\rho}\left(\frac{2}{\rho}(P_t - P_s)\right)^{-1/2}$$

Typical values of total and static pressure at the inlet were

$$P_t = 2130.98 \frac{lb_f}{ft^2}$$

$$P_s = 2129.95 \frac{lb_f}{ft^2}$$

with a typical flow density at the inlet of

$$\rho = .0736 \frac{lb_m}{ft^3}$$

Evaluating the partial derivatives yields

$$\frac{\partial V}{\partial \rho} = -35.94 \frac{ft/\sec}{lb_m / ft^3}$$

$$\frac{\partial V}{\partial P_t} = 2.57 \frac{ft/\sec}{lb_f / ft^2}$$

$$\frac{\partial V}{\partial P_s} = -2.57 \frac{ft/\sec}{lb_f / ft^2}$$

With uncertainty for the density measurement known to be

$$W_\rho = 0.00205 \frac{kg}{m^3} = .0001279 \frac{lb_m}{ft^3}$$

and manufacturer uncertainty for static pressure is

$$W_{p_s} = \pm 0.07052 \text{ lb}_\text{f}/\text{ft}^2$$

The uncertainty in pressure as stated by the manufacturer is ± 0.15 % of the measured value. Recall that all pressures were measured relative to atmospheric. Using a typical total pressure value of – 0.1 inches of water based on the rake Pitot tube lowest within the boundary layer of the inlet, the uncertainty in total pressure at the inlet is

$$W_{P_t} = \pm 0.0007803 \frac{lb_f}{ft^2}$$

Substituting these values into Equation **(B.13)** yields

$$W_V = \pm 0.1813 \frac{ft}{\sec} = \pm 0.0553 \frac{m}{\sec}$$

Assuming this to be the error for the Pitot probe and each of the rake Pitot probes, we can use conservation of mass principles to find the error in the flow coefficient C_x/U_{tip}. Continuity yields

$$\mathrm{r}\, V_{inlet} A_{inlet} = \mathrm{r}\, V_{ann} A_{ann} \tag{B.14}$$

Where V_{inlet} and A_{inlet} and V_{ann} and A_{ann} are the flow velocities and areas at the inlet duct and annulus in the plane of the rotor, respectively. Knowing the low Mach number flow to be incompressible results in

$$V_{inlet} A_{inlet} = V_{ann} A_{ann} \tag{B.15}$$

with values of

$A_{inlet} = 0.1642\ m^2$
$A_{ann} = 0.085\ m^2$

Knowing V_{ann} to be equal to the average axial velocity C_x through the blade passage yields the error in the axial flow to be

$$W_{C_x} = \pm 0.3502 \frac{ft}{\sec} = \pm 0.1068 \frac{m}{\sec}$$

With rotor rotational speed held constant at 2100 rpm and a blade tip radius of 0.7492 ft (0.228346 m), the uncertainty in the non-dimensional flow coefficient is

$$W_{C_x / U_{tip}} = 0.002127$$

Rotor performance was obtained using the non-dimensional total pressure rise

$$\Psi = \frac{P_{ann} - P_{atm}}{\frac{\mathrm{r} \cdot U_{tip}{}^{2}}{2}} \tag{3.5}$$

In this case, P_{ann} refers to the total pressure downstream of the rotor as measured by a Pitot-static probe. As all pressures were measured relative to atmospheric, uncertainty in atmospheric pressure P_{atm} is ignored. Based on Equation **(3.5)** the uncertainty in ψ is

$$W_{\Psi} = \sqrt{\left(\frac{\partial \Psi}{\partial P_{ann}} W_{P_{ann}}\right)^{2} + \left(\frac{\partial \Psi}{\partial \mathrm{r}} W_{\mathrm{r}}\right)^{2}} \tag{B.16}$$

The partial derivatives were found by differentiation of Equation **(3.5)** and substituting some typical values.

$$\frac{\partial \Psi}{\partial P_{ann}} = \frac{1}{\frac{1}{2}\mathrm{r}\, U_{tip}{}^{2}} = 0.0006474 \frac{m^{2}}{N}$$

$$\frac{\partial \Psi}{\partial \mathrm{r}} = -\frac{\left(P_{ann} - P_{atm}\right)}{\frac{1}{2}\mathrm{r}^{2} U_{tip}{}^{2}} = 0.2378 \frac{m^{3}}{kg}$$

From before,

$$W_{\mathrm{r}} = 0.00205 \frac{kg}{m^{3}} = .0001279 \frac{lb_{m}}{ft^{3}}$$

and assuming the manufacturer's specifications for $\pm 0.0015\,\%$ uncertainty in total pressure measurements gives

$$W_{P_t} = \pm 0.675 \frac{N}{m^2}$$

Substituting these values into Equation **(B.16)** gives the error in the non-dimensional pressure rise coefficient to be

$$W_{\Psi} = \pm 0.0006547$$

9.3 Uncertainty in Steady/Unsteady Rotor Exit Flow Measurements

Rotor exit one-dimensional total pressure measurements were obtained using the piggyback steady/unsteady probe described in Ch. 3. Pressure signals from each of the separate steady and unsteady probes were superimposed to provide dynamic measurements in the wake of the rotor.

The uncertainty for the steady component of the piggyback probe is assumed equal to the unsteadiness of the downstream total pressure probe

$$W_{P_t\,steady} = \pm 0.675 \frac{N}{m^2}$$

According to the manufacturer, the uncertainty due to combined non-linearity and hysteresis in the high-response transducer was ± 0.75 %. With a typical total pressure value of 0.632 N/m^2 relative to atmospheric, the uncertainty in the unsteady total pressure measurement is

$$W_{P_t\,unsteady} = \pm 0.00474 \frac{N}{m^2}$$

Superposing the uncertainties of the steady and unsteady one-dimensional total pressure measurements gives the uncertainty for the total pressure of the combination probe as

$$W_{P_t} = \pm 0.67974 \frac{N}{m^2}$$

10. APPENDIX C

Instrumentation/Hardware

10.1 Computer/Data Acquisition System

<u>Computer</u>

Gateway P166 laptop

64 MB RAM

4.0 GB hard drive

<u>I/O card</u>

National Instruments DAQCard-AI-16E-4

8 differential channels

12 bit, 1 in 4096 resolution

250 kS/sec maximum sampling rate

1024 sample FIFO buffer size

512 word configuration memory size

800 kHz small signal (-3 dB) bandwidth

400 kHz large signal (1% THD) bandwidth

<u>Board</u>

National Instruments SCB-68

Screw terminals for I/O connections

Shielded enclosure

10.2 Compressor Control

Rheostat: General Electric 5748472G130

Drive Motor: General Electric KINEMATIC Direct Current Generator 5CD256G38

Compressor: General Electric Fan Unit 7A5-A1

10.3 Pressure Transducers

Datametrics Type 590 Integral Barocel Pressure Transducer

General Specifications:

Pressure Range: 10 inches of H_2O

Power Requirements: 18 to 35 Volts DC or 20 to 33 Volts AC at 75 mA. 50-60 Hz

Output Signal: 0 to ±10 Volts DC, 2 mA into 5 K Ω load, floating (Code-4), zero adjustable ± 0.5 %, span adjustable ± 1.0 %.

Leak Rate to Ambient: Viton-sealed model (Code-V) 5E-7 std cc/sec @ 760 Torr
All-welded model (Code-H) 1E-10 std cc/sec @ 760 Torr

Electrical Fittings: MS3102A-16S-1PZ (One mating connector, MS3106A-16S-1 SZ is supplied with each 590 transducer)

Pressure Fittings: 1/8” – 27 NPT (Code-1) standard

Volume: 5.0 cc per side, with zero differential pressure applied, 0.16 cc diaphram displacement with full range pressure applied

Transient Response: 8 msec (to step input of zero to sensor full pressure range pressure, at 1 atm line pressure, with no external tubulation, measured to 63 % f.s.)

Diaphram Resonant Frequency: 3 kHz (nominal)

Overpressure: 1.5 times sensor full range

Ambient Temperature Range: Storage: -45 °C to + 85 °C
Operating: +5 °C to + 70 °C
Calibration: +10 °C to + 50 °C

Temperature Effects: 30 ppm/°C on zero, 300 ppm/°C on slope

Accuracy (zero-based linearity): ± 0.15 % of reading + 0.01 % f.s.

Repeatability: 0.01 % of reading + 0.005 % of maximum applied pressure

Hysteresis Error: ± 0.001 %

Datametrics Type 1400 Electric Manometer

General Specifications:

Display: 3 ½ digits, update twice per second

Power Requirements: 115 Volts AC, 50-60 Hz, 0.2 A

Outputs: 28 Volts DC, capable of powering up to 6 Barocels and one Type 1402 Barocel Selector, 0 to ± 1 Volts DC pressure signal, BCD DTL/T2L compatable

Controls: Power ON/OFF, Zero and Span adjustment, Range switch with X1 and X0.1 scales, and calibrate position

Ambient Temperature: Operating + 10 °C to + 40 °C, storage –45 °C to + 55 °C

Interconnecting Cables: Type 711-15, 15 feet in length

Entran EP Pressure Transducer

Model EPE-541-2P-/R

Sensitivity: 77.5 mV/Psig

Input Impedance: 1062 Ω

Output Impedance: 1041 Ω

Range: 2 psig

Burst Pressure: 46 psig

10.0 Volts excitation, gauge reference

Resonant Frequency: 80 kHz nominal, within ± ½ dB to 5 kHz, ± 5 dB to > 20 kHz

Nonlinearity and Hysteresis: 2P & .13 B: ± 1 ½ %, 5P & .35 B: ± 3/4 %; M: ± ½ dB Amp. Lin.

<u>Entran IMV Amplifier</u>

Model IMV-15/10/100A-WW

Voltage Supply: ± 15 Volts DC

Sensor Excitation: 10 Volts DC

Gain: 100 adjustable ± 10 % min.

Base line: Externally adjustable ± 500 mVolts

Full Range Out (12 Volts max.): 12 Volts with 50 Ω load

Operating Temperature: - 29 °C to + 82 °C

Storage Temperature: -40 °C to 120 °C

- 3 dB Bandwidth (nominal): at 50 gain, 80 kHz typ.; at 100 gain, 70 kHz typ.

Nonlinearity & Hysteresis: ± 0.05 %

Output Current (max.): 50 mA with up to 50 Ω load, 25 mA with 500 Ω load

11. APPENDIX D

Cubic Spline Interpolation

As cubic spline interpolation was used to obtain the steady five-hold probe inlet data as well as the lines interpolating many plots in this document, a brief introduction to cubic spline techniques is in order. The cubic spline procedure described is that set forth by Drost (37) and Burden and Faires (40). Figure A.32 depicts an arbitrary function fitted with a cubic spline. The interpolation involves four constants which empower the interpolant to not only be continuously differentiable on the interval but to have a continuous second derivative on the interval as well. The functions are valid between two specific points and their values and slopes correspond to those of the adjacent functions at the connecting points.

The third order approach creates a set of functions

$$S_j(x) = a_j + b_j(x-x_j) + c_j(x-x_j)^2 + d_j(x-x_j)^3 \qquad \textbf{(A.1)}$$

for the number of points $j = 0, 1, \ldots, n-1$. Each function $S_j(x)$ is valid for the range x_{j-1} to x_j. Since values $S_{j+1}(x_{j+1}) = S_j(x_{j+1})$ and slopes $S'_{j+1}(x_{j+1}) = S'_j(x_{j+1})$ for each $j = 0, 1, \ldots, n-2$ it is possible to derive a linear system of equations

$$(x_j - x_{j-1})(c_{j-1}) + 2(x_{j+1} - x_{j-1}) + (x_{j+1} - x_j)(c_{j+1}) = (3/(x_{j+1} - x_j))(a_{j+1} - a_j) - (3/(x_j - x_{j-1}))(a_j - a_{j-1}) \qquad \textbf{(A.2)}$$

for each $j = 1, 2, \ldots, n-1$. The Drost program **spline.bas** performs a Gauss-Seidel iteration on this linear system to numerically solve for the unknown constants.

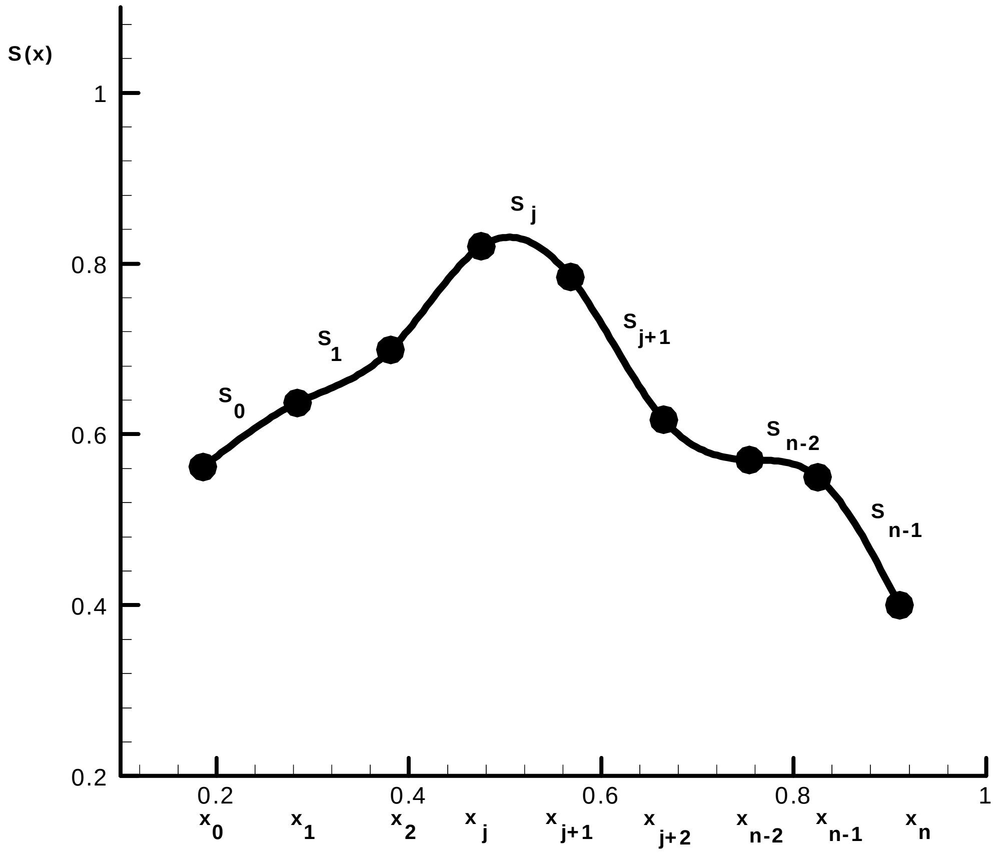

Figure D.1: Graphic of Cubic Spline Interpolation Technique.

12. VITA

The author was born on December 14, 1972 in Tucson, Arizona. He attended Green Fields Country Day School in Tucson for eight years, finishing high school in 1990. He then enrolled in the Mechanical Engineering program at Northern Arizona University and graduated Cum Laude with his Bachelor of Science degree in 1996. Over the course of his undergraduate career, he worked with Oak Ridge National Laboratory and Arizona Public Service Company. He is a member of Tau Beta Pi, Pi Tau Sigma, Phi Kappa Phi, the American Society of Mechanical Engineers, and the American Institute for Aeronautics and Astronautics. He is a registered Engineer-in-Training in the State of Arizona. He accepted Jesus Christ as his personal Savior and Lord on April 8, 1995. After graduation he will begin working as a Mechanical Designer with Siemens Westinghouse Electric Power Generation in Orlando, Florida, where he looks forward to spending a great deal of time on the beach.

Shaun M. Boller